

https://dspace.org/

Electric monopole (E0) transitions studies in medium mass 50 A 72 nuclei

Avaa, Abraham Aungwa

2020
https://hdl.handle.net/10539/31415

Downloaded from a DSpace repository. https://dspace.org/

Electric Monopole ($E0$) Transitions Studies in Medium Mass $50 \leq A \leq 72$ Nuclei

Abraham Aungwa Avaa



A thesis submitted to the Faculty of Science,
University of the Witwatersrand, in fulfilment of
the requirements for the degree of
Doctor of Philosophy.

Johannesburg 2020

University of the Witwatersrand

School of Physics

Electric Monopole ($E0$) Transitions Studies in Medium Mass $50 \leq A \leq 72$ Nuclei

Abraham Aungwa Avaa

Ph.D. thesis

Supervisors:

Prof. I. T. Usman

School of Physics
University of the Witwatersrand, Johannesburg

Dr. P. M. Jones

iThemba Laboratory for Accelerator Based Sciences
Cape Town

Declaration

I declare that the thesis being submitted for the Degree of Doctor of Philosopy to the University of the Witwatersrand, Johannesburg is my own research work. It has not been submitted previously for any degree to any other university.



Abraham Aungwa Avaa

26 June 2020

Date

Abstract

The study of electric monopole ($E0$) transitions between two excited 0^+ states is important because the monopole strength carries vital information about the nuclear structure due to its direct link with the mean-square charge radius $\langle r^2 \rangle$ and quadrupole deformation parameter β_2. Therefore, the measurement of internal conversion electrons (ICE) or internal pair formation (IPF) is crucial for $E0$ transition studies. Transitions between 0^+ states do not bear a change in angular momentum. Hence, single-photon emission is forbidden, but 0^+ states can decay via conversion electrons or pair formation and two-photon emission which is mostly negligible. To implement $E0$ studies at iThemba Laboratory for Accelerator Based Sciences (iThemba LABS), an electron spectrometer that uses a solenoidal magnetic field acting as a lens and a Si(Li) detector has been refurbished and characterized using calibration sources of ICE. Figures of merit have been extracted and compared with simulations. The spectrometer coupled with an array of $LaBr_3$:Ce detectors and Low Energy Photon Spectrometers (LEPS) was successfully implemented for in-beam experiments. Internal conversion coefficients (ICC) deduced from in-beam measurements of ^{72}As and ^{72}Ge were used to complement previous assigned multipolarities. The monopole strength $\rho^2(E0) \times 10^3$, $\langle r^2 \rangle$ and β_2 values, extracted from the observed $E0$ transition in ^{72}Se are 33(9), 2.2(6) fm^2 and 0.21(5) respectively. The goal of the experiment was to probe the under-

lying nuclear structure in $50 \leq A \leq 72$ region. The magnitude of the monopole strength suggests the presence of shape coexistence in ^{72}Se, in agreement with previous reports.

Another set of measurements were carried out at the Australian National University (ANU) using the Super-e spectrometer. A proton beam was delivered by the 14UD tandem accelerator on a ^{54}Cr target. The goal of the experiment was to populate the low-lying states in ^{54}Cr via (p, p') reaction with the aim of deducing the $E0$ strength values for the $0_2^+ \rightarrow 0_1^+$ and $2_2^+ \rightarrow 2_1^+$ transitions and afterwards search for the presence of shape coexistence. Shape coexistence has never been observed in the Ti and Cr isotopes. Though, the (p, n) reaction channel formed ^{54}Mn, the results of which yielded important physics information on the structure of the low-lying states. The first ICE and IPF spectra obtained for ^{54}Mn are presented. The multipolarities of nine new transitions have been unambiguously assigned based on the measured ICCs. The study also present the first observed $E0$ transition between $2_2^+ \rightarrow 2_1^+$ in ^{54}Mn isotope. A $\rho^2(E0\text{: } 2_2^+ \rightarrow 2_1^+) \times 10^3$ value of 626^{+142}_{-115} was deduced using literature transition rates and mixing ratios; and ICC values derived in this work.

Acknowledgements

This research work is possible today because of the strong backing of my supervisor, Dr. Pete Jones. He played pivotal roles towards this PhD project from securing of funds for my upkeep and travels. He has also given me international exposure and links to World experts in my field of study. I would like to say he has given me the requisite foundation I need to grow as an experimental nuclear Physicist.

Secondly, my sincere appreciation goes to my University supervisor Prof. Usman Iyabo who played a special role in this PhD, beginning from the admission process, link to iThemba LABS where I got a research project. She was supportive morally and financially when I was not able to raise my full school fees. Her supervision has added great value to the content and quality of this thesis. I appreciate you Ma.

I would like to thank my research group members, Maluba Chisapi for his support with Geant4 simulations which facilitates the characterization of the electron spectrometer. Other members include L. Msebi, D. Kanfac-Jiotsa, M. Bashir and B. R. Zikhali. Their critique during our group meetings were valuable as they help me to see things in a deeper perspective.

Next to be appreciated immensely is G. De Villiers for simulating the magnetic field and the Instrumentation and IT (INIT) Department for fabrications, design

and production work done while refurbishing the spectrometer. Many thanks to J. Broodryk for his drawings and the accelerator group for providing a beam for the commissioning of the spectrometer.

The crucial role of my colleagues H.M. Sinegugu, C.P. Britz, S.S Mhlongo, T. Khumalo, A.S. Makuhane, and L. Mdletshe in data collection during the in-beam experiment is highly appreciated. Another group of people worth Acknowledging is my office colleagues who provided help with analysis software like ROOT, Radware and Xmgrace whenever I am stuck.

The second set of data for this thesis was taken from experiment performed at ANU with the help of A. Prof. Tibor Kibedi. Thus, I would like to sincerely express my gratitude to Tibor who purchase the target material for my experiment and secured a beam time for me. He was also supportive throughout the analysis period. On this note, I would like to thank all the ANU collaborators particularly those who took shifts during the experiment.

Also worthy of mentioning is my neighbour, Dr. A. Simo for her support, Mr. Lucas Mjola and his wife Moloko for their prayers and moral support. I am grateful to Joel Kostensalo for his assistance with the Shell model calculations and Dr. Nikolay for the 5DCH theoretical calculations.

Finally, on a special note, I would like to thank my amiable wife, Martha who endure a lot of lonely nights through this period yet remain supportive. My daughter Precious-Iyua and my son Perfect Teryimam who has been praying for this study to be completed. My parents James Avaa and Mother Hannah are also not left out in this acknowledgement, thank God for keeping you alive to witness the foundation you laid many years ago come to fruition. I thank you for all your sacrifice the Lord bless you all.

This work was supported by the National Research Foundation (NRF), South Africa under grant numbers [93533, 118645 and 99037]. Support from iThemba Laboratory for Accelerator Based Sciences, South Africa is greatly appreciated.

Dedications

This thesis is dedicated to the Almighty God who kept me during this period.

Contents

Declaration ii

Abstract iii

Acknowledgements v

Dedication viii

List of Figures xxii

List of Tables xxiv

1 Introduction 1

1.1 $E0$ transitions in the mass 70 region 2

1.2 $E0$ transitions in the mass 50 region 4

1.3 Present work 5

1.4 Structure of the thesis 6

2 Theoretical Review 7

2.1 Atomic theory 7

2.1.1 Atomic shells 8

2.2 Nuclear models 9

2.2.1 The concept of the shell model . . . 10
2.2.2 Nuclear spin-orbit coupling . . . 12
2.2.3 The interacting shell model . . . 13
2.2.4 NuShellx Formalism . . . 14
2.2.5 Collective Bohr Hamiltonian . . . 16
2.2.5.1 Covariant density functional theory (CDFT) . . . 20
2.3 Electromagnetic transitions . . . 21
2.3.1 Gamma-ray transitions . . . 21
2.3.1.1 Electric and magnetic moments . . . 22
2.3.2 Internal conversion . . . 23
2.3.2.1 Internal conversion coefficient (ICC) . . . 24
2.3.3 Internal pair formation (IPF) . . . 25
2.3.4 Parity and selection rules . . . 26
2.3.5 Reduced transition probability . . . 27
2.4 Electric monopole (*E0*) transitions . . . 29
2.4.1 Model prediction of $E0$ transitions . . . 33
2.4.2 Shape coexistence . . . 34
2.4.2.1 Link between $E0$ transitions and shape coexistence 35
2.5 Nuclear reactions . . . 36
2.5.1 Compound reaction . . . 37
2.5.2 Direct reaction . . . 38
2.5.3 Coulomb barrier and Coulomb excitation . . . 38
2.5.4 Reaction kinematics . . . 39
2.5.5 Nuclear reaction cross section . . . 41

3 Electron Spectrometer 43

3.1 Review of electron spectrometers . . . 43
3.1.1 Lens spectrometer . . . 44
3.1.2 Solenoid spectrometer . . . 45
3.1.3 Mini-orange . . . 46
3.2 Description of the refurbished spectrometer at iThemba LABS . . . 48
3.3 Magnetic field profile . . . 49
3.4 Spectrometer modification . . . 52
3.4.1 Vacuum system . . . 52
3.4.2 Target and detector support system . . . 52
3.4.3 Cryogenic system . . . 54
3.4.4 Magnet control system . . . 55
3.5 Electron spectrometer calibration . . . 57
3.5.1 Momentum window . . . 57
3.5.2 Geant4 simulation of spectrometer properties . . . 62
3.5.3 Spectrometer efficiency calibration . . . 64

4 Experimental Techniques **68**

4.1 Experiment at iThemba LABS . . . 68
4.1.1 ^{70}Ge target preparation . . . 69
4.1.2 Alpha beam . . . 69
4.1.2.1 Calculation of angular beam spreading . . . 70
4.1.2.2 Kinematic of ^{70}Ge(α,X)Y reactions . . . 72
4.2 Electron and gamma-ray detection . . . 74
4.2.1 Photoelectric absorption . . . 75
4.2.2 Compton scattering . . . 76
4.2.3 Pair production . . . 77

4.2.4 Detectors . . . 77
4.2.5 Improved Si(Li) detector resolution . . . 78
4.2.6 Data acquisition . . . 79
4.2.7 LEPS and $LaBr_3$:Ce detection efficiency . . . 81
4.3 Data analysis for ^{70}Ge(α,X)Y reaction . . . 82
4.3.1 Total reaction cross section . . . 83
4.3.2 Gain shift corrections . . . 84
4.3.3 K and L separation . . . 88
4.4 ANU experimental setup . . . 91
4.4.1 Experiment using ^{54}Cr target . . . 93
4.4.2 Data acquisition system . . . 95
4.4.3 Detection efficiency of the ANU spectrometer array . . . 96
4.4.4 HPGe detector efficiency . . . 96
4.4.5 Super-e detection efficiency . . . 97
4.4.6 Simulation of internal pair efficiency . . . 98
4.5 Data analysis for ^{54}Cr$(p,n)^{54}$Mn reaction . . . 100
4.5.1 Kinematics calculations of ^{54}Cr$(p,n)^{54}$Mn reaction . . . 103

5 Results and Discussion **105**

5.1 ^{70}Ge experiment results . . . 105
5.1.1 Extraction of internal conversion coefficients . . . 111
5.1.2 Extraction of $q_K^2(E0/E2)$ and $\rho^2(E0)$ values . . . 115
5.1.2.1 Extraction of half-life for 691 keV transition . . . 118
5.1.3 Extraction of the difference in $\langle r^2 \rangle$ and $\langle \beta_2 \rangle$ in ^{72}Se . . . 120
5.1.4 Extraction of $B(E0)$ in ^{72}Se . . . 121
5.2 Summary of ^{70}Ge(α,X)Y results . . . 122

5.3 ^{54}Cr experiments results . . . 123
5.3.1 Extraction of spectroscopic information in ^{54}Mn . . . 124
5.3.2 Internal conversion coefficients (α_K) . . . 127
5.3.3 Internal pair coefficient (α_π) . . . 131
5.3.4 Partial decay scheme for ^{54}Mn . . . 132
5.3.5 Mixing ratio $\delta(E2/M1)$ . . . 133
5.3.6 The $q_K^2(E0/E2)$ and $\rho^2(E0)$ values for ^{54}Mn . . . 134
5.3.7 Summary of ^{54}Mn data . . . 135
5.4 Theoretical calculations . . . 136
5.4.1 Collective Hamiltonian calculations . . . 136
5.4.2 NuShellX calculations for ^{54}Mn . . . 140

6 Conclusions and Recommendations **144**

Bibliography **146**

A Pumping and venting procedure **160**

B Remote control system **162**

C Spectrometer earthing **163**

List of Figures

1.1 The ratio of $E0_i^+$ to $E2_1^+$ energies as a function of neutron number for Zn, Ge, and Se isotopes with even-mass. The data are taken from Ref. [Pas85]. 3

1.2 A square section of the nuclear chart showing the region of interest. The stable isotopes are shown in the black boxes, the β^- decaying isotopes are shown in blue boxes, the β^+ decaying isotopes are shown in the yellow and grey boxes, respectively. The image is taken from the NuDat data base. 4

2.1 Shell model calculations using ca48mh2g interaction [Hon04] for the low-lying positive parity states in ^{54}Cr compared with experimental results from [Don14]. 14

2.2 Partial level scheme of ^{54}Cr illustrating the occurrence of a pure E0 transition and mixed multipolarities. The highlighted states are transitions of interest in this study. 29

2.3 An illustration of nuclear reaction mechanism. P is the beam, T is the target, X is the outgoing particle and R is the recoil. 37

3.1 Transverse geometry of the magnetic lens showing the physical geometry of the lens and associate component. Courtesy of INIT Department, iThemba LABS. The beam travels into the page. . . 49
3.2 Overview of the meshed model of magnetic field in steel obtained from OPERA 3D simulation. 50
3.3 Axial magnetic field component for four current settings. The simulation is shown by solid lines and the points represent the measured fields. 51
3.4 The vacuum scheme of the spectrometer showing the gate valves, target position and detector position. TMP1 and TMP2 represent the turbo molecular pump 1 and 2 respectively, while V-1:V-8 represent valves 1 - 8. 53
3.5 Target system showing control system, beam direction, target chamber (left) and the 4 target positions (right). 53
3.6 A rear view of the spectrometer door showing the PT100 sensor on the cold plate and the 5 mm thick Si(Li) detector 55
3.7 Cooling curve of the cold plate and Si(Li) detector (upper) with nitrogen consumption rate (lower). 56
3.8 Measured axial magnetic flux density as a function of current at the centre of the solenoid (250 mm on the axis). The red line is a linear fit to the data points. 57
3.9 B vs E matrix measured with a ^{207}Bi source. Measurements with baffle (upper) and measurement without baffle (lower). The lines represent the momentum window calculated using Eq. (3.2) discussed in Section 3.5.2 59

3.10 An overview of Geant4 simulations of electron trajectory emerging from the source point into the solenoid magnetic field. Without baffle (upper) with baffle (lower) [Chi19]. 60
3.11 Demonstration of background reduction by the baffle system using ^{207}Bi source. The momentum gate was set on the 1064 K conversion electrons. 61
3.12 The acceptance window for the 1064 K transition in ^{207}Bi. 62
3.13 Experimental (red circles) and simulated (black triangles) rigidity curves constructed to show the B-E dependence deduced from the momentum distribution for ICE emitted from the decay of ^{207}Bi and ^{133}Ba. The purple squares and the red circles represent the data points from ^{133}Ba and ^{207}Bi, respectively. The solid and dashed lines are the fits to the experimental and simulated data points, respectively. 63
3.14 Simulated Si(Li) detector efficiency from the total spectrum. The red line is a linear fit to the simulated points. 66
3.15 A typical momentum gated conversion electron spectrum of ^{207}Bi used to determine the spectrometer efficiency. 66
3.16 Comparison of measured absolute spectrometer efficiency (squares) with simulations (circles) for electrons from ^{133}Ba and ^{207}Bi sources. 67

4.1 Reaction cross section for possible decay channels. 71
4.2 A screenshot of post target beam spread inside the beam pipe. The target position is at 0 mm. 72
4.3 Number of scattered ions along the radial axis of the beam pipe. (a) at 390 mm, (b) at 585 mm, (c) at 780 mm. 73

4.4 Overview of Compton scattering by an incident gamma ray, θ is the scattering angle and ϕ is the recoil angle. 76
4.5 Side view of the spectrometer array (upper) showing the 1: LEPS, 2: the beam line, 3: $LaBr_3$:Ce detectors, 4: target ladder, 5: magnetic lens, 6: Si(Li) cold finger and 7: Dewar used for the measurements. Front view (lower). 79
4.6 ICE singles spectra of ^{133}Ba. Red line is measurement with the eight baffle system and blue line is measured with the straight baffle. 80
4.7 Block diagram of the digital data acquisition system showing the detectors and associated electronics. The HPGe are the LEPS detectors, each have 4 signal cables, while the $LaBr_3$:Ce provide fast and slow signals. 81
4.8 Plot of total absolute efficiency of the LEPS detectors (blue circles) and $LaBr_3$:Ce (red squares). The lines represent an exponential fits to the efficiency data points. 82
4.9 Plot of counts versus time of the six $LaBr_3$:Ce detectors. 84
4.10 Gain drift in one of the $LaBr_3$:Ce (upper) and segment d of the LEPS detector (lower) for the low energy and high energy peaks. . 86
4.11 Gain drift corrected in one of the $LaBr_3$:Ce (upper) and segment d of the LEPS detector (lower) for the low energy and high energy peaks. 86
4.12 Plot of the difference in the centroid of the conversion electron peaks relative to the reference spectrum as a function of time. . . 87

4.13 Magnetic flux density vs $LaBr_3$:Ce detector 1 energy matrix. Top without gain correction, bottom gain corrected. 88
4.14 A plot showing the gain corrected spectrum from the $LaBr_3$:Ce detectors overlaid with a spectrum with gain drift. 89
4.15 A sample spectra of CE showing a fit of the overlapping K and L shell electrons. The χ^2 is about 1.5 as shown in fit parameters. . . 90
4.16 Exterior view of the experimental setup used for the ANU measurements. 92
4.17 A cross sectional view of the solenoid showing the short and long end (A, B) of the coils, 1: beam line, 2: target, 3: coils, 4: detector. 92
4.18 Image of the Super-e showing the target, baffles, Miel array, and envelope of trajectories [Kib12]. 93
4.19 Level scheme showing adopted gamma rays for ^{54}Cr [Don14]. . . 94
4.20 A block diagram of electronics used for data acquisition and processing. 96
4.21 Relative efficiency of MUX2 detector, a normalization factor of 8.349 was used to combine the data from ^{152}Eu (black squares) and ^{56}Co (blue circles). The blue triangles are points excluded from the evaluation. 97
4.22 Relative efficiency of Super-e spectrometer calculated with Monte Carlo code compared with data point from the ^{170}Lu source. . . . 98
4.23 The double differential pair emission rate for the 2848 keV $M1$ transition from Lens IPF [Kib20]. 99
4.24 Simulated absolute pair efficiency for the individual multipolarities for each transitions of interest using three magnet current settings. 101

4.25 Time difference spectrum showing the three TDC regions. T_{bgL} is the background left, T_{bgL} is the background right and T_{Pr} is the prompt region. A factor of 0.1863 is obtained from these limits and used in scaling the pair spectrum according to sampling time. . . 103
4.26 Projected magnetic field for pair conversion measurements. The three peaks correspond to the field settings. 104

5.1 Level scheme showing adopted gamma rays for ^{70}Ge taken from [Abr10]. 106
5.2 Level scheme showing adopted gamma rays for ^{72}As taken from [Abr10]. 106
5.3 Level scheme showing adopted gamma rays for ^{72}Se taken from [Abr10]. 107
5.4 Singles spectra. (a) Gamma rays detected with $LaBr_3$:Ce detectors, (b) Gamma rays measured with LEPS detectors, (c) Conversion electrons from the Si(Li) detector gated on the momentum window. The conversion electron peaks are shifted up by the K shell binding energy of ^{72}Ge to align with the transition energy. 108
5.5 Magnetic flux density versus energy matrix from the α-induced reaction. The red lines represent the momentum window calculated using Eqn. (3.2). 109
5.6 A coincident matrix for the $LaBr_3$:Ce versus Si(Li) energies from the ^{70}Ge experiment. 109
5.7 Sample of gated background subtracted ICE spectra projected from the e-γ matrix. Upper: gated on 53 keV gamma rays, Lower gated on 96 keV gamma rays. 110

5.8 Background subtracted γ-ray spectra projected from the e-γ matrix. Gates are placed on $(4_1^- \rightarrow 3_1^+)$ and $(3_1^+ \rightarrow 1_1^+)$ transitions. Upper: gated on 96 keV conversion electron transition, Lower gated on 167 keV conversion electron transition. 110

5.9 Experimental K conversion coefficients (diamond) compared with theoretical values from BrIcc [Kib08] values (smooth lines). . . . 112

5.10 Experimental L conversion coefficients, α_L (triangles) compared with theoretical values from BrIcc [Kib08] (smooth lines). 115

5.11 Partial level scheme for ^{72}As deduced from e-γ coincidence. Spin-parity assignment and energy levels were adopted from [Abr10]. Blue denotes transitions whose ICC has been measured in this study. 116

5.12 Partial level schemes of populated states in ^{72}Ge (left) and ^{72}Se (right). The red denotes $E0$ transitions. Spin-parity assignment and energy levels were adopted from [Abr10]. 116

5.13 Total projection conversion electron coincidences form the ^{70}Ge experiment. 117

5.14 The time difference spectrum between a $LaBr_3$:Ce and the Si(Li) detector corresponding to all the events. 119

5.15 ICE spectra projected from the e-γ matrix. Gate is on the 773 keV gamma ray. 120

5.16 (a) Singles γ-ray and (b) conversion-electron spectra measured simultaneously with swept magnetic field. The peaks are shifted by the binding energy of the K conversion electrons to align with (a). (c) Pair sum spectrum measured with stepped field and is shifted up in energy by $2m_0c^2$ to reflect the transition energy. The data are presented from 1000 keV to 3000 keV since no transitions with corresponding conversion electrons or pairs were detected outside of this range, and for clarity, some gamma ray transitions were not labelled. 124

5.17 Level scheme showing adopted gamma rays for ^{54}Mn [Don14]. . . 125

5.18 The magnetic flux density vs energy matrix. The solid lines represent the momentum window calculated according to Eq. (3.2) using the energy-field relationship coefficiencts for Super-e [Kib20]. 126

5.19 Experimental K conversion coeffcients compared with BrIcc values. The green triangle denotes the normalization transition. 129

5.20 The ratio of experimental K conversion and pair coefficients to theoretical values for the transitions of interest in ^{54}Mn. The $E2$ shown here is the normalization transition 131

5.21 Partial decay scheme of ^{54}Mn from the (p,n) reaction showing excitation energies up to 2.9 MeV. In addition, the γ-ray energies and multipolarities are given. Blue denotes the new assigned multipolarities. 133

5.22 A plot of χ^2 for the 1226 keV transition as a function of arctan(δ). 134

5.23 Calculated energies from the 5DCH-CDFT of the 0^+, 2^+, 4^+ states in ^{72}Ge compared with experimental results [Abr10]. 137

5.24 Calculated energies from the 5DCH-CDFT of the 0^+, 2^+, 4^+ states in ^{72}Se compared with experimental results [Abr10]. 137

5.25 Excitation energies from Shell model calculations compared with experimental results [Don14] for the 1^+, 2^+ and 3^+ from ^{54}Mn. The energies are given in MeV. 142

B.1 The Experimental Physics and Industrial Control System (EPICS) showing the liquid nitrogen, power supply and cryogenics systems 162

C.1 Earthing of various components of the spectrometer to minimize noise. 164

List of Tables

3.1 Measured and simulated FOM of the spectrometer using the 1064 K conversion electrons from ^{207}Bi. 67

4.1 Reactions characteristics of the alpha induced reaction on ^{70}Ge target. 74

4.2 The ratio of K to L shell electrons from ^{72}As ^{72}Ge and ^{72}Se compared with previous measurements 90

4.3 Summary of runs for ^{54}Cr measurement with Super-e spectrometer at $E_p = 5.4$ MeV. 95

4.4 Numerical values for the simulated pair efficiencies. The uncertainty in the transmission is ∼1 % and ∼5 % for the detection efficiencies. 102

4.5 Reactions characteristics of the proton induced reaction on ^{54}Cr target. 104

5.1 Gamma ray and K conversion electron coincident peak areas and intensities. 111

5.2 Adopted multipolarities from [Abr10] and experimental K conversion coefficients, α_K compared with theoretical values from BrIcc for the observed transition in ^{72}As, ^{72}Ge and ^{72}Se. 113

5.3 Experimental L conversion coefficients, α_L compared with theoretical values for the observed transitions in ^{72}As and ^{72}Ge. 114
5.4 Measured intensities, the ratio $q^2_K(E0/E2)$ and the $E0$ strength for ^{72}Ge and ^{72}Se compared with literature values. 121
5.5 List of gamma rays observed but not labelled in Fig. 5.16 123
5.6 Adopted multipolarities, measured intensities and conversion coefficients compared with theoretical coefficients for ^{54}Mn nucleus. . 130
5.7 Adopted multipolarities, intensities and internal pair coefficients (α_π) compared with theoretical coefficients from BrIcc. 132
5.8 Summary of adopted multipolarities, deduced mixing ratios for the observed transitions, the, intensity ratio and monopole strength $\rho^2(E0)$. Uncertainty within 1 σ were not quoted. 135
5.9 Electromagnetic transition probabilities from 5DCH-CDFT calculations for ^{72}Ge compared with experimental values taken from [Abr10]. The standard deviation (SD) of the theoretical $B(E2)$ with calculated values are presented. 139
5.10 Electromagnetic transition probabilities from 5DCH-CDFT calculations for ^{72}Se compared with experimental values taken from [Abr10]. The standard deviation (SD) of the theoretical $B(E2)$ with calculated values are presented. 140
5.11 Transition probabilities from SM calculations for ^{54}Mn compared with experimental values taken from [Don14]. The standard deviation (SD) between the experimental values and theoretical values are also shown 143

Chapter 1

Introduction

The study of gamma rays from the decay of an excited nucleus provides some insight into the nuclear structure. However, probing the nuclear structure by gamma ray detectors alone can provide only a limited view of the nuclear de-excitation processes as the decay of an excited nucleus does not only proceed via gamma-ray emission. There are other competing modes of de-excitation such as emission of internal conversion electrons (ICE) and internal pair formation (IPF) [Kan95]. Due to the intrinsic angular momentum of the photon, a transition between states, with zero spin and identical parity (e.g., $0^+ \rightarrow 0^+$) is forbidden by single-photon emission [Chu56]. However, it can proceed as an electric monopole $E0$ transition via the emission of conversion electrons or electron-positron pairs, with the latter being possible only when the transition energy exceeds the combined rest mass of the electrons and positrons [Kib05]. $E0$ transitions can also occur between states with the same spin and parity where $J^\pi \neq 0$ (e.g., $2^+ \rightarrow 2^+$).

The physical feature behind the $E0$ transition is that the spin and parity of the two states must be the same in a nucleus enclosed by electrons. If the $E0$ transition is emerging from a very deformed to a less deformed state, the charge

state distribution will change, giving rise to the $E0$ transition strengths. Thus, the $E0$ strength, $\rho^2(E0)$, is a veritable probe of the charge distribution of an atomic nucleus and by extension a powerful tool for studying shape coexistence and mixing. For example, the measurements of $E0$ transition strengths and the energies of the excited 0^+ states in ^{70,72}Ge [Dra74, Pas85] and ^{54}Fe [Tho18] led to the interpretation of shape coexistence in this mass region. Measurement of $E0$ transition strength is the focus of this study, a brief overview of previous related studies shall be discussed in the following sections, while a detailed theory of the $E0$ transition will be discussed in Chapter 2.

1.1 *E*0 transitions in the mass 70 region

The electric monopole $\rho^2(E0)$ strength from the decay of $0_f^+ \rightarrow 0_i^+$ was used to study the structure of the low-lying states in $^{70-72}$Ge [Dra74, Pas85, Cho94], and ^{72}Se [Dra74, Cho94]. For many decades, the even-mass Ge isotopes have been the subject of debate due to the anomaly in the first excited 0_2^+ state which makes it difficult to elucidate their systematics with change in mass number [Pas85, Aya16]. In addition, the energy of the 0_2^+ state changes with increase in neutron number, N, and becomes the first excited state in ^{72}Ge [Pas85]. This anomaly, also inferred from the abrupt discontinuity at N=40 in the ratio $E(0_i^+)/E(2_1^+)$ of even-mass Zn, Ge, and Se isotopes as shown in Fig. 1.1, has been ascribed to pure neutron/proton excitations [Ver80, Pas85].

Accordingly, the first excited 0^+ state in ^{72}Se has been found to occur at an excitation energy of less than 1.0 MeV [McC11]. This is a prime signature of shape coexistence as the 0_2^+ state is only 75 keV above the first excited 2_1^+ (862 keV) state.

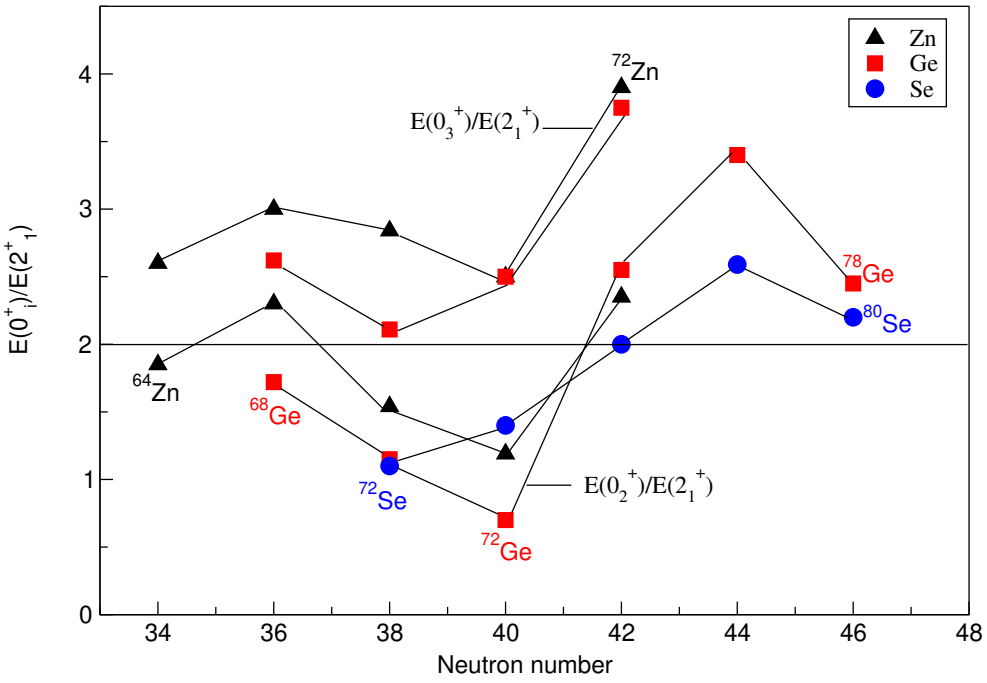

Figure 1.1: The ratio of $E0_i^+$ to $E2_1^+$ energies as a function of neutron number for Zn, Ge, and Se isotopes with even-mass. The data are taken from Ref. [Pas85].

Another uncommon feature observed in ^{72}Se is that the energy of the $4_1^+ \rightarrow 2_1^+$ transition is less than that of the $2_1^+ \rightarrow 0_1^+$ transition, which is contrary to other even-mass Se isotopes ($^{74-78}$Se) [Ham74, McC11]. The interpretation of shape coexistence in these nuclei was based on the measured strength and other properties of the $E0$ transitions [Dra74, Ham74]. Although this mass region has been studied previously, it remains under scrutiny, and as such, more experimental evidence is needed to supplement and fully understand the unusual properties exhibited by these nuclei. Furthermore, additional experimental information is required in the mass 70 region to elucidate the competition between various configurations at different deformations.

1.2 $E0$ transitions in the mass 50 region

The monoploe strength $E0$ in ^{54}Fe from a $0^+_f \rightarrow 0^+_i$ transition was measured in the 1970's [War72] while that of the $2^+_f \rightarrow 2^+_i$ transition in the same nucleus was recently measured by [Tho18]. This region is of special interest as it lies between two doubly-magic nuclei, ^{40}Ca in the south west and ^{56}Ni in the north east as shown in Fig. 1.2. These nuclei exhibit strong evidence of super-deformation, which is interpreted as shape coexistence [Ide01, Ban14, Pat15].



Figure 1.2: A square section of the nuclear chart showing the region of interest. The stable isotopes are shown in the black boxes, the β^- decaying isotopes are shown in blue boxes, the β^+ decaying isotopes are shown in the yellow and grey boxes, respectively. The image is taken from the NuDat data base.

However, experimental information on $E0$ transitions in the mass 50 region is

lacking, there is no experimental data available on $E0$ transitions in ^{52}Cr, ^{50}Ti and in neighbouring ^{54}Cr and ^{54}Mn. It is therefore, imperative to investigate the main nuclear features in this region through $E0$ transitions as the electric monopole strength parameter carries significant information about the nuclear structure [Woo99, Kib05].

1.3 Present work

The main aim of this study is to refurbish and recommission the electron spectrometer for $E0$ transitions studies at iThemba LABS. To this end a test reaction was used to investigate the underlying nuclear structure of the lowest excited states in ^{72}Se, ^{72}Ge, ^{72}As via alpha-induced reactions on a ^{70}Ge target. In addition, ^{54}Cr will be probed utilizing a (p, p$'$) reaction to search for shape coexistence in ^{54}Cr. Measurements of $E0$ transitions in these nuclei through ICE and IPF measurements was achieved. The relationships between the measured monopole strength $\rho^2(E0)$ parameter with other extracted spectroscopic information, namely, change in the mean square charge radius, $\Delta\langle r^2\rangle$, transition probabilities, $B(E2)$, $B(E0)$, and quadrupole deformation β_2 was utilized to elucidate the nuclear structure of the low-lying states in these nuclei. Theoretical calculations of the excitation energies, transition probabilities and monopole strength using the state-of-the-art shell model and five-dimensional collective Bohr Hamiltonian based on the covariant density functional theory (5DCH-CDFT) were performed and the results compared with experimentally deduced values where available. In addition, unambiguous assignment of multipolarities was achieved using the ICC and IPF extracted from the observed transitions in these nuclei.

1.4 Structure of the thesis

Having stressed the intent of the study and how this could be achieved, an overview of atomic structure and nuclear theory relevant to this study are detailed in Chapter 2. Nuclear models are presented, followed by experimental observables and their connection with nuclear structure.

In Chapter 3, a comprehensive review of spectrometers previously used in internal conversion electron studies is given along with detailed description of work done on the refurbished electron spectrometer at iThemba LABS. Secondly, an overview of calibrations carried out to characterize the spectrometer and the extracted Figures of Merit are presented.

In Chapter 4, nuclear reactions are introduced. A guide to experimental techniques which includes, firstly, equipment used for measurements of decay radiation and the setup for the iThemba LABS experiment. In addition, the complementary experiment performed at the Australian National University Heavy Ion Accelerator Facility (ANU HIAF) is discussed. Data extraction and analysis techniques for the two sets of measurements are also presented.

Detailed results of the measurements are presented and discussed extensively in Chapter 5. Where applicable, the experimental values are compared with previous measurements and theoretical results. In Chapter 6, the thesis is concluded with a brief discussion of the success story of the commissioning experiment, the experiment at ANU, recommendations and future plans.

Chapter 2

Theoretical Review

The atomic nucleus is a many-body quantum mechanical system governed by single particle and collective excitations. The goal of nuclear physics is to provide a clear understanding of the structure and dynamics of nuclei. To realize this goal, measurements of electromagnetic transitions are required. Radiations emitted from the decay of excited states such as gamma emission, internal conversion electrons and pair formation carry information about the nuclear properties needed to elucidate the shape of the atomic nucleus. In this chapter, a review of atomic and nuclear models together with types of electromagnetic transition is presented.

2.1 Atomic theory

The atom has been described by Neils Bohr and Ernest Rutherford as a system comprising of a small dense nucleus with electrons orbiting around it [Tol57]. Taking the particle-like approach to the electrons with mass m rotating around the atomic nucleus in their orbit of radius r, the electrons will experience a centripetal

force due to Coulomb attraction between the electron and the proton. When an electron is in its lowest orbit, its acceleration does not result in radiation and energy loss. However, when the electron is excited to a higher orbit, it de-excite by releasing a quantum of electromagnetic radiation. The energy emitted is determined by the difference in energy of the two orbits according to Planck's constant

$$h\nu = E_f - E_i, \tag{2.1}$$

where h and ν are the Planck's constant and frequency of the radiation connecting the two states, respectively. E_f and E_i are the energies of the final and initial state respectively.

2.1.1 Atomic shells

According to the Pauli Exclusion Principle [Wol25], the maximum number of electrons that can occupy an orbit with principal quantum number n is $2n^2$. In other words, two electrons cannot be described by the same four quanta numbers, namely the principal quantum number n, angular momentum quantum number l, magnetic quantum number m_l, and spin quantum number m_s [Yar58]. The coefficient 2, typify the two-spin orientation of an electron. Based on the possible values of the principal quantum number (n = 1,2,3,...), the maximum number of electrons corresponding to n is 2, 8, 18, etc. It is also shown from Pauli principle that for any given value of n, only $2(2l + 1)$ electrons is allowed with any specific value of orbital angular momentum l. All electrons with the same total quantum number n thus belong to the same shell designated as K, L, M, N, etc. That is, for $n = 1$, the 2 electrons will occupy the K shell and for $n = 2$, the 8 electrons will be in the L shell, etc. An atom is most stable when it has minimum energy,

thus, it will first fill the lowest energy level to attain the state of minimum energy. Therefore, the K shell which is closer to the nucleus is filled first followed by the L, etc. The total number of electrons in filled electronic shells are 2, 10, 18, 36, 54, and 86, these are the atomic magic numbers. The chemical properties of an atom are exclusively determined by the number of valence electrons which is fixed by the nuclear charge [Tol57]. The addition of electrons to the electronic structure will change the atomic configuration.

2.2 Nuclear models

In atoms, the Coulomb interaction between the electrons and the nucleus is responsible for the motion of electrons in their orbits. In the nucleus, the nucleons are bound to each other by a nuclear force. Attempts to describe the nature of this force is usually difficult due to the fact the nucleus is a many-body system of individual protons and neutrons [Yan96]. As a result of these ambiguities, many nuclear models have been proposed to interpret approximately the motion of the nucleons and the nuclear structure. Nuclear models can be divided into independent particle models in which the nucleons are assumed to be moving independently and the collective (strong interaction) model in which the nucleons move collectively due to strong coupling [Fra74, Yan96]. A straightforward example of the collective model is the "liquid drop model". An example of an independent particle model is the shell model which is discussed in the next subsection.

2.2.1 The concept of the shell model

An ideal model required to describe the nuclear behaviour must be able to predict new properties to search for in future experiments besides accurately reproducing previous measured properties. There has been substantive evidence in support of the agreement between measured atomic properties and the ones predicted by the shell model of the atom.

Nuclear properties such as nucleon separation energies which show discontinuities of the same type as those observed in atomic ionization potentials [Boh69] suggest the existence of nuclear shell structure. Another feature that shows the existence of shell structure is the large discontinuities that occur in nuclei with neutron numbers 2, 8, 20, 28, 50, 82, and 126 [Boh69]. These numbers are called "magic" numbers and are counterpart in nuclear structure to atomic numbers described in subsection 2.1.1. It will require an enormous amount of energy greater than the binding to remove a nucleon from the nucleus because they are tightly bound. Other evidence for shell structure as stated in [May49] are excitation energies of states at closed shells and level densities.

The aforementioned magic numbers can be reproduced by a theoretical model by choosing a suitable potential for the nucleus together with spin-orbit coupling [Hax49]. Such a potential is due to the nucleons themselves contrary to the central Coulomb potential in the atomic systems where negatively charged electrons are orbiting a positively charged nucleus [Som18]. This is because nuclear shell model includes an attractive potential arising from the short-range interaction between neighbouring nucleons which is directly dependent on the shape of the nuclear distribution [Dav10, Lea15]. Therefore, the shell model can treat each nucleon as an independent particle that moves within a mean field

of all the rest, thus allowing nucleons to occupy the various orbitals within the shells. These fundamental ideas constitute the description of nuclear structure within the framework of the shell model, as well as characterizing the formalism for single-nucleon transfer reactions [Dav10]. Two of the occasionally lesser used potentials are the infinite well and the harmonic oscillator. Therefore, starting with harmonic oscillator, which has spherical symmetry, the potential $V(r)$ is defined in terms of the nucleon mass m, frequency ω and nuclear radius r as

$$V(r) = \frac{1}{2}m\omega^2 r^2. \tag{2.2}$$

The solution of the infinite well and the harmonic oscillator potential solved in three dimensions by the Schrödinger equation given in

$$\frac{-\hbar^2}{2m}\nabla^2\Psi(r) + (V(r))\Psi(r) = E\Psi(r), \tag{2.3}$$

would produce equally spaced energy levels (2, 8, 20, 40, 70, 112) as shown in Fig. 2-21 of Ref. [Boh69]. The number of nucleons that can occupy each energy levels is defined by $2(2l+1)$, due to degeneracy of both the spin s and magnetic quantum numbers m. However, not all the magic numbers were reproduced because of degeneracy, the same energies were produced in different quantum state. The harmonic oscillator is also unrealistic at large nuclear radius. Hence, the need to choose an intermediate form that is more realistic. The Wood-Saxon potential $V(r)$ which nearly reproduces the charge distribution of a nucleus is the available alternative. The Woods-Saxon potential is parameterized as

$$V(r) = -\frac{V_0}{1 + Exp[(r - R_{av})/s]}, \tag{2.4}$$

where R_{av} is the nuclear average radius defined by the expression

$$R_{av} = 1.25A^{1/3}, \tag{2.5}$$

V_0 represent the well depth and s is the skin thickness (the radius of the nucleus in which the charge density decreases to minimum) whose value is usually around 5-6 fm [Cho15, Sor16]. However, the magic numbers shown in [May49] could not be replicated. In 1949 Goeppert-Mayer and Jensen [May49] proposed the inclusion of an additional term that describes the spin-orbit interaction which was able to reproduce the pattern of magic numbers and defined what is known as the (non-interacting) nuclear shell model.

2.2.2 Nuclear spin-orbit coupling

The nuclear spin-orbit coupling force is stronger and has an opposite sign than the spin-orbit coupling in atoms. The strong force that gives rise to the coupling is also of a different origin from the spin-orbit coupling in atomic electrons. The spin-orbit coupling in nuclei is related to the force between nucleons, it is responsible for the splitting of the energy levels into two labelled by the orbital angular momentum l such that the single particle angular momentum $j = l \pm s$. The spin-orbit splitting is proportional to (2l+1). For a given value of l, $l + \frac{1}{2}$ lies lower in energy with a degeneracy of $2j + 1 = 2l + 2$. The $l - \frac{1}{2}$ lies higher because of the change of sign of the spin-orbit coupling in nuclei [Fra74, Yan96]. The strong coupling of the spin and the orbital motion of the nucleons with opposite sign is fundamental to produce energy splitting (shell gaps) consistent with experimental spherical nuclear magic numbers [Yan96].

2.2.3 The interacting shell model

Although an independent-particle model could explain the basic features of nuclear structure like magic numbers and the existence of closed-shell nuclei. In general a correlated wave function is needed to decompose the total Hamiltonian in a mean-field H_{MF} and a residual part H_{res}, expressed as

$$H = H_{MF} + H_{res}. \tag{2.6}$$

The residual part requires diagonalization in the valence space (A-body Hilbert space) [Som18]. To achieve this, the excitations across major shells are suppressed [Som18]. In principle, to a first approximation, a given major shell can be probed independently of the others. This idea is at the rudiment of the interacting shell model and is implemented by first, defining an active valence space. Followed by building a valence-space Hamiltonian, H_{val}^{eff} and lastly, by diagonalizing the H_{val}^{eff} in the reduced space [Som18]. The diagonalization of the Hamiltonian usually yields the single particle energies. To diagonalize the Hamiltonian different shell model codes have been developed, namely OXBASH [Bro85], NuShellX [Bro14] etc. A brief overview of the NuShellX formalism is discussed in subsection 2.2.4. The success of the interacting shell model is seen in its ability to perform calculations well beyond the region reachable by fullspace diagonalization. However, it has limitations as it is unable to describe the structure of nuclei in the heavy mass region due to large amount of unpaired nucleons [McG70, Hjo95, Pov11, Som18]. It is also unable to predict the monopole transition probability $B(E0)$. As an example, the Kshell model [Shi13] calculations for ^{54}Cr were made using the pf-shell model space and ca48mh2g effective interaction [Hon04], the results is compared

with experimental values in Fig. 2.1. The low-lying ground-state band levels were reproduced, however, the 0^+ band could not be reproduced.

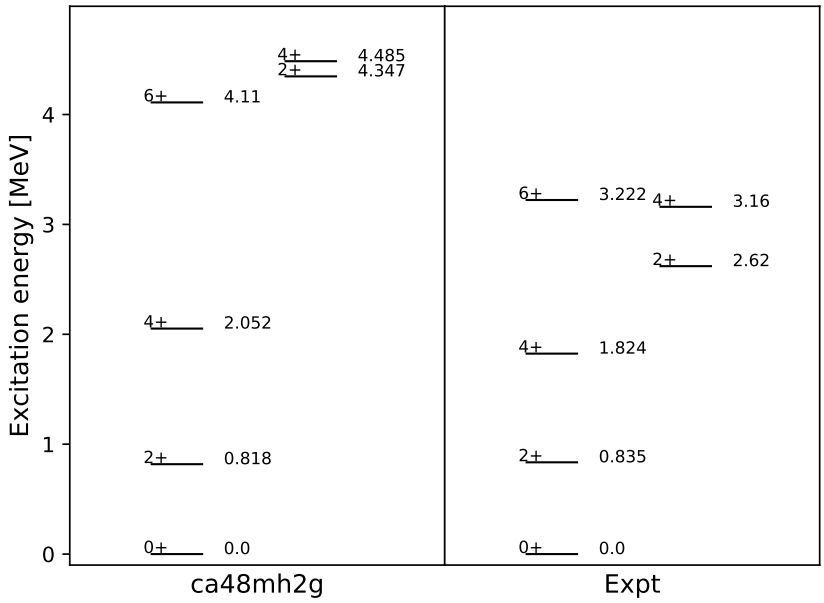

Figure 2.1: Shell model calculations using ca48mh2g interaction [Hon04] for the low-lying positive parity states in ^{54}Cr compared with experimental results from [Don14].

2.2.4 NuShellx Formalism

The Nushellx code [Bro14] uses an effective Hamiltonian in each model space, which is diagonalized to get the wave functions. The Hamiltonian is written as a sum of three terms

$$H = H_{pp} + H_{nn} + H_{pn}, \tag{2.7}$$

where H_{pp} is the Hamiltonian of the proton-proton and H_{nn} is the Hamiltonian of the neutron-neutron interactions. While H_{pn} is the Hamiltonian describing the

proton-neutron interaction. The H_{pn} can be quantised to have the configuration

$$H_{pn} = \sum_{pnp^{'}n^{'},J_0} \left\{ \left[a_p^+ a_n^+ \right]^{J_0} \otimes \left[\tilde{a}_{p^{'}} \tilde{a}_{n^{'}} \right]^{J_0} \right\}^{(0)}, \tag{2.8}$$

where a_p^+ denotes the proton operator and a_n^+ is the neutron operator. The quantity J_0 is single angular momentum operator while $p^{'}$ and $p^{'}$ are the proton and neutron conjugates. The proton-neutron Hamiltonian, H_{pn} can also be written in the particle-hole form as [Bro14]

$$H_{pn} = \sum_{pp^{'}nn^{'},\lambda} F_\lambda \left(pp^{'}nn^{'} \right) \left\{ \left[a_p^+ \tilde{a}_{p^{'}} \right]^\lambda \otimes \left[a_p^+ \tilde{a}_{n^{'}} \right]^\lambda \right\}^{(0)}, \tag{2.9}$$

where

$$F_\lambda \left(pp^{'}nn^{'} \right) = -\sum_{J_0} \sqrt{(2\lambda+1)(2J+1)(-1)^{n+p^{\lambda}-\lambda-J_0}} \begin{Bmatrix} p & n & J_0 \\ n^{'} & p^{'} & \lambda. \end{Bmatrix} \tag{2.10}$$

The NuShellX basis states are defined in [Bro14] by

$$|B, J\rangle = |[(J_p, \alpha_p) \otimes (J_n, \alpha_n)]\, J\rangle\,, \tag{2.11}$$

where J_p, α_p, J_n and α_n are the proton and neutron matrix elements. A detailed description of the coupling of the operators and how the matrix elements are defined is given in [Bro14]. By utilizing the effective g-factors and the effective charges described in [Hon04], the electromagnetic transition matrix elements are evaluated.

2.2.5 Collective Bohr Hamiltonian

The various features of the spectra associated with shape deformation of quadrupole symmetry can be described by a set of five amplitudes $\alpha_{2\mu}$ that make up the spherical tensor [Boh75]. Such deformations produce an ellipsoidal shape for small amplitudes. The principal axes of the deformed shape defines an intrinsic coordinate system whose orientation angles $\omega = (\phi, \theta, \psi)$ are related to the amplitude by

$$\alpha_{2\mu} = \sum_{\nu} a_{2\nu} \mathfrak{D}^{2}_{\mu\nu}(\omega), \tag{2.12}$$

where $a_{2\nu}$ is the nonvanishing intrinsic deformation variable and $\mathfrak{D}_{\mu\nu}$ is an orthogonal expansion function of the orientation angle ω. The quantity μ and ν is the magnetic dipole moment and the band matrix element, respectively. The parameters (ϕ, θ, ψ) are called Euler angles [Boh75, Shi18] and will be referred to as Euler angles throughout the text. The two non-vanishing intrinsic deformation variables are usually designated in terms of the shape parameters β and γ. The potential energy of the nucleus does not depend on the nuclear orientation but on the shape parameters. Thus, the potential energy function can be rendered as

$$V = V(\beta, \gamma). \tag{2.13}$$

While the kinetic energy T involves the vibrational and rotational component of the nucleus. It can, therefore, be written as the sum of vibrational and rotational kinetic energies [Boh75]

$$T = T_{vib} + T_{rot}. \tag{2.14}$$

The quadrupole Hamiltonian describes a variety of different types of collective motion controlled by the potential energy function V and the inertial parameters [Boh75]. In a situation where the potential energy function has a well defined minimum away from the origin, the quadrupole degrees of freedom split into vibrational and rotational components. The vibrations correspond to small amplitude oscillations about the equilibrium whereas, the rotation is characterized by the kinetic energy T and moments of inertia $\Im_k$.

The five-dimensional collective Bohr Hamiltonian that describes the quadrupole vibrational and rotational degrees of freedom is expressed in terms of the two deformation parameters β and γ as

$$\hat{H} = -\frac{\hbar^2}{2B_0}\left(\frac{1}{\beta^4}\frac{\partial}{\partial\beta}\beta^4\frac{\partial}{\partial\beta} + \frac{1}{\beta^2 sin3\gamma}\frac{\partial}{\partial\gamma}sin3\gamma\right) + \frac{1}{2}\sum_{k=1}^{3}\frac{\hat{J}_k^2}{\Im_k(\beta)} + V(\beta,\gamma), \quad (2.15)$$

where $\hat{J}_k$ is the component of angular momentum in the fixed-body frame and can be expressed as a function of Euler angles. The moments of inertia with respect to the body-fixed axis are given by

$$\Im_k = 4B_0(\beta)\beta^2 sin^2\left(\gamma - \frac{2\pi k}{3}\right), \quad (2.16)$$

where B_0 is a single mass parameter and k denotes the axis of rotation. To solve the eigenvalue problem with the Hamiltonian in Eq. (2.15), the eigenfunctions are expanded in terms of a complete set of basic functions that depend on the deformation variables β, γ and the Euler angles. For each value of angular momentum I, the basic functions are written as

$$\Psi_{IM}^{n_\beta v\alpha} = R^{(n_\beta,v)}(\beta)\Upsilon_{v\alpha IM}(\gamma,\Omega), \quad (2.17)$$

where $\Upsilon_{v\alpha IM}(\gamma,\Omega)$ are the spherical harmonics, which are the eigenfunctions of the operator $\hat{\Lambda}^2$

$$\begin{aligned}\hat{\Lambda}^2\Upsilon_{v\alpha IM} &= \left[-\frac{1}{\sin 3\gamma}\frac{\partial}{\partial\gamma}\sin 3\gamma\frac{\partial}{\partial\gamma}+\frac{1}{4}\sum_k\frac{\hat{J}_k^2}{\sin^2\left(\gamma-\frac{2\pi k}{3}\right)}\right]\Upsilon_{v\alpha IM} \\ &= v(v+3)\Upsilon_{v\alpha IM}.\end{aligned} \tag{2.18}$$

In addition to the angular momentum I and its projection M, each function $\Upsilon_{v\alpha IM}(\gamma,\Omega)$ is labelled by the seniority quantum number v and a multiplicity index α, which is required for $v \geq 6$ [Mar20]. In the following, both indices v and α will be replaced by the running index $n_\gamma = 0, 1, 2, \ldots$. The $\Upsilon_{v\alpha IM}(\gamma,\Omega)$ can be explicitly constructed as a sum over the states with explicit value of the projection K of the angular momentum on the intrinsic axis [Cap09],

$$\Upsilon_{v\alpha IM}(\gamma,\Omega) = \sum_{K=0,even}^{I}\mathcal{F}_{v\alpha I,K}(\gamma)\xi^I_{KM}(\Omega), \tag{2.19}$$

where

$$\xi^I_{KM}(\Omega) = \frac{1}{\sqrt{2(1+\delta_{K0})}}\left[D^I_{MK}(\Omega)+(-1)^I D^I_{M-K}(\Omega)\right], \tag{2.20}$$

and the $\mathcal{F}_{v\alpha I,K}(\gamma)$ are polynomials constructed from the trigonometrical functions of γ [Row10], where $D^I_{MK}(\Omega)$ is the Wigner D-function [Var88]. The potential energy $V(\beta,\gamma)$ in Eq. (2.15) is calculated in the frame of covariant energy density functional theory based on the relativistic mean-field with the NL3 parameter set which is discussed in the next subsection.

The collective quadrupole operator responsible for $E2$ transitions is ex-

pressed in the form

$$Q_{2\mu}^{coll} = \frac{3Ze}{4\pi} R_0^2 \left[\beta \cos\gamma D_{\mu 0}^2(\Omega) + \frac{1}{\sqrt{2}} \beta \sin\gamma \left(D_{\mu 2}^2(\Omega) + D_{\mu -2}^2(\Omega) \right) \right]. \tag{2.21}$$

In the case of the $E2$, reduced transition probability is given by the following expression

$$B(E2; I_i \to I_f) = \left(\frac{3}{4\pi} ZeR_0^2 \right)^2 \left(C_{I_i 0\, 20}^{I_f 0} \right)^2 |\langle f|\beta|i\rangle|^2, \tag{2.22}$$

where R_0 is the equivalent volume-conserving spherical radius of the nucleus, Z is the nuclear charge number and $C_{I_i 0\, 20}^{I_f 0}$ is the Clebsch-Gordan coefficient. The $M1$ reduced transition probability is calculated assuming the following expression for the $M1$ transition operator

$$(M1)_\mu = \mu_N \sqrt{\frac{3}{4\pi}} g_R(\beta) \hat{I}_\mu, \tag{2.23}$$

where μ_N is the nuclear magneton and $g_R(\beta)$ is the deformation-dependent collective g-factor. This form of the $M1$ transition operator is justified below. Thus,

$$B(M1; 2_i \to 2_f) = \mu_N^2 \frac{9}{2\pi} |\langle 2_f^+ | g_R(\beta) | 2_i^+ \rangle|^2. \tag{2.24}$$

The $E0$ transition strength $\rho^2(E0; I_i \to I_f)$ is calculated using

$$\rho^2(E0; i \to f) \equiv |\langle f|\mathcal{M}(E0)|i\rangle|^2 / (eR_0^2)^2, \tag{2.25}$$

Detailed formalism for the five-dimensional collective Bohr Hamiltonian is given in [Boh75, Pro09].

2.2.5.1 Covariant density functional theory (CDFT)

The covariant density functional theory is a modified version of the relativistic mean field theory (RMF) first introduced by Walecka [Wal74]. The RMF theory was modified by an additional density dependence for a quantitative description of nuclear surface properties [Lal09].

The CDFT starts with a standard Lagrangian density [Gam90]

$$\begin{aligned}\mathfrak{L} &= \bar{\psi}\left(\gamma(i\partial - g_\omega\omega - g_\rho\vec{\rho}\vec{\tau} - eA) - m - g_\sigma\sigma\right)\psi \\ &+ \frac{1}{2}(\partial\sigma)^2 - U(\sigma) - \frac{1}{4}\Omega^{\mu\nu}_{\mu\upsilon} + \frac{1}{2}m^2_\omega\omega^2 \\ &- \frac{1}{4}\vec{R}_{\mu\nu}\vec{R}^{\mu\nu} + \frac{1}{2}m^2_\rho\vec{\rho}^2 - \frac{1}{4}F_{\mu\upsilon}F^{\mu\nu},\end{aligned} \tag{2.26}$$

which contains nucleons ψ with mass m and mesons σ, ω, ρ. Other parameters in the Lagrangian are the electromagnetic field A, the nonlinear potential U. The quantities g_σ, g_ω and g_ρ are the coupling constants while $\Omega_{\mu\upsilon}$, $F_{\mu\upsilon}$ and $R_{\mu\upsilon}$ are the field tensors. The nonlinear potential is defined in terms of the non-linear meson coupling as

$$U(\sigma) = \frac{1}{2}m^2_\sigma\sigma^2 + \frac{1}{3}g_2\sigma^3 + \frac{1}{4}g_3\sigma^4, \tag{2.27}$$

is responsible for the additional density dependence. To describe the ground state and rotational properties of finite nuclei along the valley of stability the parameter set NL3 was introduced [Lal97]. Detailed formalism of the Lagrangian is presented in [Sul03].

2.3 Electromagnetic transitions

An excited nucleus usually dissipates excess energy as it decays to the ground state by the emission of electromagnetic radiation. The properties of these radiation fields, if known, are excellent probes to examine the features of nuclear structure [Gol55]. In this section, types of electromagnetic transitions namely, gamma decay, internal conversion and internal pair formation are discussed.

2.3.1 Gamma-ray transitions

One of the modes of decay of an excited state is by emission of gamma rays, a process where the excess energy is transformed into electromagnetic energy and is carried away by a photon. During this process, the nuclear constituents (protons and neutrons) remain unchanged. The decay from an initial state with energy E_i, orbital angular momentum l_i with a projection of the magnetic momentum m_i and wave function Ψ_i to a final state having the following properties E_f, l_f, m_f and Ψ_f, will emit a gamma ray with energy E_γ. The emitted gamma rays must carry at least one unit of angular momentum. By measuring the properties of emitted gamma ray, the properties of the initial state can be inferred.

Transitions that generate gamma rays are governed by operators which depend on the nuclear multipole moments. It should be noted that the movement of nucleons in the nucleus create definite electric and magnetic fields which are described by multipole moments. The multipole moment can be static or dynamic. The static nuclear moments are closely associated with the electric and magnetic fields of a specific nuclear state [Gol55]. On the other hand, the dynamic nuclear moment describes the change in the magnetic and electric fields of a nucleus due to transitions from excited state to a lower energy excited state.

The dynamic multipole moment expectation value M_{if} (matrix element) for transition between nuclear states with different wave functions (i.e $\Psi_i \neq \Psi_f$) is defined by

$$M_{if} = \int \Psi_f^* \hat{O}_{\sigma\lambda} \Psi_i d\tau, \tag{2.28}$$

where Ψ_i and Ψ_f are the initial and final wave functions of the nuclear states, $\hat{O}_{\sigma\lambda}$ is the operator of the corresponding multipole moment. The index, σ represents the electric or magnetic moment of multipole order λ. The expectation value of the static multipole moment is determined when the initial and final states are the same ($\Psi_i = \Psi_f$) as

$$M_{if} = \int_{-\infty}^{+\infty} \Psi_i^* \hat{O}_{\sigma\lambda} \Psi_i d\tau = \int_{-\infty}^{o} \Psi_i^* \hat{O}_{\sigma\lambda} \Psi_i d\tau + \int_{0}^{+\infty} \Psi_i^* \hat{O}_{\sigma\lambda} \Psi_i d\tau. \tag{2.29}$$

2.3.1.1 Electric and magnetic moments

The distributions of charges and currents inside the nucleus are described by multipole moments. The charges and currents create electromagnetic fields with definite shapes and properties, in that if a proton occupies the $l = 0$ state, and in consequence has a spherical spatial distribution Y_{00}, it will also have a spherical electric field. Furthermore, if the protons are in an $l = 1$ state, its electric field will be asymmetric, hence, the shape of electric and magnetic fields is built upon the angular momentum l. The angular momentum l is also called the multipole order, and is characterized by the spherical harmonics Y_{lm}.

The field with angular momentum $l = 0$ has multipole order 0, thus called monopole field; for $l = 1$ field, the multipole order is unity and is called a *dipole*; while for $l = 2$, the multiple order will be 2, thus referred to as *quadrupole*, etc. The multipole moment M_l of a field of multipole order l carries information

about the angular dependence of the field and transition probability.

2.3.2 Internal conversion

Internal conversion (IC) is a radioactive decay process whereby an orbital electron interacts with the electromagnetic field of the nucleus such that the transition energy is carried away by the orbital electron leading to the ejection of the electron from the atom [Kan95]. The kinetic energy of the ejected electrons K_e can be expressed as

$$K_e = E_\gamma - BE, \tag{2.30}$$

where BE is the binding energy of the electron which depends on the shell occupied by the electron before the process occurs. Thus, the kinetic energy of the electron will be different depending on the initial shell of the electron. In this way, the electron can come from any of the K, L, M, etc..., shells [Mon14]. It is worth noting that this is not a two-step process whereby a gamma ray is emitted and afterwards interact with an orbital electron to eject it out of its orbit; it is highly unlikely that such a process would occur [Kra88, Mon14].

Internal conversion process competes with gamma-ray emission below an excitation energy equivalent to $2m_ec^2$, where m_e is the electron rest mass and c ia the speed of light. However, above $2m_ec^2$, pair formation becomes possible. The ratio of decay due to internal conversion to gamma-ray emission is given by the Internal Conversion Coefficient (ICC). The ICC depends on the transition energy, atomic number and multipolarity of the transition. A detailed discussion of internal conversion coeffcients is given in the next subsection.

2.3.2.1 Internal conversion coefficient (ICC)

The probability of ICE being emitted over gamma ray is determined by the ICC (α) parameterized as

$$\alpha_{tot} = \frac{I_e}{I_\gamma} = \alpha_K + \alpha_L + ..., \tag{2.31}$$

where α_{tot} is the sum of the various ICCs, I_e is the intensity of the conversion electrons emitted from one of the shells and I_γ is the gamma-ray intensity [Kan95]. The theoretical ICCs for electric and magnetic multipole can be calculated using a non-relativistic approach as follows [Ber07]

$$\alpha(EL) \cong \frac{Z^3}{n^3}\left(\frac{L}{L+1}\right)\left(\frac{e^2}{\hbar c}\right)^4\left(\frac{2m_0c^2}{E}\right)^{L+5/2}, \tag{2.32}$$

$$\alpha(ML) \cong \frac{Z^3}{n^3}\left(\frac{e^2}{\hbar c}\right)^4\left(\frac{2m_0c^2}{E}\right)^{L+3/2}, \tag{2.33}$$

where $\frac{e^2}{\hbar c}$ is the fine structure term, $\hbar$ is the reduced Planck's constant, Z and e are the atomic number and the electron charge, respectively. Salient features of the conversion coefficient are revealed by Eqns. (2.32 & 2.34), firstly the Z^3 shows that the process is more likely for heavy nuclei. Secondly, the dependence on n the main quantum number is an indication that conversion electrons are preferentially emitted from the most interior shells. The last factor demonstrates that internal conversion increases inversely with transition energy [Bob07]. For a mixed transition, the ICC is

$$\alpha = \frac{\alpha_{ML} + \delta \times \alpha_{E(L+1)}}{1+\delta^2}, \tag{2.34}$$

where δ^2 is a mixing ratio. When the experimental ICC (α_{exp}) is used, the mixing

ratio is calculated as [Ros49, Kan95]

$$\delta^2 = \frac{\alpha_{ML} - \alpha_{exp}}{\alpha_{exp} - \alpha_{E(L+1)}}. \tag{2.35}$$

2.3.3 Internal pair formation (IPF)

Internal pair formation is an alternative mode of decay that can compete with gamma decay and internal conversion at transition energies above $2m_0c^2$. The emission of electron-positron pair is highest when the internal conversion is smallest, this is seen at energies well beyond 1.022 MeV. The probability of electron-positron pair formation increases at higher energies contrary to internal conversion process.

For higher order electromagnetic multipolarities, the electron-positron pair conversion probability is defined in terms of gamma-ray emission probability and the pair conversion coeffcient of the transition. Similarly, for electric multipoles, the double differential pair emission probability as derived in [Ros49] is

$$\begin{aligned}
&\frac{d^2\alpha_\pi\,(EL)}{dE_+ dcos\theta_{sep}} = (2\alpha/\pi(L+1))(p_+p_-/q)\frac{(q/k)^{2L-1}}{(k^2-q^2)^2} \\
&\times [(2L+1)(W_+W_- + 1 - \frac{1}{3}p_+p_-cos\theta_{sep}) \\
&+ L[(q^2/k^2) - 2](W_+W_- - 1 + p_+p_-cos\theta_{sep}) \\
&+ \frac{1}{3}(L-1)p_+p_- - [(3/q^2)(p_-p_+cos\theta_{sep}) \times (p_+ + p_-cos\theta_{sep}) - cos\theta_{sep}]],
\end{aligned} \tag{2.36}$$

while that of the magnetic multipoles is expressed as

$$\begin{aligned}
&\frac{d^2\alpha_\pi\,(EL)}{dE_+ dcos\theta_{sep}} = (2\alpha/\pi)(p_+p_-/q)\frac{(q/k)^{2L+1}}{(k^2-q^2)^2} \\
&\left\{1 + W_+W_- - \frac{p_+p_-}{q^2(p_- + p_+cos\theta_{sep})(p_+ + p_-cos\theta_{sep})}\right\},
\end{aligned} \tag{2.37}$$

where α is the fine structure constant, p is the momentum, q is the magnitude of quantization, $W = E + \gamma$ is the energy of the outgoing electron, θ_{sep} is the separation angle and k is the transition energy. A detailed derivation of angular and energy distribution for electric and magnetic multipoles is given in [Ros49].

The double-differential emission probability is calculated theoretically within the Born approximation where the e^- and e^+ are regarded as plane waves [Lei98]. The double-differential probability depends on the transition energy, multipolarity, separation angle and the atomic number Z. In [Ald56], the First Born Approximation is defined by

$$f(\theta, \varphi) = \frac{-m}{2\pi\hbar^2} \int d^3r' e^{-ik.r'} V(r') e^{iq.r'/\hbar}, \tag{2.38}$$

where θ and φ are the polar and azimuthal angles of the pairs.

2.3.4 Parity and selection rules

Gamma radiation is, as already alluded to, electromagnetic radiation emitted by the nucleus. Whether the emitted radiation is of the electric or magnetic type is determined by the relative parity of the initial and final levels. The spin and parity of the initial and final state in the de-excitation process and the photon angular momentum are represented by J_i, J_f, π_i, π_f and L respectively. Since the J_i, L and J_f must form a closed vector triangle, the allowed values of L are definite with the largest and least value being $|J_i + J_f|$ and $|J_i + J_f|$ respectively [Kra88]. Hence, the angular momentum conservation law stipulates that

$$|J_i - J_f| \leq L \leq J_i + J_f, \tag{2.39}$$

For a given nuclear state, there is a specific parity, either $\pi = +1$ or $\pi = -1$. The parity operator tests the wave function of a nuclear state for a change in its sign under a reflection in space. The electric and magnetic moment operators have opposite parities calculated respectively as

$$\pi(\hat{O}_{E\lambda}) = (-1)^{\lambda+1}, \tag{2.40}$$

$$\pi(\hat{O}_{M\lambda}) = (-1)^{\lambda}. \tag{2.41}$$

Similarly, the parity of a transition with electric or magnetic nature can be determined respectively by,

$$\pi(EL) = (-1)^{L}, \tag{2.42}$$

$$\pi(ML) = (-1)^{L+1}. \tag{2.43}$$

This implies that electric and magnetic multipoles of the same order will both have opposite parity.

2.3.5 Reduced transition probability

The reduced transition probability is a useful tool in comparing two different transitions of the same multipole order. It is also used to obtain information about the underlying nuclear structures. For example, high reduced transition probabilities correspond to collective excitations and deformed nuclear shapes. The reduced transition probability $B(\sigma L)$ in terms of the squared matrix element of the multipole operator for electric (EL) or magnetic (ML) transitions [Won04] can be expressed as

$$B(\sigma L) = \sum_{mM_f} |\left\langle I_f M_f | \hat{O}_{Lm} | I_i M_i \right\rangle|^2, \tag{2.44}$$

where σ represent either magnetic or electric transitions, the parameters m and M_f describes the orientation of the final spin states and $\hat{O}_{Lm}$ is the multipole operator. The $B(\sigma L)$ values are specified in Weisskopf units (W.u.), which are based on single particle estimates of the transition [Bla52].

The operator for electric and magnetic transitions is given respectively by

$$\hat{O}_{lm}(EL) = \sum_{i=1}^{A} e_i r_i^L Y_{lm}^*(\theta_i, \phi_i), \tag{2.45}$$

$$\hat{O}_{lm}(ML) = \sum_{i=1}^{A} g_s(i) s_i + g_l(i) \frac{2l_i}{L+1} . \bigtriangledown_i \left(r_i^L Y_{lm}^*(\theta_i, \phi_i)\right), \tag{2.46}$$

where e_i is the electric charge with values of $1e$ for protons and 0 for neutrons, l_i and s_i are the orbital and spin angular momenta of the nucleon, while $g_l(i)$ and $g_s(i)$ are gyromagnetic ratios representing the spin and orbital factors, respectively.

2.4 Electric monopole (*E0*) transitions

Due to conservation of angular momentum, single gamma decay is forbidden in a transition between a pair of 0^+ or 0^- states with no parity change. The only alternative mode of decay is by $E0$ transition which takes place either by the emission of ICE or IPF depending on the transition energy. Electric monopole transitions occur purely by the penetration of the orbital electrons within the finite nuclear volume [Chu58]. Monopole transitions can also occur between states with same spin and parity ($J^\pi \rightarrow J^\pi$), in such a transition, the $E0$ component may compete with gamma-ray emission and internal conversion of transitions of higher multipole order [Chu56, Kan95]. For example a $2^+ \rightarrow 2^+$ or $4^+ \rightarrow 4^+$ may have an $E0$ component competing with an $E2$ transition, as a result the $E0$ is usually very weak. A typical example of pure $E0$ transition and mixed multipolarity is illustrated in the partial decay scheme of ^{54}Cr presented in Fig. 2.2.

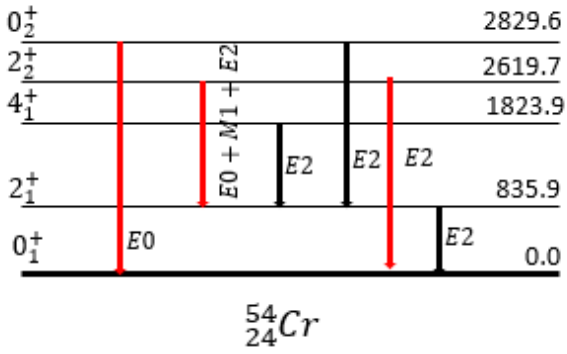

Figure 2.2: Partial level scheme of ^{54}Cr illustrating the occurrence of pure $E0$ transition and mixed multipoles. The highlighted states are transitions of interest in this study. Data are taken from the Evaluated Nuclear Structure Data Files (ENSDF) [Don14].

The electric monopole moment is simply the magnitude of the electric charge q,

$\mathbf{M_0} = q$. Hence, for an $E0$ transition to happen, an orbital electron must dive into the centre of the nucleus and during that experience a change in electric field [Kan95]. The ejected electron may as well carry away energy from the nucleus. The monopole strength operator is related to nuclear radius R, change of its mean-square charge radius, and radial density oscillations, etc. The $E0$ matrix element has the form

$$\rho(E0) = \frac{\langle f|\mathbf{M}(E0)|\, i\rangle}{eR^2}, \tag{2.47}$$

where e is the electronic charge. The reduced monopole transition probability $B(E0)$ is equal to the square of the monopole strength matrix element

$$B(E0) = \rho^2(E0)e^2R^4. \tag{2.48}$$

The $E0$ strength operator can also be rendered as

$$M(E0) = e\sum_p r_p^2. \tag{2.49}$$

The sum is taken over square of the radius vector of the protons. To showcase the very important quantities used in the description of the $E0$ transition rates, the $E0$ transition is defined in terms of the electronic factor and the square of the matrix element, ρ^2 as

$$W(i; E0) = \frac{1}{\tau(E0)} = \rho^2\Omega_i(Z, k), \tag{2.50}$$

where $i = K, L$,..., or IPF, τ is the partial lifetime, Z and k represents the atomic number and transition energy, respectively. The electronic factor Ω defined by Church and Weneser [Chu56] has the units of s^{-1}. It is a non-nuclear

quantity corresponding to the internal conversion coefficient and it varies with the transition energy, atomic number Z of the nucleus and electron shell involved but independent of spin of the states involved [Chu56, Kan95, Woo99, Kib08]. It is assumed that all nuclear structure information is embodied in the dimensionless monopole strength parameter $\rho^2(E0)$ since the matrix elements are highly sensitive to the finer details of the nuclear wave function [Chu56]

The total $E0$ transition probability is given by the expression

$$W\left(E0\right) = \frac{1}{\tau\left(E0\right)} = W_{ic}\left(E0\right) + W_{\pi}\left(E0\right), \tag{2.51}$$

where $W_{ic}(E0)$ and $W_{\pi}(E0)$ are the transition probabilities for ICE and IPF respectively. The two quantities are defined by

$$W_{ic}\left(E0\right) + W_{\pi}\left(E0\right) = \rho^2\left(E0\right) \times \left[\Omega_{ic}\left(E0\right) + \Omega_{\pi}\left(E0\right)\right], \tag{2.52}$$

where $\Omega_{ic}(E0)$ and $\Omega_{\pi}(E0)$ are electronic factors for ICE and IPF respectively. Electrons from the K shell are most likely to be emitted due to its greater spatial overlap of the electron and nuclear wave functions [Reg03]. Therefore, only the K shell gives a tangible contribution to $E0$ transitions [Kan95, Ber07]; hence, the strength parameter takes the form

$$\rho^2\left(E0\right) = \frac{1}{\Omega_K(E0) \times \tau_K(E0)}. \tag{2.53}$$

where $\tau(E0)$ is the partial mean lietime of the $E0$ transition. The determination of $\rho^2(E0)$ requires knowledge of the half-life of 0^+ states and branching ratio for $E0$ decay. Though, this is not usually practical as the half-lives of many 0^+

states are still not known. An alternative method involving the use of a quantity $X(E0/E2)$ defined as the ratio of $E0$ and $E2$ reduced transition probabilities can be utilized [Ras60] in such circumstances. The quantity is defined by

$$X(E0/E2) = \frac{B(E0)}{B(E2)} = \frac{\rho^2(E0)e^2R^4}{B(E2)}. \tag{2.54}$$

For $J^\pi \rightarrow J^\pi$ transitions (e.g., $2^+ \rightarrow 2^+$), the $\rho^2(E0)$ of the $E0$ component can be determined using the quantity $q_K^2\left((E0/E2)\right)$ introduced by [Chu56], which is expressed as the ratio of the monopole transition ($E0$) and quadrupole transition ($E2$) K conversion electron intensities

$$q_K^2(E0/E2) = \frac{I_K(E0)}{I_K(E2)}. \tag{2.55}$$

Provided the $E2$ transition rate is known, the $\rho^2(E0)$ value can be deduced using

$$\rho^2\left(E0\right) = q_K^2\left((E0/E2)\right) \times \frac{\alpha_{K(E2)}}{\Omega_K\left(E0\right)} \times W_\gamma\left(E2\right), \tag{2.56}$$

where $\alpha_K(E2)$ is the K conversion coefficient for a pure $E2$ transition. The quantity $q_K^2(E0/E2)$ can be extended to transitions with zero spin and parity ($0^+ \rightarrow 0^+$) where $E2$ transition is forbidden [Kib94]. Therefore, the corresponding experimental value of the intensity ratios can be obtained from

$$X(E0/E2) = 2.54 \times 10^9 A^{4/3} \times q_K^2(E0/E2) \times \frac{\alpha_K(E2)}{\Omega_K(E0)} \times E_\gamma^5, \tag{2.57}$$

where E_γ is energy of the $E2$ transition.

2.4.1 Model prediction of $E0$ transitions

The nuclear structure information carried by the ρ^2 values can be directly related to simple models such as shell model and collective model [Woo99]. Shell model estimates of $\rho^2(E0)$ can be directly formulated because the shell model describes the nucleus in terms of nucleon degrees of freedom [Woo99].

A $\rho^2(E0)$ value of two-proton configurations with single-particle orbits j_1 and j_2 can be obtained directly by assuming the two states are mixed thus

$$\begin{aligned} |0_i^+\rangle &= a(j_i^2)_0 + b(j_2^2)_0 \\ |0_f^+\rangle &= -b(j_1^2) + a(j_2^2)_0, \end{aligned} \tag{2.58}$$

where $(j_i^2)_0$ and $(j_1^2)_0$ indicate pairs of nucleons coupled to total spin zero, and with the normalization $a^2+b^2=1$, the ρ^2 value between two oscillator shells takes the form

$$\rho^2 = \frac{2ab}{R^2}\left(\langle r^2\rangle_f - \langle r^2\rangle_i\right), \tag{2.59}$$

where $\langle r^2\rangle$ is the proton mean square radii. If j_1 and j_2 are members of adjacent oscillator shells, then ρ^2 for maximum mixing is [Kan95, Woo99]

$$\rho^2 = 0.5A^{-2/3}, \tag{2.60}$$

where A is the mass number of the nucleus in question. The spherical quadrupole phonon model predicts the quantities $X(E0/E2)$ and ρ^2 to be

$$\rho^2 \approx 0.023Z^2\beta_{rms}^4, \tag{2.61}$$

$$X(E0/E2) = \beta_{rms}^2, \tag{2.62}$$

where "rms" signifies a dynamic deformation.

In a case where two 0^+ states both containing two components of different shapes (e.g. spherical and deformed) are assumed to be mixed, it is easy to write the formula that depicts the role of deformation and mixing. The two levels (e.g., 0_f^+ and 0_i^+) are inferred to have the following wave functions [Kan95],

$$\begin{aligned} \left|0_i^+\right\rangle &= a\left|sph\right\rangle + b\left|def\right\rangle \\ \left|0_f^+\right\rangle &= -b\left|sph\right\rangle + a\left|def\right\rangle, \end{aligned} \tag{2.63}$$

where a and b are the mixing amplitudes. Here the deformed component gives the major contribution to the $E0$ transition intensity. Hence, the monopole operator can be written as follows

$$\left\langle 0_i^+ \left|\mathbf{M}\left(E0\right)\right| 0_f^+ \right\rangle \approx abk\beta_2^2, \tag{2.64}$$

where β_2^2 is the quadrupole deformation parameter and k can be deduced from

$$k = \frac{3}{4\pi} ZeR^2 \left[1 + \frac{4\pi^2}{3}\left(\frac{a_0}{R}\right)^2\right], \tag{2.65}$$

where a_0 is the diffusness parameter of the nuclear surface.

2.4.2 Shape coexistence

Nuclei located half-way between shell closures exhibit most significant form of deformation due to the number of valence nucleons [Eji89]. On the contrary, nuclei near the closed shell have only few active valence nucleons, hence spherical shapes are the most dominant feature in this region. Nonetheless, the existence

of multiple shapes with different deformation in one nucleus is probable. This phenomenon is called shape coexistence [Eji89, Yan96]. It has been reported in Ejiri and de Voigt [Eji89] that where spherical and deformed shapes coexist, states due to single-particle excitations and rotational band heads appear at nearly the same excitation energy. The coexistence of different shapes in one nucleus creates scenarios where unified models that could interpret both types of structure can be tested. As reported in [Hey83, Woo92] it is customary to base the evidence of shape coexistence on band structures, especially energy spacing and electromagnetic transition probabilities. The phenomenon of shape coexistence has been established in doubly magic nuclei like ^{16}O and ^{40}Ca where there is a promotion of nucleon pairs across the shell gap Wood *etal*., [Woo92]. Spectroscopic evidence in support of shape coexistence in ^{16}O and ^{40}Ca are the existence of a $K^{\pi} = 0^{+}$ at excitation energies of 6049 keV and 3353 keV due to $4p-4h$ excitations in ^{16}O and ^{40}Ca respectively [Woo92]. Single closed-shell nuclei, for example, the tin isotopes, also exhibit shape coexistence. This finding is supported with evidence from the relative $B(E2)$ and large $\rho^2(E0)$ values that suggest excited deformed bands in the low-lying states and strong mixing between near spherical and deformed intruder excitation [Woo92, Woo99]. The Cd isotopes are nuclei near closed shells which also display strong $\rho^2(E0)$ and $B(E2)$ values which underpin the identification of deformed bands in these nuclei. The $\rho^2(E0)$ and $B(E2)$ values are shown in Figs. (23 & 24) of Ref. [Woo99].

2.4.2.1 Link between $E0$ transitions and shape coexistence

The relationship between shape mixing and monopole $E0$ strength is demonstrated in a two-level model [Hey90, Woo99]. The mixing between the two phonon

state (0_2^+) with the ground state (0_1^+) results in two eigenstates $\left|0_i^+\right\rangle$ and $\left|0_f^+\right\rangle$

$$\begin{aligned}\left|0_i^+\right\rangle &= a\left|0_1^+\right\rangle + b\left|0_2^+\right\rangle \\ \left|0_f^+\right\rangle &= -b\left|0_1^+\right\rangle + a\left|0_2^+\right\rangle,\end{aligned} \tag{2.66}$$

The $E0$ operator and the matrix element $\rho_{fi}(E0)$ is related by the expression

$$\rho_{fi}(E0) = \frac{1}{eR^2}\left[ab\left(\left\langle 0_1^+|\boldsymbol{M}(E0)|0_1^+\right\rangle - \left\langle 0_2^+|\boldsymbol{M}(E0)|0_2^+\right\rangle\right) + (a^2-b^2)\left\langle 0_2^+|\boldsymbol{M}(E0)|0_1^+\right\rangle\right] \tag{2.67}$$

For weak mixing, the mixing amplitudes a and b are approximately zero [Woo99], thus;

$$\left\langle 0_i^+\left|\boldsymbol{M}\left(E0\right)\right|0_f^+\right\rangle \approx 0, \tag{2.68}$$

However, for a strong mixing scenario, the monopole operator is still zero, but $a\sim -b \approx \frac{1}{\sqrt{2}}$, hence, the $E0$ strength parameter is related to the difference in deformation of the states

$$\rho^2\left(E0\right) = \frac{1}{4}\left(\frac{3}{4\pi}\right)^2 Z^2\left(\beta_1^2 - \beta_2^2\right)^2. \tag{2.69}$$

2.5 Nuclear reactions

If a charged particle is accelerated with a sufficient kinetic energy and incident on a stationary target, there is the possibility of a nuclear reaction taking place. During the nuclear reaction process, the accelerated particle (beam) can produce different types of reaction depending on its energy. A typical nuclear reaction is shown in Fig. 2.3. Nuclear reactions broadly are grouped into compound or direct reactions. The probability of either occurring depends on the distance of

approach and the energy of the projectile. The two reactions shall be discussed in this section.

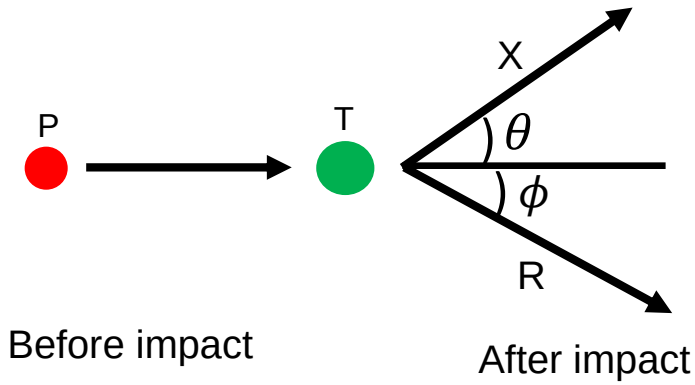

Figure 2.3: An illustration of nuclear reaction mechanism. P is the beam, T is the target, X is the outgoing particle and R is the recoil.

2.5.1 Compound reaction

When a projectile with kinetic energy in the range of 10-20 MeV enters a target nucleus with an impact parameter small compared to the nuclear radius, it will interacts many times inside the nucleus, boosting individual nucleons into excited states, until it comes to rest inside the nucleus. The decay of the compound nucleus may yield a process whereby nucleons are given sufficient energy to escape. A notation of a compound reaction is $a + X \rightarrow Y^*_{t_{1/2>>10^{-23}s}} \rightarrow B + b$, the compound nucleus Y is written with asterisk to show it is in excited state and it must live longer than the transit time a nucleon will take to traverse the nuclear diameter [Won04]. Thus, the time scale of a compound reaction is in the range of 10^{-19} - 10^{-15} seconds [Ber07]. An example of a compound reaction is that of $^{70}\mathrm{Ge}(\alpha, np\gamma)^{72}\mathrm{As}$, whereby, a proton beam interacts with a ^{70}Ge target and produces ^{72}As after emission of EM radiation.

2.5.2 Direct reaction

Direct reactions are referred to as peripheral reactions involving only a few surface nucleons. These reactions occur within a time scale of the order of 10^{-22} seconds and can be grouped into scattering and breakup reactions [Ber07].

Pickup reaction: If the incident particle is identical with the outgoing particle and the recoil nucleus is also identical with the target (or the target remains unchanged and in ground state) it is elastic scattering reaction, for example ^{70}Ge$(\alpha, \alpha^{'})^{70}$Ge. On the other hand if the recoil nucleus remains in its excited state, it is an inelastic scattering reaction, the example of the $(\alpha, \alpha^{'})$ reaction given in Section (4.1) is a typical case.

Stripping reaction: In this type of reaction, one or more particles are emitted from the target nucleus. The most encountered stripping reaction are the "deuterium stripping" reaction, (d, p) or (d, n) and "α stripping" reactions, (α, p) or (α, n). Stripping reactions are important in the study of low-lying shell-model excited states [Kra88].

2.5.3 Coulomb barrier and Coulomb excitation

As the projectile with charge Z_1 and mass A_1 approaches the target nucleus with a charge Z_2 and mass A_2, there is a repulsive force (Coulomb force). For the two charged nuclei to interact and be in the range of the nuclear force between their nucleons, the projectile must approach the target with a kinetic energy equal or greater than the repulsive Coulomb barrier between them. Note that their centres are separated by the sum of their radii $R_1 + R_2$ respectively. Consequently, the

barrier is given by

$$V_c = \frac{1.44 Z_1 Z_2}{R_1 + R_2} = \frac{1.44 Z_1 Z_2}{R_0 (A_1^{1/3} + A_2^{1/3})}. \tag{2.70}$$

For example, the Coulomb barrier for bombarding a $^{70}_{32}$Ge nucleus with alpha an particle, $^{4}_{2}$He and that of $^{54}_{24}$Cr with a proton is calculated using Kantele calculator [Tar02] with a density factor of ~ 1. The results yield 11.2 MeV and 5.02 MeV, respectively.

In a fusion reaction where a compound nucleus is formed, for linear momentum and kinetic energy to be conserved, the kinetic energy of the projectile K_1 must exceed the Coulomb barrier threshold kinetic energy K_{ct} [Won04]. The K_{ct} expressed as [Won04]

$$K_{ct} = V_c (1 + \frac{A_1}{A_2}). \tag{2.71}$$

2.5.4 Reaction kinematics

When a beam is incident on a target, there are multiple collisions of beam particles with different nuclei in the centre of mass frame (cm). At the centre of mass frame, the projectile and target nucleus momenta are equal and opposite. The kinetic energy, E_{cm} of the collision transferred to the compound system can be calculated by taking the difference between the kinetic energy of the beam, E_B and the kinetic energy of the recoiling compound system, E_R. Thus,

$$E_{cm} = E_B - E_R. \tag{2.72}$$

If the momentum of the beam in the laboratory frame is ${p_i}^{lab}$ and that of the target is ${p_t}^{lab}$, where ${p_t}^{lab} = 0$; for a compound nucleus frame of reference, the beam and recoil momenta would be zero as the particles fused together. By

Lorentz transformation the beam energy (e.g., α in the case of this study) and momentum in the cm and lab. frames could be defined as

$$E_{\alpha}^{cm} = \gamma_{cm}(E_{\alpha}^{lab} - \beta_{cm}p_{\alpha}^{lab}c), E_{\alpha}^{lab} = \gamma_{cm}(E_{\alpha}^{cm} - \beta_{cm}p_{\alpha}^{cm}c), \tag{2.73}$$

and

$$p_{\alpha}^{cm} = \gamma_{cm}(p_{\alpha}^{lab} - \beta_{cm}p_{\alpha}^{lab}/c), p_{\alpha}^{lab} = \gamma_{cm}(p_{\alpha}^{cm} - \beta_{cm}p_{\alpha}^{cm}/c), \tag{2.74}$$

where γ_{cm} is the Lorentz factor in the cm frame $\equiv 1/\sqrt{1-\beta_{cm}^2}$. In the Lab. frame, the initial energies and momenta of the projectile and target before collision are expressed by the following

$$\begin{aligned} E_{\alpha}^{lab} &= E_{\alpha}^{coll} + m_{\alpha}c^2, \\ E_{t}^{lab} &= m_{t}^{*}c^2 \end{aligned} \tag{2.75}$$

$$\begin{aligned} p_{\alpha}^{lab} &= \sqrt{\frac{\left(E_{\alpha}^{lab}\right)^2 - m_{\alpha}^2c^4}{c}} \\ p_{t}^{lab} &= 0. \end{aligned} \tag{2.76}$$

By substituting Eq. (2.73) into Eq. (2.75) the reduced velocity of the centre of mass frame can be obtained by

$$\beta_{cm} = \frac{p_{\alpha}^{lab}c}{\left(E_{\alpha}^{lab} + E_{t}^{lab}\right)}. \tag{2.77}$$

At a scattering angle θ, the energy of the scattered beam in the lab frame at an angle $\theta^{'}$ will be

$$E_{\alpha}^{lab^{'}} = E_{\alpha}^{lab}[1 + \frac{M_1M_2}{M_1 + M_2}(cos\theta_1^{'} - 1)]. \tag{2.78}$$

2.5.5 Nuclear reaction cross section

The cross section is a measure of the relative probability for the reaction to occur. If the ejectile emitted during a nuclear reaction in a given direction $(\theta, \emptyset)$ with respect to the beam direction is measured with a detector, the detector defines a solid angle $d\Omega$ at the target position [Kra88]. Given the fact that the target has N nuclei per unit area interacting with beam particles traveling with a current of I_a per unit time such that the ejectile is emitted into 4π at a rate R, thus, the reaction cross section is given by

$$\sigma = \frac{R}{I_a N}. \tag{2.79}$$

Defined in this way, σ has the dimension of area per nucleus. The detector occupies a small solid angle $d\Omega$ compared to the 4π emission of the ejectiles. Therefore, only a small fraction of the particles emitted dR is observed, hence, only a fraction of the cross section $d\sigma$ will be deduced [Kra88]. However, since the emission of the ejectiles is not isotropic, it will have an angular distribution that is dependent on θ and $\emptyset$. If the angular distribution function is arbitrary represented by $r(\theta, \emptyset)$, therefore,

$$\frac{d\sigma}{d\Omega} = \frac{r(\theta, \emptyset)}{4\pi I_a N}, \tag{2.80}$$

where $\frac{d\sigma}{d\Omega}$ is the differential cross section and the term 4π is introduced to make $d\sigma/4\pi$ a pure fraction. The reaction cross section σ can be obtained by integrating $\frac{d\sigma}{d\Omega}$ over all angles as

$$\sigma = \int \frac{d\sigma}{d\Omega} d\Omega = \int_0^{\pi} sin\theta d\theta \int_0^{2\pi} d\emptyset \frac{d\sigma}{d\Omega}. \tag{2.81}$$

In a situation where the interest is to find the probability of a particle emitted at a certain angle with an energy corresponding to a specific energy of the reaction product net decay. The definition of cross section will mean the probability to observe an emitted particle b in the angular range of $d\Omega$ and in the energy range dE_b. This probability is called a double differential cross section.

Another type of cross section that is also considered in a nuclear reaction experiment, which is important in this study, is the total cross section. In this type of cross section for a specific beam particle a, the reaction cross section is the sum of all possible different outgoing particles, irrespective of their direction or energy [Kra88]. This gives information on the probability for an incident beam to create a reaction at the interaction point, inside the target.

Chapter 3

Electron Spectrometer

This chapter focusses on the refurbishment and characterization of an electron spectrometer that was previously used in IPN Orsay, France. To gain perspective, a comprehensive survey of other existing electron spectrometers and measurement techniques are presented first. Secondly, a general description of the spectrometer is given followed by measurement and simulation of the lens magnetic field. Mechanical modifications made on the spectrometer to make it suitable for measurement of conversion electrons with minimum background is discussed. Subsequently, calibration results with Figures Of Merit (FOM) of the spectrometer are presented.

3.1 Review of electron spectrometers

The measurement of ICE or IPF for electric monopole $E0$ transitions studies is achieved using electron spectrometers specifically designed to transport electrons or pairs to the detector surface. One of the drawbacks of using an electron spectrometer is the background radiation caused by charged nuclear particles from the

target, delta electrons, bremsstrahlung, and Auger electrons from the target material as well as beam line and Faraday cup. [Kan95]. To reduce the background radiation, the following requirements enumerated in [Kan95,Dio99] are essential in the operation of an in-beam spectrometer. The conditions include ensuring; high acceptance solid angle, high transmission efficiency, large momentum resolution ($\frac{\Delta p}{p}$), possibility of broad-range mode operation, selection of energy (momentum) region of interest, suitability to lifetime measurements in sub-nanosecond, and suitability to IPF measurements.

A brief review of other electron spectrometers used for nuclear structure studies is presented according to their classification which depends on the geometry and the method used in creating the magnetic field.

3.1.1 Lens spectrometer

In the lens spectrometer, electrons are transported using an axial field; they are characterized by a constant momentum resolution ($\frac{\Delta p}{p}$). For a long lens, the average momentum is most often over 25 % of 4π whereas, it is a few percent for a short lens [Luo79].

One of such spectrometers is the Siegbahn-Kleinheinz magnetic lens (SK) at the University of Uppsala, Sweden [Kle64]. The spectrometer used an adjustable Hubbert baffle as shown in Fig. 8 of Ref. [Kle64] to discriminate positrons from electrons, thereby eliminating the background caused by positrons and low energy gamma rays. An optimum transmission of the spectrometer is 2.1 %.

Similarly, at the University of Jyväskylä, two identical lenses of the Kleinheinz type [Luo79] were used. It was made to ensure that the beam enters

the lens axially to hit the target inside the lens. A schematic cross-section of the spectromer is shown in Fig. 1 of Ref. [Luo79]. The emitted charged particles were measured on a Si(Li) detector placed in a region of high magnetic field. Thus, high transmission and large momentum resolution were achieved. Another SK magnetic lens spectrometer like the one used in Uppsala, was developed, and coupled to an array of germanium detectors (EUROGAM) in Orsay, France [Dio99] and with a modification of the annular entrance baffle. The configuration yielded a transmission of 4.11 %.

3.1.2 Solenoid spectrometer

In a solenoid spectrometer, a uniform axial magnetic field is used to transport electrons, operating in the broad-range mode with an associated momentum window corresponding to a certain energy range, electrons are thus focused onto the detector [Kan95]. In addition, a solenoid spectrometer can be operated in lens mode by using a baffle system to select the momentum window and the field swept to cover the whole energy spectrum. An alternative mode by which a solenoid spectrometer can be operated is the recoil shadow mode using a transverse geometry. In the recoil shadow mode, the source is placed behind a physical barrier with the aim of reducing background while transporting delayed electrons.

The Super-e electron spectrometer was developed at the Australian National University, Canberra. The spectrometer uses a superconducting solenoid to transport electrons to a segmented Si(Li) detector, it has a maximum efficiency of $\sim$ 5.9 % at 344 keV [Kib90].

A spectrometer called SACRED, named after its detection system (Solenoid Array for ConveRsion Electron Detection) which uses a multi-detector array in a

collinear geometry to detect cascades of conversion electrons was developed in the United Kingdom and later deployed to Finland [Jon96]. The spectrometer has the capability for detecting weak transitions with relatively high efficiency [But96]. The spectrometer was redesigned in 2004 by Kankaanpää *et al.*, [Kan04] to accommodate the Recoil Ion Transport Unit (RITU) gas-filled recoil separator for in-beam recoil and the Recoil Decay Tagging (RDT) measurements. The aim was to achieve maximum background suppression.

Another example of a solenoid spectrometer is the Silicon And Germanium (SAGE) spectrometer coupled to the JUROGAM II germanium array at the University of Jyväskylä which is used in conjunction with the RITU gas filled recoil separator and Ge-detector array. The spectrometer has a maximum absolute efficiency for single electrons of 6% at 150 keV, [Pak15].

3.1.3 Mini-orange

In this type of spectrometer, the magnetic field is produced either by an iron core or permanent magnet arranged in a toroid. The toroidal magnetic field generated by the system can discriminate positrons from electrons of the same kinetic energy, a requirement necessary to reduce background in electron spectroscopy [Sor16]. They are however, limited by transmission such that the maximum transmission achieved is $\sim$ 20%, this is due to the numerous number of transporting gaps [Kan95].

A multi-electron spectrometer with a magnetic filter of Mini-orange type was developed in Japan Atomic Energy institute by Kidera *et al* [Kid97], the device has a unique capability of sensitivity to angular distribution and the Doppler shift of electrons. Similarly, a Spectrometer for Internal Conversion Electrons

(SPICE) designed to fit into the TIGRESS array [Mou18] has been commissioned for in-beam experiments at TRIUMF. The spectrometer has a maximum efficiency of $\sim 10\%$ at 700 keV and $> 5\%$ at 1 MeV for the medium energy magnetic lens. In the University of Lodz, an electron spectrometer which uses a combination of magnets to generate magnetic field in two different layouts was designed and commissioned. With such a design, it is possible to register electrons on detectors placed at backward angles in a wide energy range and at the same time suppress background [And07]. The configuration shows a maximum efficiency of 0.4 % at 300 keV.

There are other electron spectrometers that transport electrons without the use of a magnetic field, such as SPEDE in University of Jyväskylä, Finland [Pap15]. This is achieved by placing an annular silicon detector close to the target at backward angles because the low intensities of RIBs compared to stable ion beams provide for lower radiation and lower delta electron background at backward angles. This position was chosen to reduce radiation caused by delta electrons originating from primary beam and target interactions, giving an efficiency of 7% between 200 keV and 400 keV which decreases to 3% at 600 keV [Pap15].

The Pentagonal Array for Conversion Electron Spectroscopy (PACES) situated inside the GRIFFIN decay setup at TRIUMF also transport electrons without magnetic field. The spectrometer consist of five Si(Li) detectors used for charged-particle detection.

3.2 Description of the refurbished spectrometer at iThemba LABS

This section describes the mechanical features of the spectrometer previously used at IPN Orsay, France. The spectrometer coils are divided in six individual sections consisting of 12 layers with 20 windings each. Rectangular copper wires of 2 mm (radially) $\times$ 3 mm (axially) were wound on a 270 mm wide brass cylindrical plate which acts as the vacuum vessel [Kle64]. The copper wire has a total resistance of 4.5 Ω and a total inductance of 74 mH, separated by a thin insulating material with six 4.5 mm inner diameter water pipes placed in between the coil sections for cooling purposes. To minimize the effect of stray magnetic field, the coils are inserted in a 20 mm thick steel casing and closed on the rear side with a 30 mm thick door. The door has a 40 mm hole to accommodate the Si(Li) detector. In front (target position), it is closed with a cone-shaped iron yoke with an opening of 46 mm diameter also designed to minimize the effect of stray magnetic field. To cool the coils, chilled water at 20 ^{o}C flowing at 22 L/min is used. A cross-sectional view of a two dimensional drawing of the spectrometer showing the coils, target ladder, the detectors and detector assembly is shown in Fig. 3.1.

One of the challenges of electron spectroscopy is how to suppress the background caused by emitted radiations and scattered beam particles in order to acquire a clean spectrum. To mitigate this problem, a 245 mm by 270 mm baffle system made of 8 blades connected to a cylindrical lead piece was inserted. The lead piece lies on the lens axis when the baffle is inserted in the lens and is designed to reduce the background due to delta electrons, positrons, and gamma rays [And07]. A detailed description of the lens can be found in Ref. [Kle64].

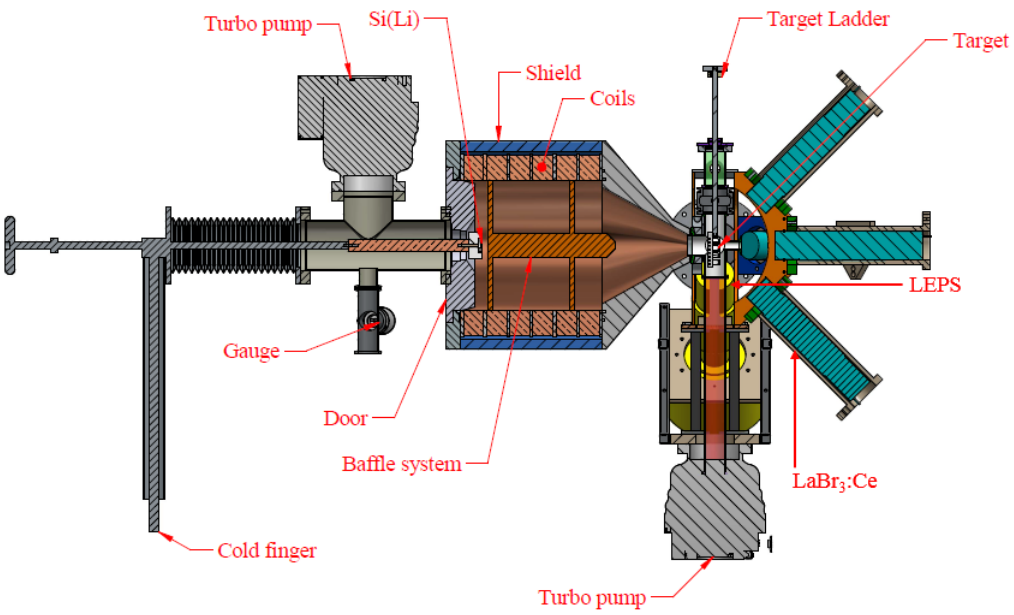

Figure 3.1: Transverse geometry of the magnetic lens showing the physical geometry of the lens and associate component. Courtesy of INIT Department, iThemba LABS. The beam travels into the page.

3.3 Magnetic field profile

In order to revive the spectrometer, for the purpose of measuring ICE, the axial magnetic field was simulated using OPERA 3D simulation software [OPE19]. The calculations were performed using current density defined in vector space as the ratio of the real magnetomotive force (MMF) to the MMF in vector field which is parameterized as

$$J_{vf} = \frac{N_R * I_R}{N_{vf} * A_{vf}}, \tag{3.1}$$

where N_R is the real number of turns (240 turns), I_R is the variable real input current and N_{vf} is the number of turns in vector field which is taken to be unity (1) for one section of six coils. While A_{vf} is the area vector field calculated to

be 1923.04 mm^2 for one set of coils. The axial magnetic field of the lens was calculated in steps of 1 mm beginning from the source position (-50 mm) to a point (100 mm) beyond the detector position for four current settings. Fig. 3.2 presents a brief overview of the meshed model of the spectrometer showing the coil geometry.

A longitudinal hand-held probe model 4048 manufactured by F.W. Bell was used to measure the magnetic field to compare with the simulation result. By supplying DC power via the 5.1 kW power supply (TDK-Lambda, model: GEN150-34-3P400) [TDK], the magnetic field was measured in steps of 50 mm since it was difficult to measure with a hand-held probe in steps of 1 mm, the field profile is shown in Fig. 3.3.

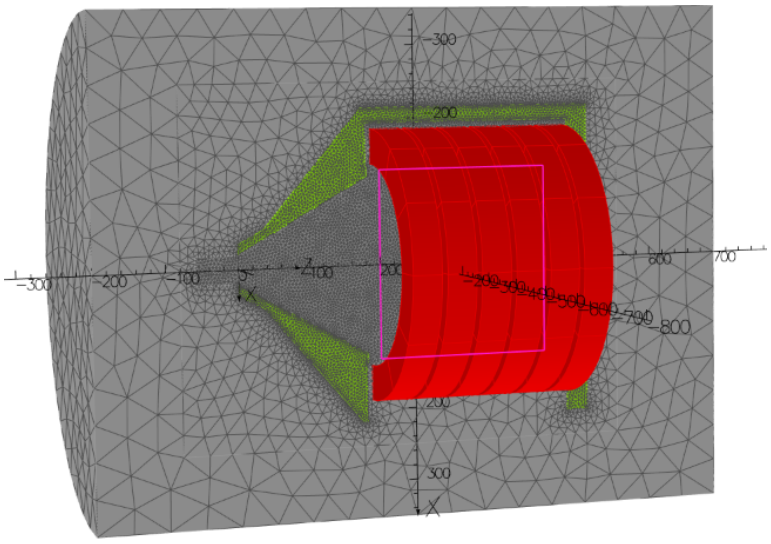

Figure 3.2: Overview of the meshed model of magnetic field in steel obtained from OPERA 3D simulation.

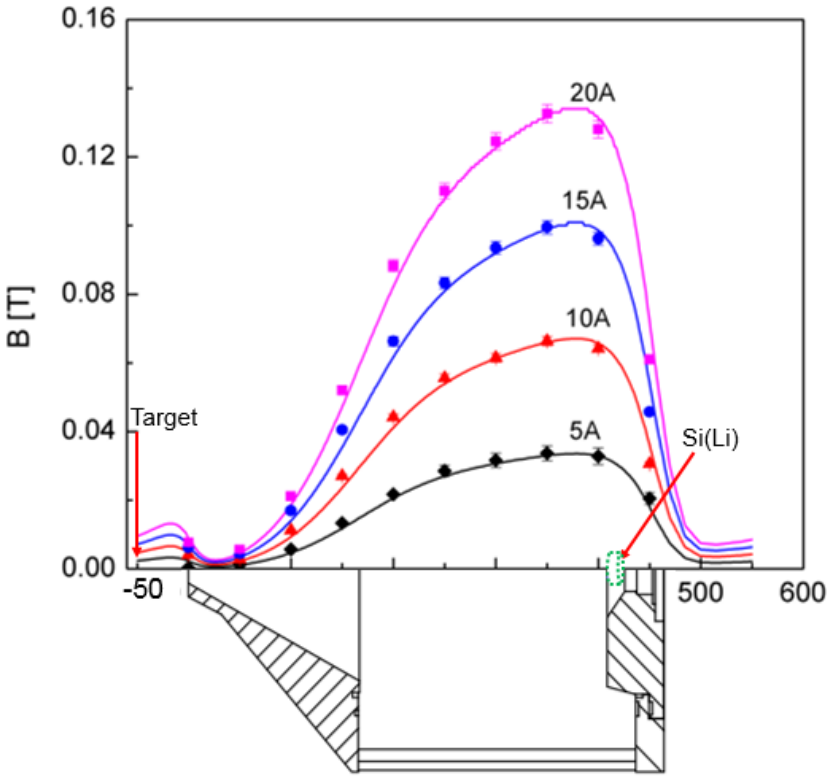

Figure 3.3: Axial magnetic field component for four current settings. The simulation is shown by solid lines and the points represent the measured fields.

It should be noted that there was no prior knowledge about the type of steel the shield was made of, however, the properties of mild steel grade A, were used in the simulations to generate the magnetic field. The 2 % agreement between the measured and simulated field showed the choice of the material properties of the steel was good.

3.4 Spectrometer modification

To make optimum use of the electron spectrometer, some additional instrumentation and modifications were made. In this section, information, and results of the modifications are presented.

3.4.1 Vacuum system

High vacuum is required when using a cooled Si(Li) detector to prevent condensation from forming on the detector surface and to ensure the transport of electrons is not hindered. This was achieved by using two 250 L/s turbo molecular pumps backed by two oil free pumps connected close to the target and detector positions (see Fig. 3.1). It takes about 24 hours to reach minimum pressures of 10^{-6} mbar and 10^{-7} mbar at the target and detector positions, respectively. Dry pumps were used throughout to avoid oil contamination of the system. A schematic of the pumping scheme is shown in Fig. 3.4 while the detailed pumping procedure is described in Appendix A.

3.4.2 Target and detector support system

A support mechanism was manufactured to hold six $LaBr_3$:Ce and two LEPS detectors, both placed at 45° and 35° with respect to the beam line. These detectors are facing directly at the target as shown in Fig. 3.1. To keep the spectrometer under vacuum while changing or mounting targets, a mechanically controlled target ladder was used. The spectrometer and its detector support structure is placed on a movable system, that allows them to be easily coupled to any of the iThemba LABS facilities in the future, for instance, AFRODITE [New98] and

K600 spectrometer [Nev11]. The target system and target ladder showing the target position is shown in Fig. 3.5.

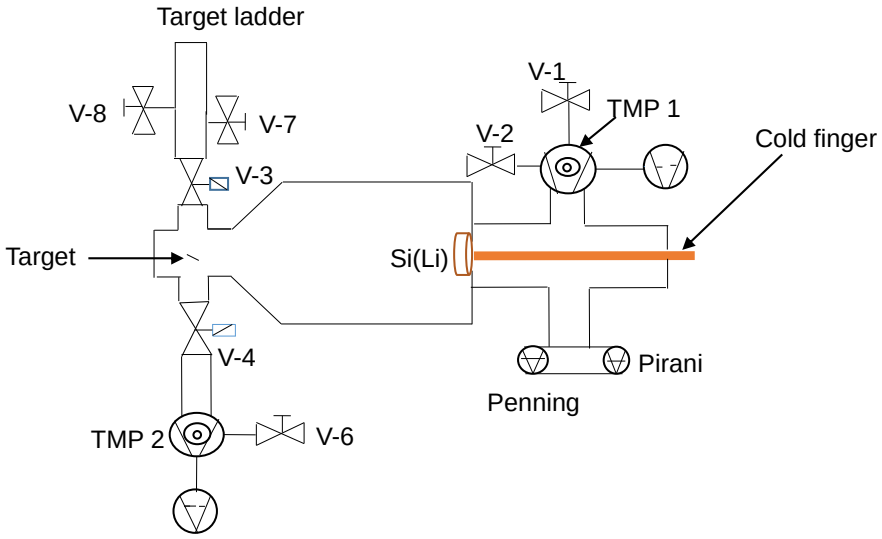

Figure 3.4: The vacuum scheme of the spectrometer showing the gate valves, target position and detector position. TMP1 and TMP2 represent the turbo molecular pump 1 and 2 respectively, while V-1:V-8 represent valves 1 - 8.

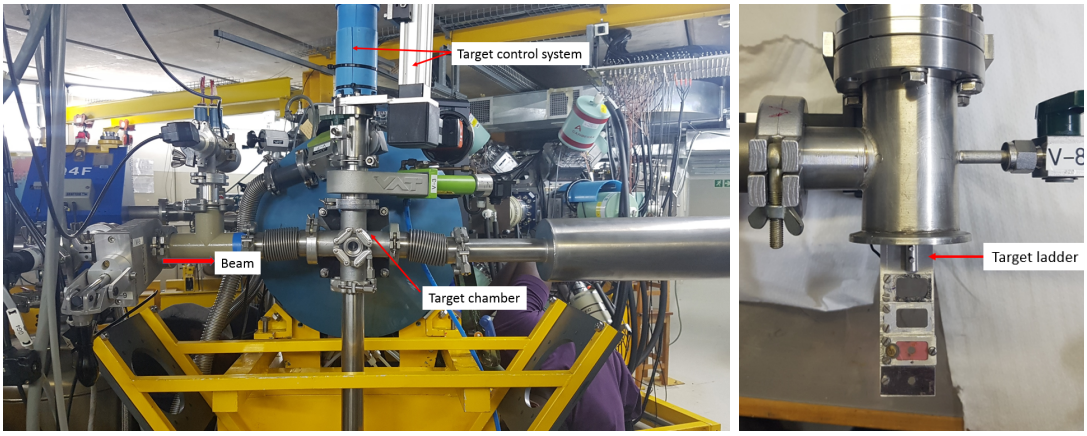

Figure 3.5: Target system showing control system, beam direction, target chamber (left) and the 4 target positions (right).

3.4.3 Cryogenic system

Electron-hole pairs are generated in a semiconductor detector under reverse bias conditions by ionising radiations. These charge carriers move in opposite directions with a saturated drift velocities proportional to the strength of the applied field. Thermal effects directly related to the temperature of the detector lead to statistical fluctuations in the number of charge carriers. Thus, the Si(Li) detector and the Field Effect Transistor (FET) are cooled with liquid nitrogen to reduce the influence of thermal noise.

To monitor the detector temperature when it is biased, two platinum resistance sensors (PT100) with a resistance of 100 Ω at 0 ^{o}C were connected to the cold finger and cold plate. The PT100 sensory are connected to a 16 channel Precision Thermocouple card (PC 73C) utilizing a constant current and read using the LabVIEW data acquisition system with a built in Experimental Physics and Industrial Control System (EPICS) interface [Epi18]. The typical temperature of the Si(Li) detector in normal running conditions is $\sim$ -130 ^{o}C. Similarly, a PT100 sensor was connected to each of the six magnet coils to monitor their warmup when current is applied to the coils. The coil temperature and nitrogen consumption are also connected to the EPICS library and monitored through a Control System Studio (CSS) either remotely or locally. A rear view of the spectrometer with PT100 sensor attached to the cold plate is shown in Fig. 3.6.

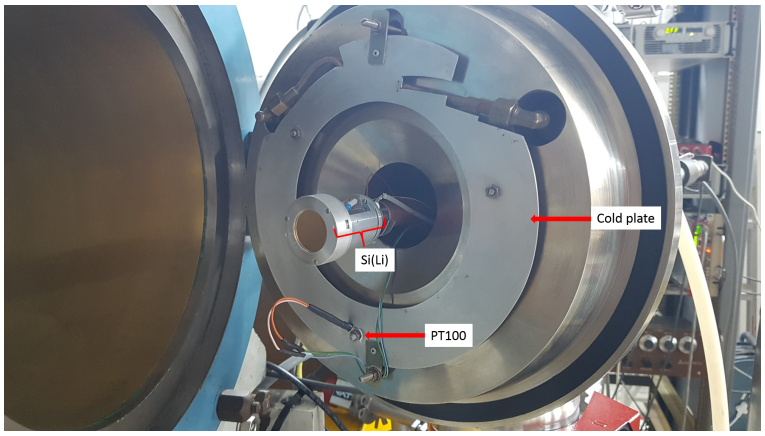

Figure 3.6: A rear view of the spectrometer door showing the PT100 sensor on the cold plate and the 5 mm thick Si(Li) detector.

In Fig. 3.7, the cooling curve for the cold plate and cold finger is shown along with nitrogen consumption rate. In an ideal situation, the two curves should not cross each other. However, the cold plate and cold finger are at different temperatures due to their body mass, therefore, the cold plate curve crosses the cold finger curve by the time the cold finger is already at its room temperature.

3.4.4 Magnet control system

The magnet power supply for the spectrometer is remotely controlled via a serial communication interface through the EPICS library. The spectrometer is operated in lens mode by sweeping the magnet current in steps of 0.1 A/min to cover the whole energy range. The current and voltage are time stamped and saved with the data for gating and analysis purposes. The magnet power supply is hardware interlocked directly on the coils from the magnet cooling water supply. An overview of the remote control system is shown in Appendix B.

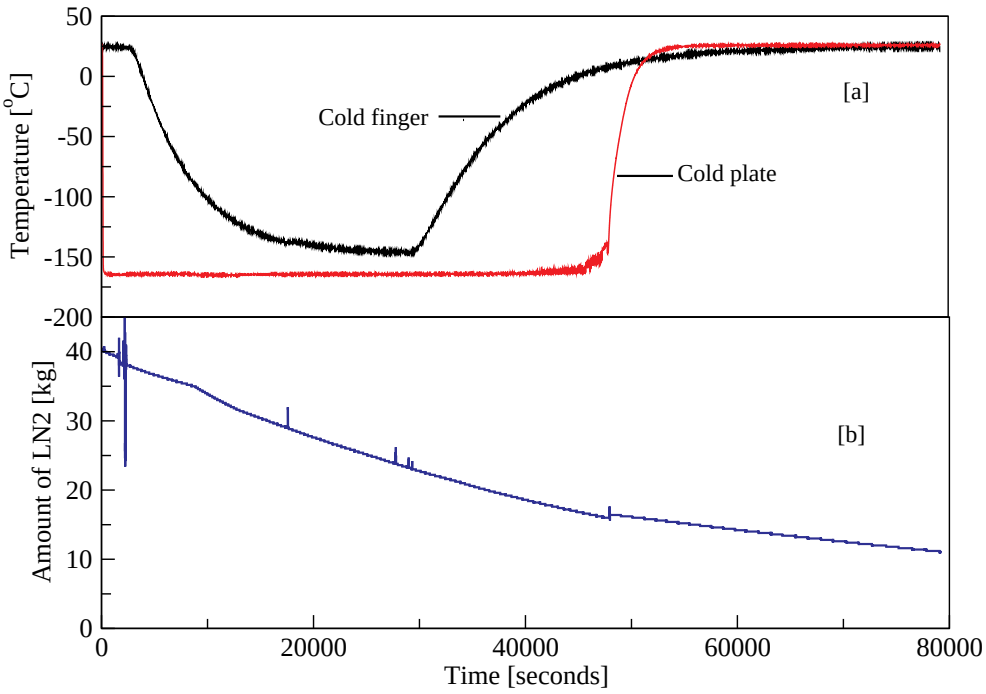

Figure 3.7: Cooling curve of the cold plate and Si(Li) detector (upper) with nitrogen consumption rate (lower).

The linear dependency between the field and current shown in Fig 3.8 was used to obtain a linear function for calibration. This was achieved by fitting a linear function to data points, the gradient (0.0055) and the offset (-0.0003) is then used as a calibration function to convert current to magnetic field.

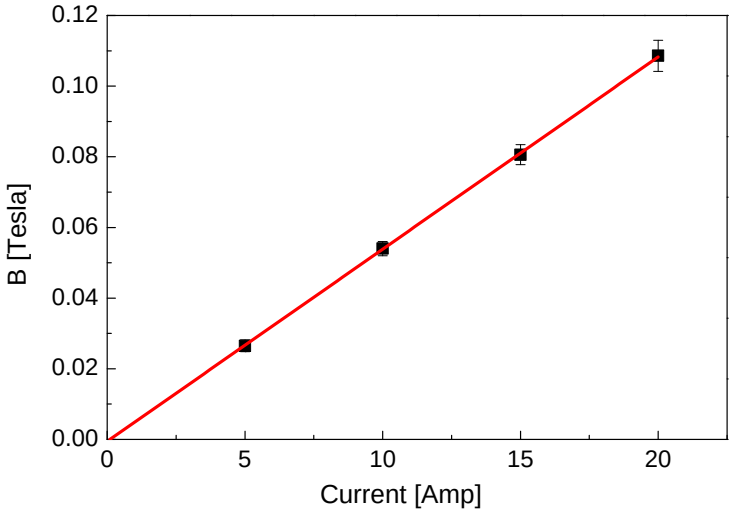

Figure 3.8: Measured axial magnetic flux density as a function of current at the centre of the solenoid (250 mm on the axis). The red line is a linear fit to the data points.

3.5 Electron spectrometer calibration

Spectrometer parameters such as detector resolution, momentum resolution, and transmission efficiency which describe the spectrometer performance were measured with two unsealed calibration sources, ^{207}Bi and ^{133}Ba with activities of 35 kBq and 36 kBq respectively. The setup for the measurement is described in Section 4.2.4.

3.5.1 Momentum window

The momentum window defines the physical limits of the spectrometer in terms of momentum for transporting electrons from the source to the detector. As the mangnetic field strength increases, so do the width and centroid of the momentum window. This implies that the momentum window increases with electron energy

and there is a maximum magnetic field for transportation of a given electron energy. In the case of the spectrometer described here, the range of acceptance angles and the baffle geometry is fixed, thus the effective momentum resolution is a function of electron kinetic energy and magnetic field. One distinctive property of an electron spectrometer is that at a given magnetic field, only electrons within the momentum window defined by the field are transported to the detector [Kib90]. By constructing a two-dimensional matrix of accepted electron energy (E) vs magnetic flux density (B), this relationship is determined over the full energy spectrum.

The source measurements were made with and without a baffle to understand the effectiveness of the baffle system in background reduction and momentum selection. From the E vs B matrix presented in Fig. 3.9, it can be observed from the matrix in the upper panel (with baffle) that the use of a baffle has greatly suppressed the background as the energies are distinct and fit well within the calculated momentum window. Also, the use of baffle limits the angular opening to $7^o \leq \alpha \leq 24^o$ which prevents all electrons with small take off angles from being transmitted to the detector, thus, the electrons make only a single loop before reaching the surface of the detector. In contrast, the matrix in the lower panel which is without baffle show the electrons are transported at all magnetic field settings, this effect is illustrated in Fig. 3.10.

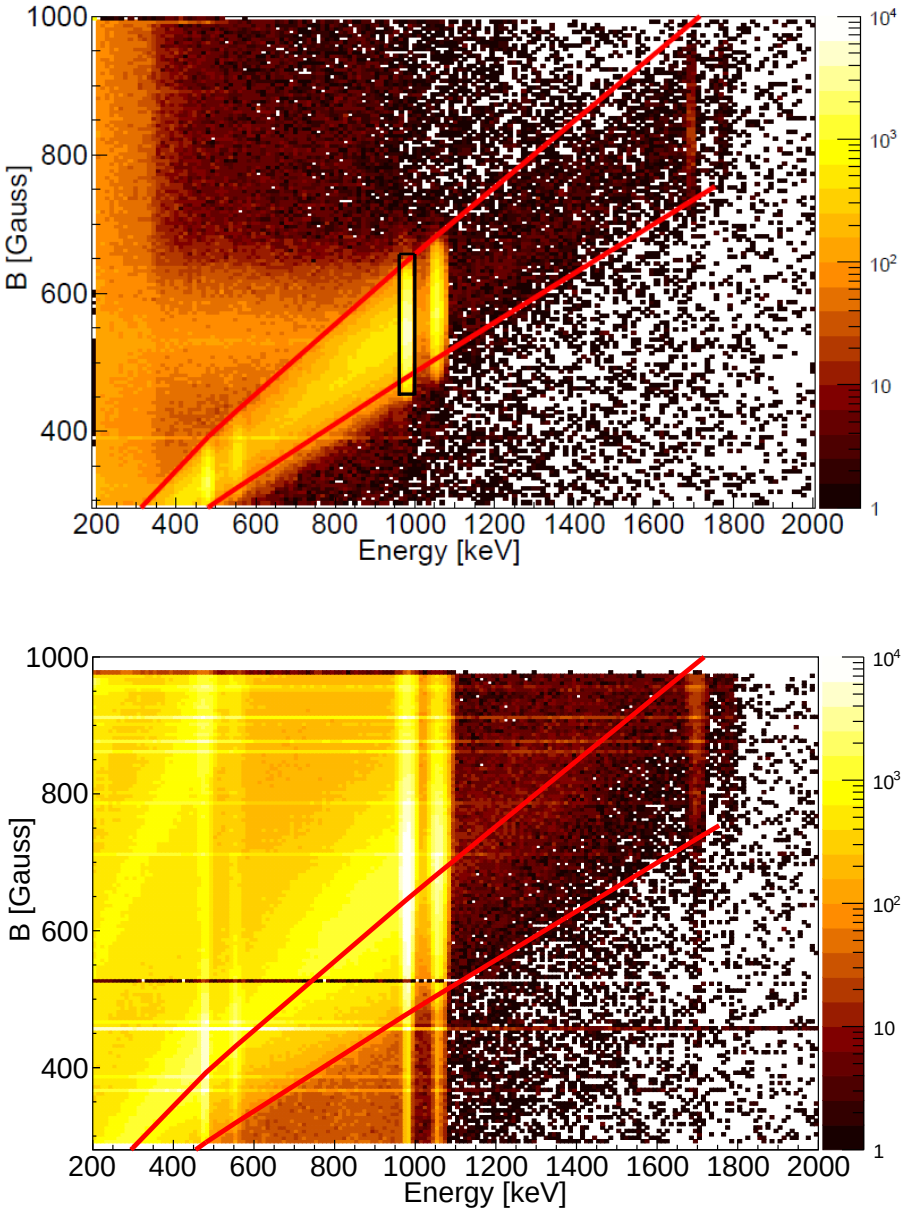

Figure 3.9: B vs E matrix measured with a ^{207}Bi source. Measurements with baffle (upper) and measurement without baffle (lower). The lines represent the momentum window calculated using Eq. (3.2) discussed in Section 3.5.2

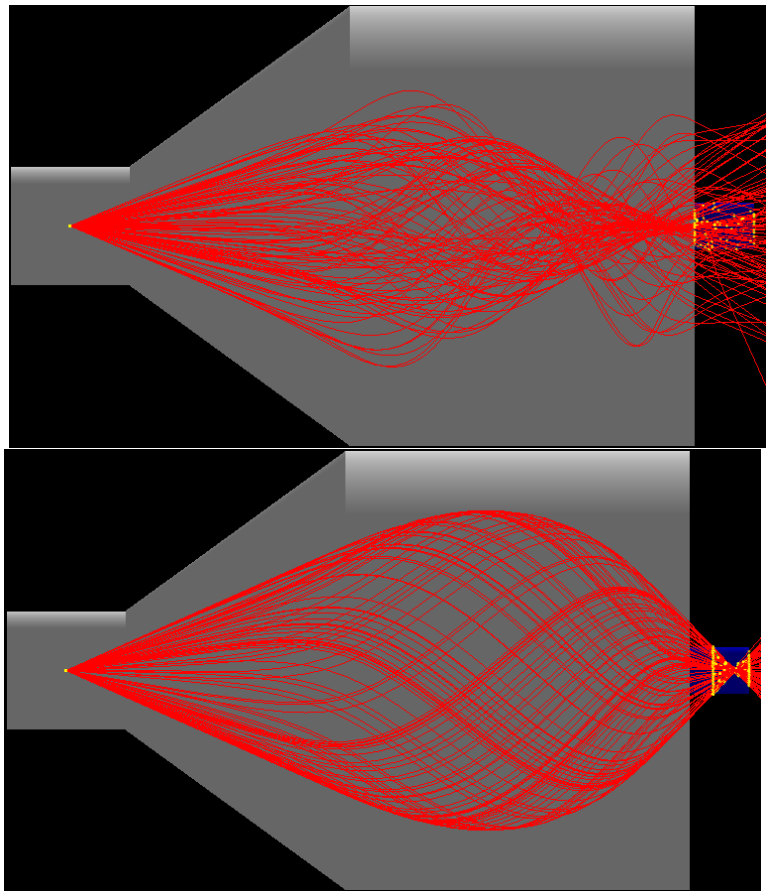

Figure 3.10: An overview of Geant4 simulations of electron trajectory emerging from the source point into the solenoid magnetic field. Without baffle (upper) with baffle (lower) [Chi19].

By setting 2-D momentum gates (field range: 450 G - 650 G) with the same conditions on the two E vs B matrix around the 1064 keV electrons from the K atomic shell following the decay of ^{207}Bi, the energy spectrum is extracted and presented in Fig. 3.11. The conversion electron spectrum obtained without the baffle is overlaid on the measurement with the baffle for direct comparison. It can be observed that the use of baffle has reduced the background such that the Peak-to-Total ratio increased by 27 %. From the measurements without the baffle, the K and L electrons from the decay of 570 keV transition were also transported

alongside the electrons for which the momentum window was set. This is because without the baffle, the electrons emitted at zero degrees (on the solenoid axis) will not experience Lorentz force since the velocity (v) and magnetic flux density (B) is in the same direction, therefore, they travel straight to the detector. However, with the use of the baffle, this effect is eliminated. It is important to state that the nomenclature used in labelling transitions and ICE in this section are transition energy + electromagnetic radiation (e.g., 773 $E2$) and electrons energy + shell (e.g., 773 K).

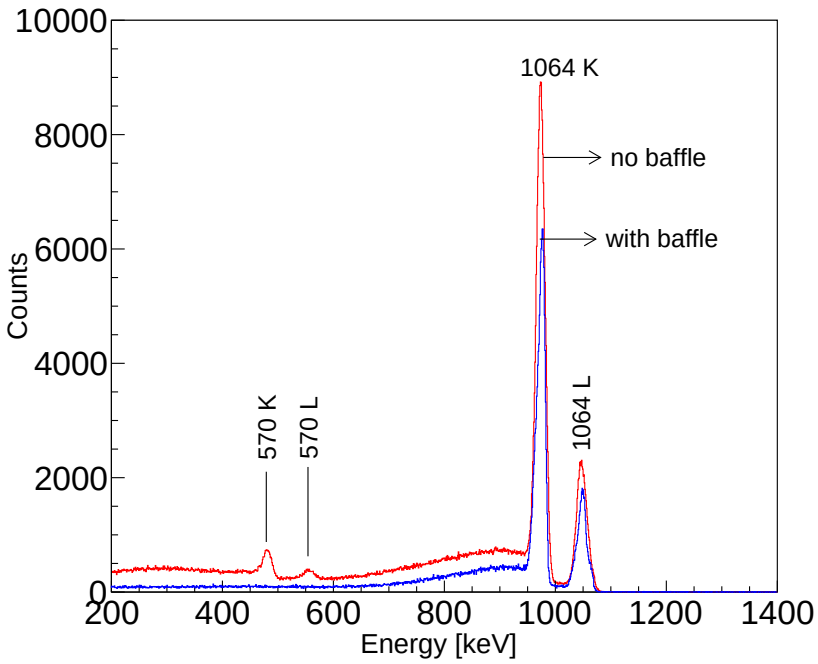

Figure 3.11: Demonstration of background reduction by the baffle system using ^{207}Bi source. The momentum gate was set on the 1064 K conversion electrons.

Another gate was set on the 1064 K transition to extract the momentum distribution. The distribution presented in Fig. 3.12 depicts the momentum distribution of the magnetic lens. The momentum selection allows both the K and L conversion electrons from the 1064 keV transition to be transported. This is due to the

fact that the width of the momentum distribution is above 72 keV which is the separation energy between the K and L electron for ^{207}Bi. By obtaining the three field limits marked B_{lower}, B_{max}, and B_{upper} from the momentum distribution, the B-E dependency shown in Fig. 3.13 was constructed by fitting the data points to a power function defined according to Eq. (3.3).

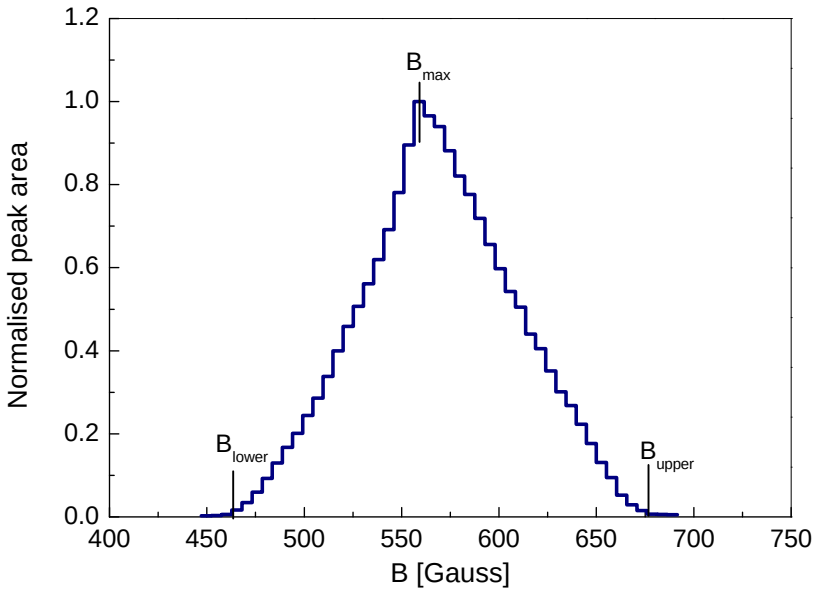

Figure 3.12: The acceptance window for the 1064 K transition in ^{207}Bi.

3.5.2 Geant4 simulation of spectrometer properties

A simulation using Geant4 version 10.3 [Ago03] was carried out to optimize the transmission of conversion electrons by the solenoid magnetic lens to the Si(Li) detector. The field generated by the magnetic lens at a given current was mapped using OPERA 3D [OPE19] and the field grid was imported into Geant4 [Chi19]. Each magnetic field mesh extracted corresponds to a given current, thus, capable of transporting only electrons of a specific kinetic energy. Therefore, the field was

scaled (linearly) up or down to correctly focus the corresponding ICE onto the detector. The spectrometer was built in Geant4 using its actual dimensions and materials to reproduce, as much as possible, the real physical geometry of the spectrometer.

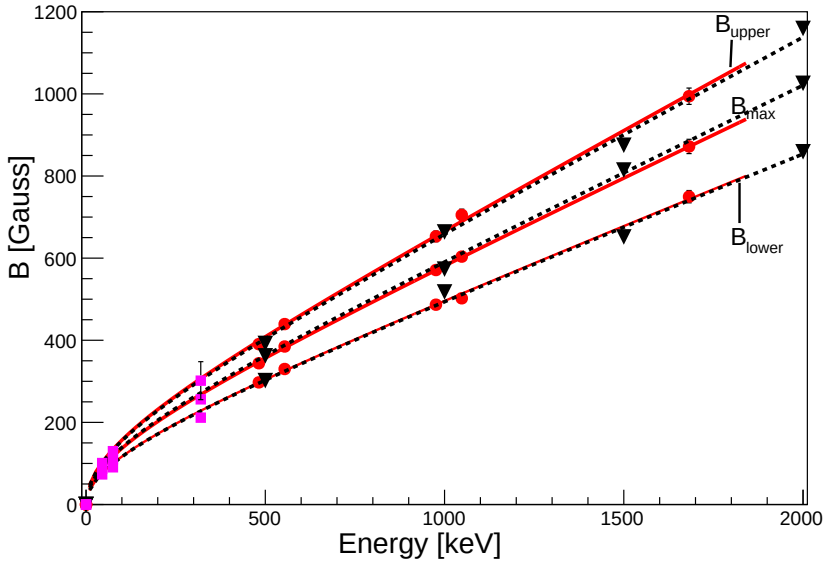

Figure 3.13: Experimental (red circles) and simulated (black triangles) rigidity curves constructed to show the B-E dependence deduced from the momentum distribution for ICE emitted from the decay of ^{207}Bi and ^{133}Ba. The purple squares and the red circles represent the data points from ^{133}Ba and ^{207}Bi, respectively. The solid and dashed lines are the fits to the experimental and simulated data points, respectively.

A total of one million events were sampled for each ICE energy emitted from ^{133}Ba and ^{207}Bi sources at 50 mm from the magnetic lens. The divergence angles of the electrons were restricted to the angular opening quoted in Section 3.5.1. Three field limits were obtained from the simulated form of the momentum distribution using the procedure described in Section 3.5.1. For direct comparison, the field limits were plotted together with the measured values in Fig. 3.13, which provides an excellent agreement of $\sim$ 95 % between the experimental results and the simu-

lation. Other results from the simulations which yielded figures of merit (FOM) of the spectrometer, namely the transmission efficiency, momentum resolution and spectrometer efficiency are presented in Table. 3.1.

With the extracted fields limits, the momentum window of the spectrometer at any electron energy can be obtained using the expression

$$B_i(E) = C_i B\rho \tag{3.2}$$

$$B\rho(E) = \frac{0.001074 T m \sqrt{E^2 + 2m_o c^2 E}}{m_o c^2} \tag{3.3}$$

where Bρ is the magnetic rigidity, $m_o c^2$ is rest mass of the electrons and C_i is the field-energy relationship coefficients obtained by fitting Eq. (3.3) to the data points in Fig. 3.13.

3.5.3 Spectrometer efficiency calibration

The total detection efficiency of the spectrometer array depends on the transmission efficiency of the magnetic spectrometer T(E) which is the ratio of the number of emitted electrons to the number of electrons transported to the front face of Si(Li) detector and the efficiency P(E) of the Si(Li) detector. Therefore, the total efficiency can be defined as the product of the transmission efficiency (energy dependent since the field was swept) and detector efficiency which is energy dependent as well. To obtain the absolute transmission efficiency of the spectrometer, branching ratios from Ref. [Mar93,Rab95] and K conversion coefficients from Ref. [Kib08] were used. A relative efficiency curve for all the conversion electrons was generated using relative intensities from Ref. [Trz90] and peak areas from the momentum-gated spectra. The absolute transmission efficiency values of 570

K and 356 K from the decay of ^{207}Bi and ^{133}Ba respectively were used to correct for the efficiency and to normalize the two data sets. This was achieved by scaling the relative efficiency values for the 570 K and 356 K decays to match the absolute values obtained using the source activity. The weighted average of each of those absolute values divided by the corresponding relative values provide a normalization factor for all the relative efficiency values. The total detection efficiency of the spectrometer was therefore straightforwardly deduced by multiplying the transmission T(E) by the detector efficiency (intrinsic) calculated using Geant4 [Ago03]. The calculated efficiency of the Si(Li) is shown in Fig. 3.14. A typical measured momentum-gated spectrum of ^{207}Bi used to determine the total effciiency of the spectrometer is presented in Fig. 3.15. The resulting total efficiency of the spectrometer is illustrated in Fig. 3.16 where it is compared with simulation results. The simulated efficiency seems to follow the same trend exhibited by the measured values around 45 keV to 1.0 MeV. The drop of the efficiency at lower energies and above 1.0 MeV is the effect of sweeping the magnetic field and is consistent with the efficiencies of other spectrometers operated in lens mode [Kib90, Soh97].

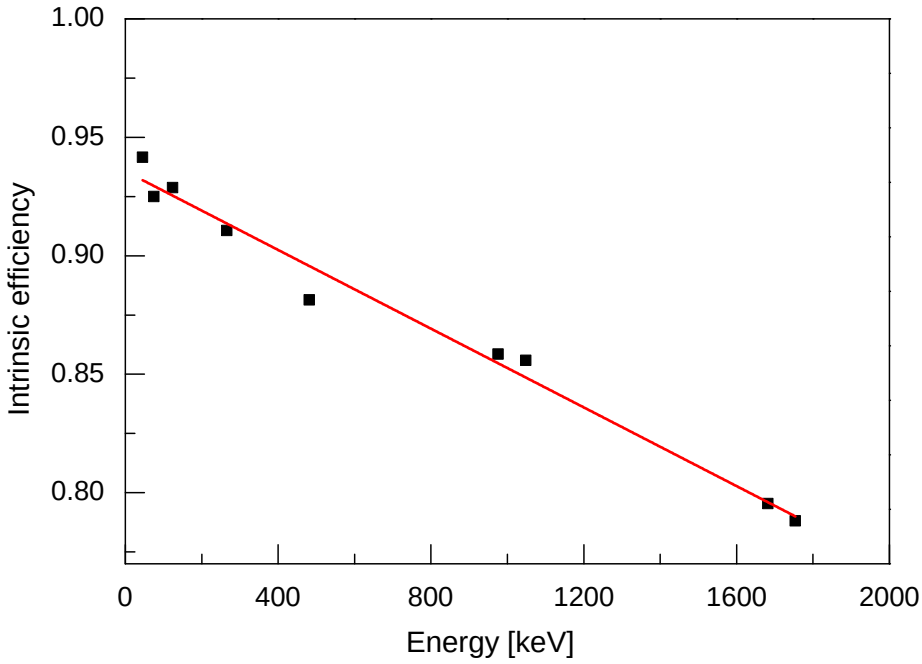

Figure 3.14: Simulated Si(Li) detector efficiency from the total spectrum. The red line is a linear fit to the simulated points.

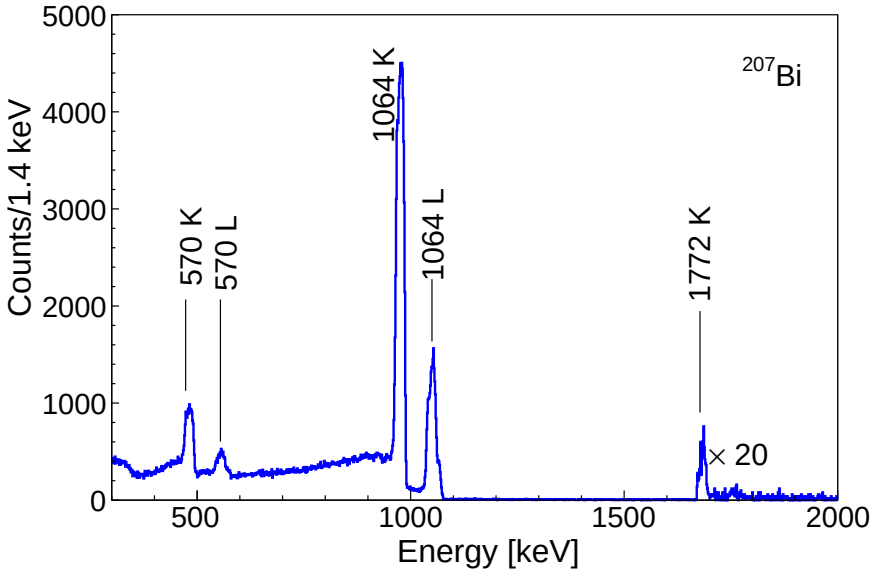

Figure 3.15: A typical momentum gated conversion electron spectrum of ^{207}Bi used to determine the spectrometer efficiency.

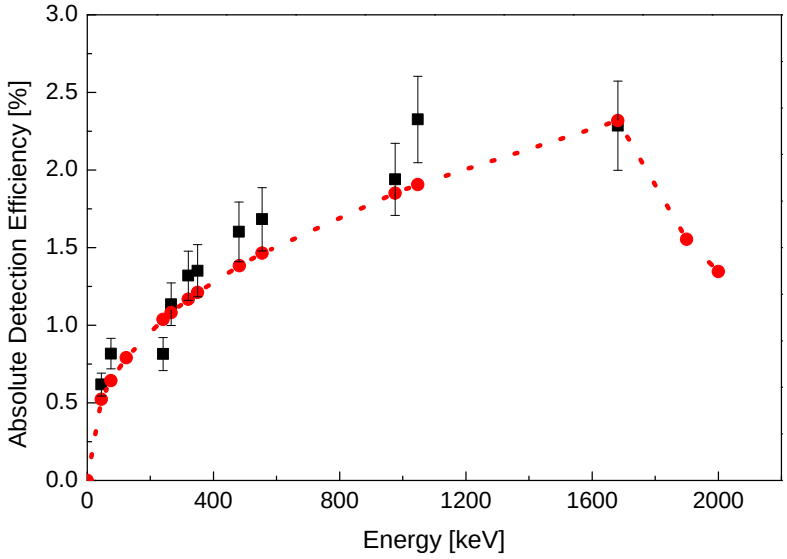

Figure 3.16: Comparison of measured absolute spectrometer efficiency (squares) with simulations (circles) for electrons from ^{133}Ba and ^{207}Bi sources.

Table 3.1: Measured and simulated FOM of the spectrometer using the 1064 K conversion electrons from ^{207}Bi.

Physical properties	**Measured**	**Calculated**
Solid angle [% of 4π]		4.2
Momentum resolution (%)	19(14)	21
Energy resolution [976 keV](keV)	16.0(2)	
Transmission efficiency [%]	2.9(4)	2.7
Detection efficiency [%]	2.3(3)	2.3
C_i coefficients		
C_{lower}	10.40(7)	10.21(2)
C_{max}	12.23(4)	12.32(5)
C_{upper}	14.06(6)	13.48(6)

It should be noted that the energy resolution of the spectrometer has been rectified to 4.5 keV at 320 keV.

Chapter 4

Experimental Techniques

The main objective of this study is to determine the strength of the $E0$ transitions by measuring internal conversion and internal pair coeffcients together with corresponding gamma rays. This will give access to nuclear information on the products from alpha, α and proton, p induced reactions on ^{70}Ge and ^{54}Cr targets, respectively. In this chapter, the experimental techniques utilizing the refurbished electron spectrometer at iThemba LABS as shown in Chapter 3 shall be discussed, followed by a complementary experiment performed at the Australian National University (ANU), Canberra.

4.1 Experiment at iThemba LABS

The experiment was performed using the newly characterized electron spectrometer as a test of principle. The goal of the experiment was to obtain spectroscopic information from the different reactions to study the nuclear structure of ^{72}As, ^{72}Se and ^{72}Ge. Properties of beam and target are discussed in this section followed by detailed description of equipment and experimental techniques used.

4.1.1 ^{70}Ge target preparation

The targets were produced starting with ^{70}Ge powder supplied by ISOFLEX, with an isotopic enrichment of 97.60 %. The powder was pelletized with a hand presser to form a pill to avoid losing the material during the heating process under vacuum. The pill was transferred into the copper hearth of an electron gun and the system was taken down to negative gauge pressure using a turbomolecular pump. The heating of the germanium (Ge) was conducted when the pressure of the system was at 10^{-5} mbar, which is the recommended pressure to perform vacuum depositions of materials using the electron heating of the vacuum evaporation system [Mat10]. The deposit of the ^{70}Ge was collected on a polished stainless-steel plate coated with a thin layer of $BaCl_2$ which acts as a parting agent. Once the deposition was complete, the system was allowed to cool and vented with argon to break vacuum. Thin films of ^{70}Ge were floated off from the substrates using deionized water and mounted on the desired frames. The targets were further characterized by X-ray fluorescence (XRF) to verify their thickness. Final thickness of the targets after the XRF measurements were 0.31, 0.37, 0.44, and 0.46 mg/cm^2 with uncertainties on the thickness of $\sim$ 3 %. For this measurement ^{70}Ge target with area density of 0.46 mg/cm^2 was utilized.

4.1.2 Alpha beam

A beam of alpha particles was chosen to probe the nuclear structure of ^{70}Ge due to the fact that inelastic α-scattering is an ideal probe for isoscalar monopole (IS0) excitation [Sch87]. A $^4_2$He beam was prepared using the Grenoble Test Source (GTS) Electron Cyclotron Resonance (ECR) ion source [Tho08]. The GTS-ECR ion source is coupled to 14 GHz and 18 GHz microwave generators. However, to

produce $^{4}_{2}$He beam, only the 14 GHz microwave frequency was utilized. The beam is extracted from the ion source with initial energy of 0.164 MeV, and transported to the second solid pole injector cyclotron (SPC2) via the Q and AX beam line for pre-acceleration. At the SPC2, the beam is accelerated to 1.5 MeV and sent to the Separated Sector Cyclotron (SSC) through the K and J line for final acceleration to 30.0 MeV, and subsequently transported through the X and P line to the G line where the electron spectrometer is located. The beam is focused with a solenoid of length 200 cm between the Q and AX line and from the AX line to the G line where it is delivered on ^{70}Ge target, it is focused with series of quadrupole magnets.

The beam energy was chosen based on TALYS-1.9 [Kon17] calculations performed using different alpha-particle beam energies on a ^{70}Ge target. It should be noted that the minimum alpha beam the cyclotron can accelerate is 30 MeV. The results of the residual production cross section per nuclide is presented in Fig. 4.1. It can be seen from the results that at 30 MeV, the cross-section for the population of all states for the $(\alpha, \alpha^{'})$ reaction is $\sim$ 100 mb. The $(\alpha, np\gamma)$ and $(\alpha, 2n\gamma)$ reactions have the highest cross section. The total reaction cross-sections obtained using TALYS is 1342 mb.

4.1.2.1 Calculation of angular beam spreading

A beam pipe extension was made to couple the spectrometer to the G-line at iThemba LABS using a stainless-steel pipe of 20 mm radius connected to a 48 mm radius pipe leading to the beam dump. It was necessary to determine post target spread of the beam to check the extent of interaction with the beam pipe, to ensure that beam-induced background such as neutron background and shower

particles are avoided [Fod17]. To this effect, calculations were performed using Transport of Ions in Matter (TRIM-2012.0) program, which is a package in the Stopping and Range of Ions in Matter software (SRIM-2012.0) [Zie13] to determine the angular spread of the scattered beam after interacting with the target material.

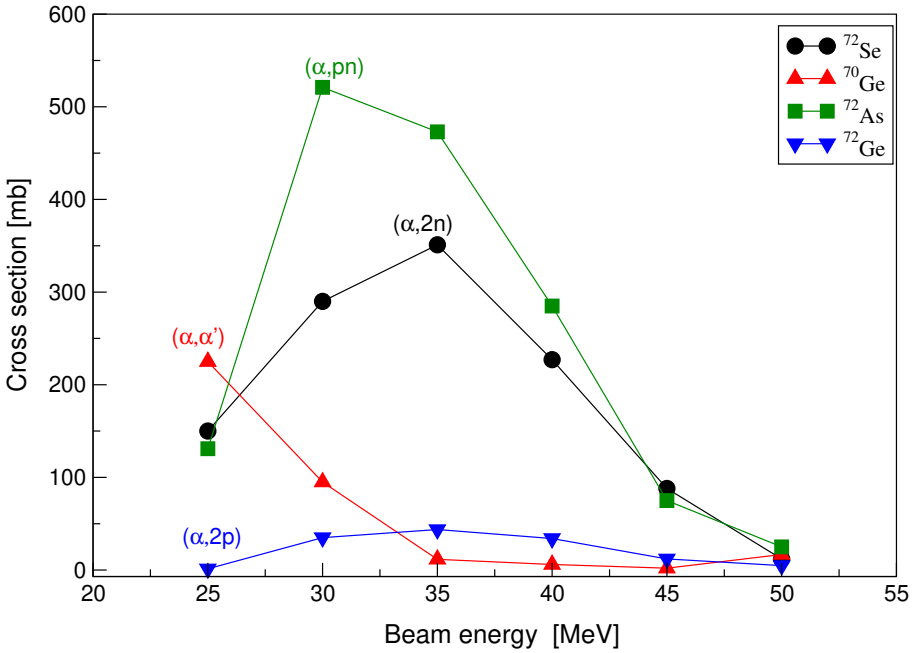

Figure 4.1: Reaction cross section for possible decay channels.

A screenshot of the SRIM calculations showing post target angular spread of beam particles inside the beam pipe is shown in Fig. 4.2. It can be inferred that the spread of the particles is less close to the target and increase towards the beam dump. By projection unto the y-axis at three position on the beam length, the angular spread from the central axis of beam pipe at each position is obtained as shown in Fig. 4.3. It implies that post target scattering of the beam is more at the end of the beam pipe, thus, it is less likely that there will be any effect of

beam-induced background.

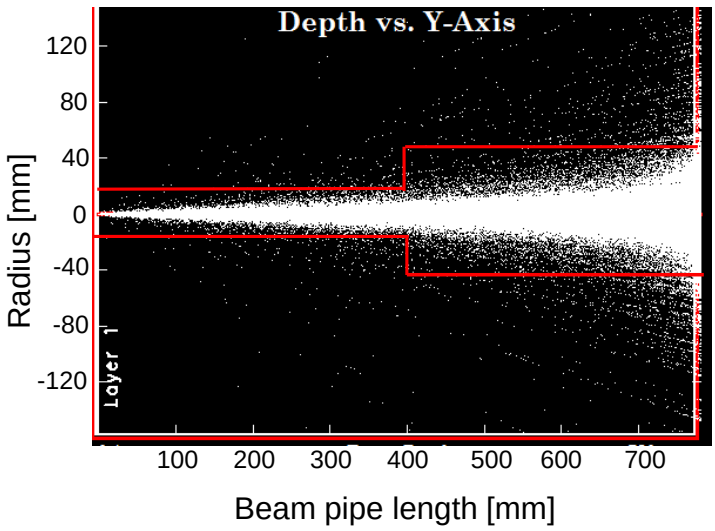

Figure 4.2: A screenshot of post target beam spread inside the beam pipe. The target position is at 0 mm.

4.1.2.2 Kinematic of ^{70}Ge(α,X)Y reactions

Given the laboratory energy of the projectile (α) as 30 MeV, the reaction dynamics were calculated using SRIM [Zie13]. The results gave the velocity of the projectile as 12.6 % of the speed of light, and 28.31 MeV the centre of mass energy. The reaction produced a compound nucleus of mass 74 a.m.u which recoils with a kinetic energy of 1.6 MeV and velocity, of 0.69 % of the speed of light in the laboratory frame. From these values, a Doppler shift of $\sim$ 1.4 keV and $\sim$ 6.8 keV at 180° is expected for 0.2 MeV and 1.0 MeV gamma rays, respectively. In order to determine if the recoiling nuclei stop inside the target or exit the target, the recoil energy and target density of $\rho(^{70}\text{Ge}) = 5323$ mg/cm^3 were used in SRIM to evaluate the maximum range of the recoil nucleus.

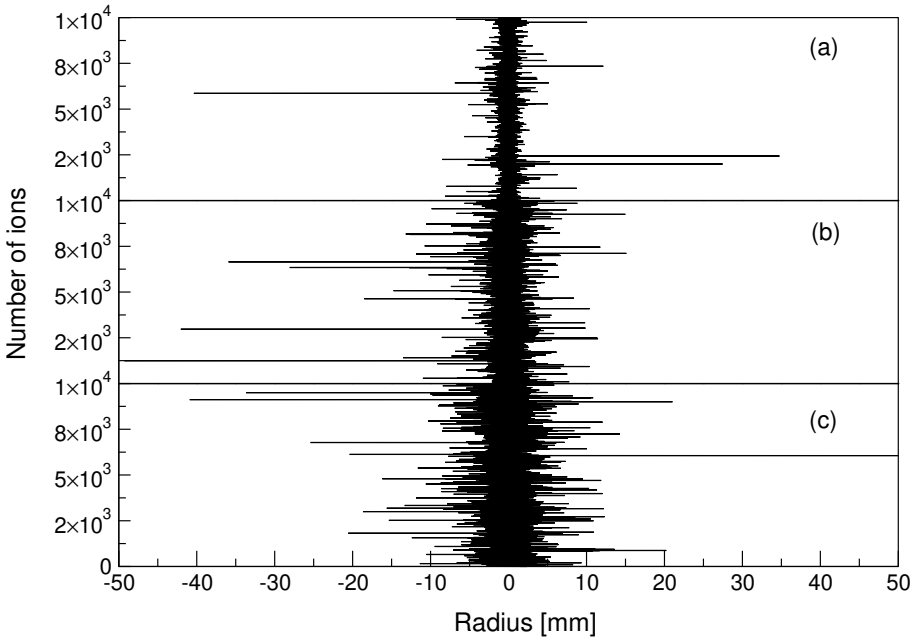

Figure 4.3: Number of scattered ions along the radial axis of the beam pipe. (a) at 390 mm, (b) at 585 mm, (c) at 780 mm.

The target is positioned at 45 degrees with respect to the beam direction, therefore, the effective target thickness x_{eff} is deduced from

$$x_{eff} = \frac{x}{cos(\pi/4)}, \tag{4.1}$$

assuming that the recoil is in straight path. Where x is the target thickness given as 0.46(2) mg/cm^2 $\equiv$ 0.86 μm. The target is usually provided in area density, so one has to divide by the density of the target material to obtain the spatial thickness. The kinematics is summarized in Table. 4.1. From the maximum range of the recoil ions inside Ge it can be inferred that the recoils will travel $\sim$ 0.4 μm to exit the target.

Table 4.1: Reactions characteristics of the alpha induced reaction on ^{70}Ge target.

Physical properties	quantity
Beam enery [MeV]	30
Center of mass energy [MeV]	28.31
Beam current [nA]	8
Recoil velocity β (v/c) [%]	0.7
Compound nucleus recoil energy [MeV]	1.6
Target thickness [mg/cm^2]	0.46(2)
Effective target thickness [μm]	1.2(3)
Maximum range of ^{72}Ge [μm]	0.8
Maximum range of ^{72}As [μm]	0.7
Maximum range of ^{72}Se [μm]	0.7

4.2 Electron and gamma-ray detection

The energy emitted in the de-excitation process is measured with semiconductor and scintillator detectors in this study. In semiconductor detectors a large cloud of electron-hole pairs which are charge carriers are created as the emitted radiation interacts with the large volume of crystalline material. The pairs are accelerated in an electric field and the total charge that is collected at the electrodes is proportional to the amount of energy deposited in the detector [Reg03]. On the other hand, in a scintillator detector, ionizing radiation is converted to a light pulse or scintillation. Each scintillation is converted into an electronic pulse by a photomultiplier tube (PMT), which also amplifies the electron current by 5 or 6 orders of magnitude [Sai14]. The decay time of the induced scintillation is generally, very short, and as a result fast signals are generated by the scintillator.

Hence, they are suitable for fast timing measurements [Gil08].

Electrons are detected by lithium-drifted silicon detector because it has good energy resolution, stability of operation and thin entrance windows. If the incident electron has enough energy to ionize atoms in the detector materials, it will thus, interact with the neighbouring atoms and in each interaction, the kinetic energy is transferred to the atom and eventually the electron stops within the detector thickness after imparting all its kinetic energy. Another way by which electrons lose energy in the detector material is through bremsstrahlung as the electrons interact with other orbital electrons. On the other hand, gamma rays interact with the detector material and lose energy through any of the three processes: Photoelectric absorption, Compton scattering and Pair production discussed briefly in the next subsections.

4.2.1 Photoelectric absorption

In photoelectric absorption, the incident gamma ray interacts with an atomic orbital electron of the detector material which results in the emission of photoelectrons from the electron shells. The electron is emitted with a kinetic energy equal to the difference between the energy of the incident photon and the energy binding the electron to its original shell. The emitted electron creates a vacancy in the electron shell which is filled by neighbouring electrons from higher orbits resulting in the emission of a characteristics X-ray or Auger electrons. These X-rays or Auger electrons are usually reabsorbed in the detector material due to their low energy [Kno00, Gil08]. The probability of photoelectric absorption is higher at low energies in detectors made with materials of high atomic number, Z .

4.2.2 Compton scattering

Compton scattering occurs when the incident gamma ray interacts directly with an orbital electron, transferring part of its momentum and energy to the electron which then recoils through the detector volume. An illustration of a Compton scatterd gamma ray is shown in Fig. 4.4.

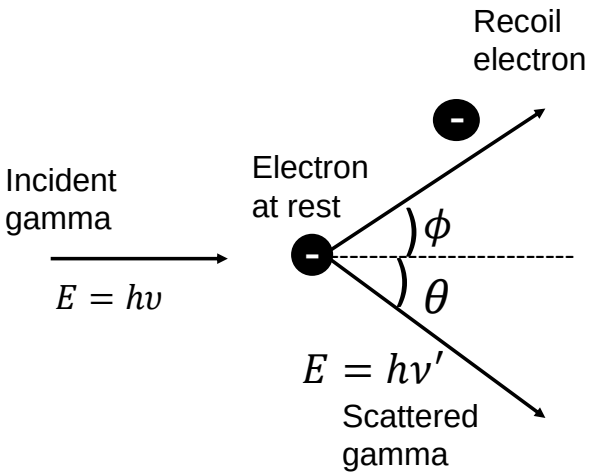

Figure 4.4: Overview of Compton scattering by an incident gamma ray, θ is the scattering angle and ϕ is the recoil angle.

The amount of energy transferred to the recoil electron is given by ΔE, where

$$\Delta E = h\nu - h\nu' = h\nu \left(\frac{\frac{h\nu}{m_e c^2}(1 - cos\theta)}{1 + \frac{h\nu}{m_e c^2}(1 - cos\theta)} \right), \tag{4.2}$$

where $h\nu$ is the energy of the incident gamma ray and $h\nu'$ is the energy of the scattered gamma ray. Because all angles of scattering are possible, the energy transferred to the electron can vary from zero to a large fraction of gamma-ray energy. The probability of Compton scattering per atom of the absorber depends on the number of electrons available, hence it linearly increases with atomic number, Z [Kno00, Gil08].

4.2.3 Pair production

Contrary to the processes discussed in the two preceding subsections, pair production occurs due to the interaction of the gamma ray with the whole atom. It takes place within the Coulomb field of the nucleus during which the gamma ray is converted into electron-positron pair which share the total kinetic energy equivalent to the gamma-ray energy minus $2m_0c^2$ (2×0.511 MeV). In practice, this process only becomes energetically possible as the transition energy exceeds 1.022 MeV. The positron emitted eventually loses its energy typically a (space of 1.0 ns) as it travels through the detector and will annihilate with another electron creating two 511 keV photons [Kno00, Gil08].

4.2.4 Detectors

The electrons were measured in vacuum with a Si(Li) detector of active area 500 mm^2 connected to a cold finger cooled to liquid nitrogen temperature. The Si(Li) detector has a resolution of 16 keV at 976 keV. The resolution was due to electronic noise from instrumentation effects, however, it has subsequently been rectified and the rectified resolution is discussed in Subsection 4.2.5. To transport electrons in the energy range of 45 keV to 1.2 MeV unto the detector, the magnetic field was sampled from 2.00 A to 14.00 A. The field values were calculated according to Eq. (3.2) using the field-energy coefficients in Table. 3.1. For gamma ray measurement, six $2'' \times 2''$ fast-timing $LaBr_3$:Ce detectors with Brilliance:Ce-380 crystals manufactured by Saint Gobain Crystals coupled to a R2083 (PMT) were used. The $LaBr_3$:Ce has an energy resolution of $\sim$ 3 % at 1.33 MeV and an excellent timing resolution of $\approx$ 300 ps. In addition, two 2800 mm^2 planar LEPS constructed with p-type HPGe segmented electrically into quadrants [New98] with

a resolution of 1.3 keV each at 121 keV, were used for the measurement of low-energy photons.

The motivation for the use of two types of gamma ray detectors is necessitated due to the intention to measure both low and high energy gamma ray transitions depopulating the lowest excited states. The LEPS has good energy resolution and reasonably high efficiency at energies from 50 - 300 keV [Sar09, Szu11]. On the other hand, the $LaBr_3$:Ce has a moderate energy resolution but a very high efficiency, thus, a combination of the two detector systems produce an excellent system with high efficiency and high energy resolution at this energy domain [Bas15]. In addition, the low-energy response for X rays of the LEPS detectors can be used in conversion electron studies and X-ray yield analysis. The complete experimental set up used for these measurements is shown in Fig. 4.5.

4.2.5 Improved Si(Li) detector resolution

After the in-beam experiment the spectrometer was moved to a standalone location and a thorough grounding and recabling was done. This led to significant improvement in the energy resolution from 16 keV to 4.5 keV at 320 keV. Fig. 4.6 shows the spectra of ^{133}Ba with the improved setup. The spectra were measured with the 8 blade baffle used in the ^{70}Ge experiment and a straight baffle without blades. The counts in the spectrum with the straight baffle is 20 % higher at all energies Therefore, in order to gain in efficiency, it is recommended that in subsequent experiments, there should be a repeat of source taste with this baffle to compare with previous calibration.



Figure 4.5: Side view of the spectrometer array (upper) showing the 1: LEPS, 2: the beam line, 3: $LaBr_3$:Ce detectors, 4: target ladder, 5: magnetic lens, 6: Si(Li) cold finger and 7: Dewar used for the measurements. Front view (lower).

4.2.6 Data acquisition

A total of twenty one signal cables, namely the slow and fast signals from six $LaBr_3$:Ce detectors; four signals from each of the two LEPS (HPGe) detectors and one from the Si(Li) detector, were used in this experiment. The cables were connected to two XIA DGF-PIXIE 16, 500 MHz and 100 MHz, pulse processors for data acquisition [Jon12]. Incoming signals are digitized and three digital filters were applied, namely, a digital constant fraction (CFD) filter, a fast and a slow trapezoidal filter. The Constant Fraction Discriminator (CFD) provides a timing

signal which is related to the time of occurrence of the gamma ray detection.

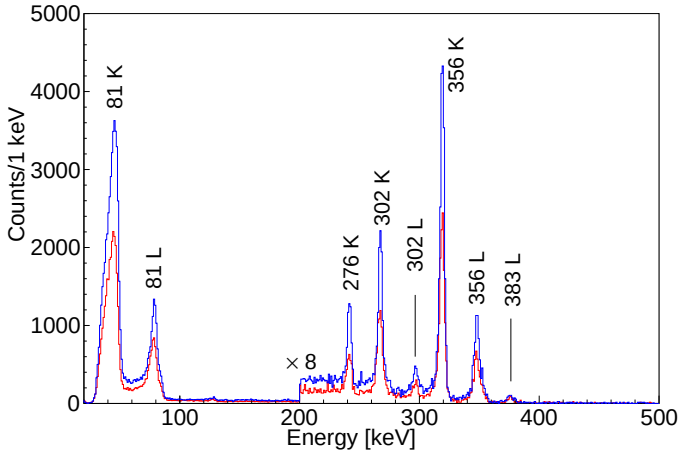

Figure 4.6: ICE singles spectra of ^{133}Ba. Red line is measurement with the eight baffle system and blue line is measured with the straight baffle.

The field programmable gate array (FPGA) implements pulse detection, triggering, discrimination, pileup inspection and a trapezoidal energy filter digitally. Waveforms of each event such as trigger threshold, filter rise and flat top time were customized. Validated events were processed by the Digital Signal Processor (DSP) and those events that are not validated are eliminated with zero dead time. The DSP reads out the energy filter from the FPGA and computes the pulse height and performs other tasks such as constant fraction timing and rise time calculation [Mse19]. The data are transferred via Ethernet to a collection unit for processing and correction of time ordering per card. The data were then transmitted to the merge to be timestamped and ordered in a single stream [Jon12] before being written to disc for offline analysis. In addition, power supply current and voltages were recorded with the Si detector data. A block diagram of the electronics is shown in Fig. 4.7.

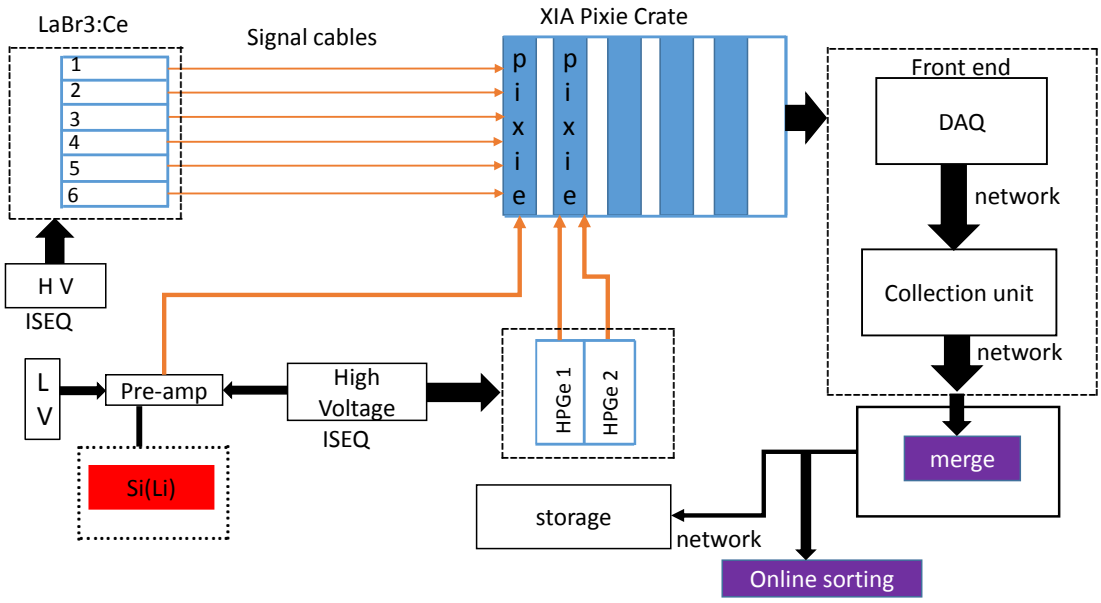

Figure 4.7: Block diagram of the digital data acquisition system showing the detectors and associated electronics. The HPGe are the LEPS detectors, each have 4 signal cables, while the $LaBr_3$:Ce provide fast and slow signals.

4.2.7 LEPS and $LaBr_3$:Ce detection efficiency

The gamma ray detection efficiency of the spectrometer was determined using a ^{152}Eu sealed source and ^{133}Ba open source and the absolute efficiency is presented in Fig. 4.8. The efficiency of the six $2'' \times 2''$ $LaBr_3$:Ce used is consistently higher than the efficiency of the two 10 mm×60 mm LEPS detectors at all energies by an order of magnitude across the energy spectrum. The reason for the deviation is attributed to the difference in the linear attenuation co-efficient (μ) of the detector material. For $LaBr_3$:Ce, $\mu = 2.7$ cm^{-1} and 1 cm^{-1} for LEPS at 200 keV. At higher energies, the difference could also be due to geometry factor between the two detectors. The total photopeak combined efficiency of the spectrometer at 100 keV is $\sim$ 34(4) % and about 6.0(5) % at 1000 keV.

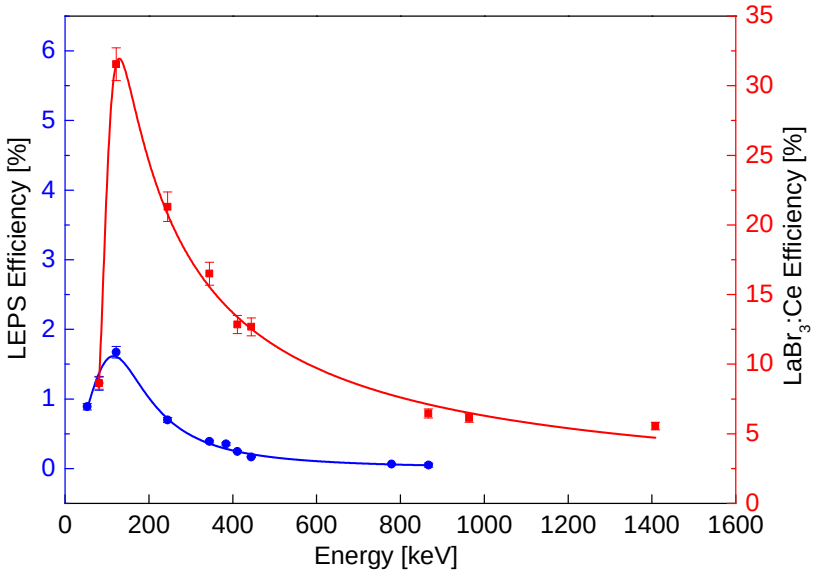

Figure 4.8: Plot of total absolute efficiency of the LEPS detectors (blue circles) and $LaBr_3$:Ce (red squares). The lines represent an exponential fits to the efficiency data points.

4.3 Data analysis for ^{70}Ge(α,X)Y reaction

The data were sorted in MIDAS [MID19] using an MTsort program [Cre15]. As earlier stated, the spectrometer was operated in lens mode where the field was swept from a lower to an upper limit. This information was used to create conditions in the sort code to increment electron energy versus time and electron energy versus current matrices. The field limits described in Subsection 3.5.1 were used to create $B\rho$(E) gates which were used as an additional condition in creating a two-dimensional electron-gamma coincidence matrix in addition to the time window. This improves the peak-to-background ratio as the unwanted background is reduced by the $B\rho$(E) condition. Peak fitting was performed using Radware version 1.2 [Rad95] and ROOT Data Analysis Framework version 5.34/36 [ROO16].

A Gaussian function combined with a skewed Gaussian to account for low energy tails due to incomplete charge collection and a smoothed setup function to increase the background on the low-energy side of the peak were used to fit the peaks in the conversion electron spectra.

4.3.1 Total reaction cross section

To determine the total cross-section from the α-induced reaction, Eq. (2.79) is modified to account for the detector efficiency. Reaction rates of 28(3) kHz were obtained from the sum of the six $LaBr_3$:Ce spectra. To eliminate the time when there was no beam on target, cuts were made on the counts versus time spectrum as shown in Fig. 4.9. By using the beam intensity of 8.0(2) nA and target thickness t of 0.46(2) mg/cm^2 with a charge state of +2, the corrected total reaction cross section is calculated as

$$\frac{R}{I_a N t \epsilon_t} = 797(96) mb. \tag{4.3}$$

The uncertainty on the cross-section is from the target thickness, reaction rates and beam current. Comparing the result of the total cross-section in this experiment with TALYS calculation, it can be observed that, the measured cross-section is ∼60 % of the theoretical cross-section. It is obvious the assumption that every reaction produces a gamma ray is not correct, thus the discrepancy in the cross-section results. This information is crucial as this is the first in-beam experiment with the spectrometer, thus subsequent users may find it resourceful in estimating the number of shifts while proposing experiments.

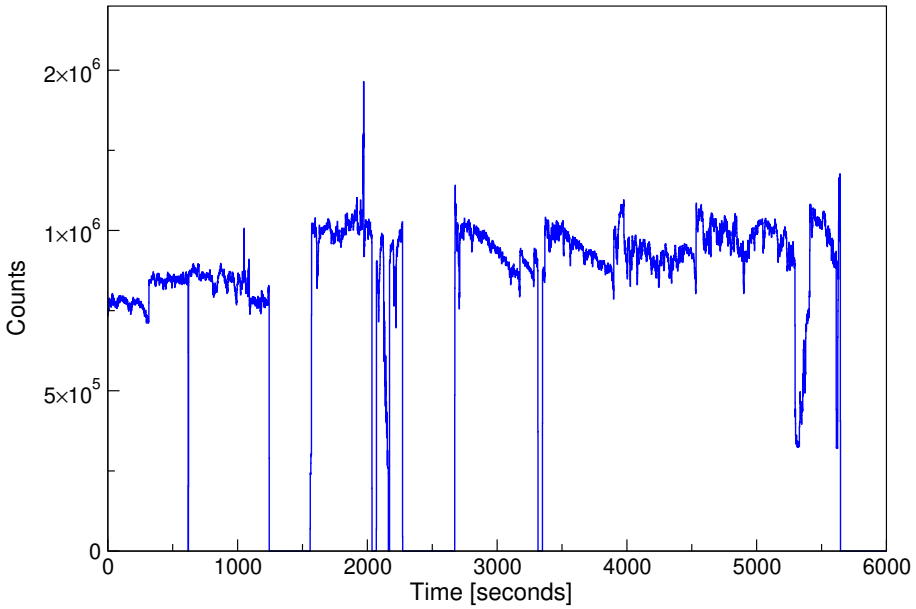

Figure 4.9: Plot of counts versus time of the six $LaBr_3$:Ce detectors.

4.3.2 Gain shift corrections

The energy calibration of the detectors was performed using ^{152}Eu and ^{207}Bi sources before collecting in-beam data. The same sources were used to create gain coefficients which were used for online sorting. However, during offline sorting, it was observed that peaks from both the six $LaBr_3$:Ce and the two LEPS detectors did not align due to a drift in the gain. Gain drift can occur as a result of temperature fluctuations during the experiment, photomultiplier tube relaxation, etc. To correct for the drift, the data were sorted run by run to observe the extent to which the gain shifted. The first run was used as a reference run, two prominent peaks with known energies from ENDSF [Abr10], 167 keV(^{72}As) and 773 keV(^{72}Ge) were fitted to get the centroid. Fig. 4.10 show the residual of the centroid channel relative to the reference peaks. In the $LaBr_3$:Ce detector, typical gain drift at lower energy is about 6 channels and up to 30 channels for the high

energy peak. The lower energies in the LEPS detector shifts by 3 channels and at higher energies the peaks shift by 100 channels.

To correct for the gain drift, a linear gain matching relationship given in Eq. (4.4) was used.

$$f(x) = ax + b, \tag{4.4}$$

where x is the centroid, a and b is the gain and offset respectively. The centroid of the peaks in the non-gain matched reference spectrum was designated as X_1 and X_2 whereas, the centroid of all the other spectra to be corrected were designated as $X_1{}'$ and $X_2{}'$ for the low energy peak (167 keV) and the higher energy peak (773 keV) respectively. The gain was defined to have the relation

$$a = (X_1 - X_2)/(X_1' - X_2'), \tag{4.5}$$

All the other parameters are defined in the text. The offset is given by the expression

$$b = X_2 - (X_1 - X_2)/(X_1' - X_2')\times X_2'. \tag{4.6}$$

After correction, the peaks were all aligned as the difference in the centroid of the reference peak and the gain shifted peak was almost zero as shown in Fig. 4.11.

In order to check for the gain drift in the Si(Li) detector, a time versus energy matrix was used. By setting gates on the time for which each peak was measured, ICE spectra were obtained. The peaks were fitted and the residual of the peaks centroid relative to the reference peaks is shown in Fig. 4.12. As evident from the figure the maximum shift is less than 1 channel for the four peaks, this is considered negligible [OCo94] and thus, it was determined that there was no need for gain correction in the Si(Li) detector.

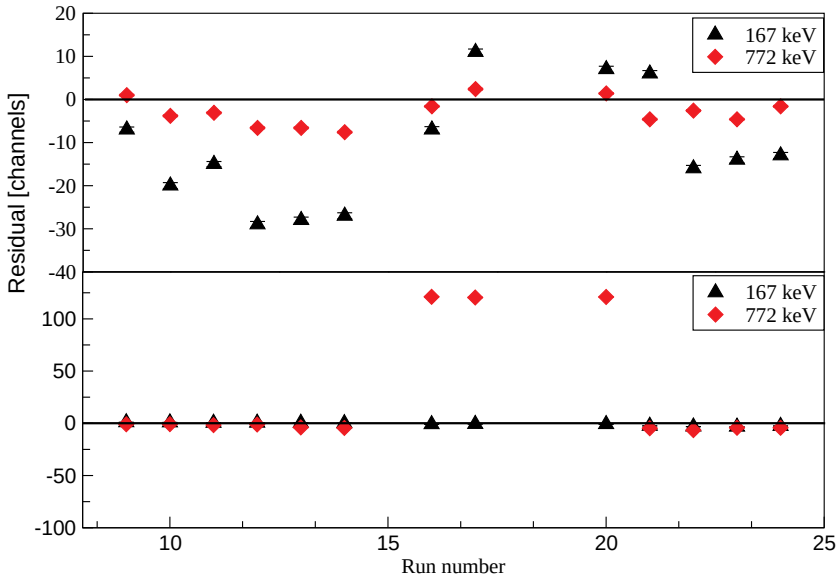

Figure 4.10: Gain drift in one of the $LaBr_3$:Ce (upper) and segment d of the LEPS detector (lower) for the low energy and high energy peaks.

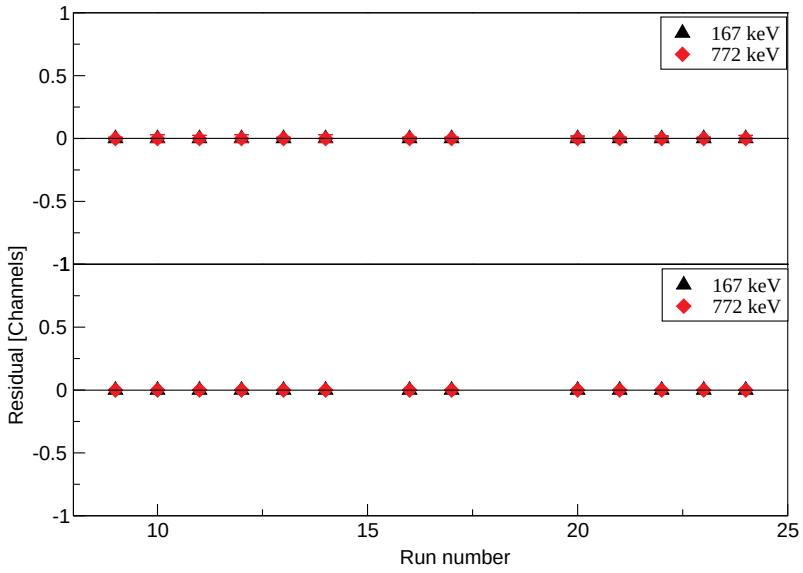

Figure 4.11: Gain drift corrected in one of the $LaBr_3$:Ce (upper) and segment d of the LEPS detector (lower) for the low energy and high energy peaks.

The $LaBr_3$:Ce is made of a PMT which contains a photocathode that geometrically increases the number of electrons when struck by a photon. The interference of

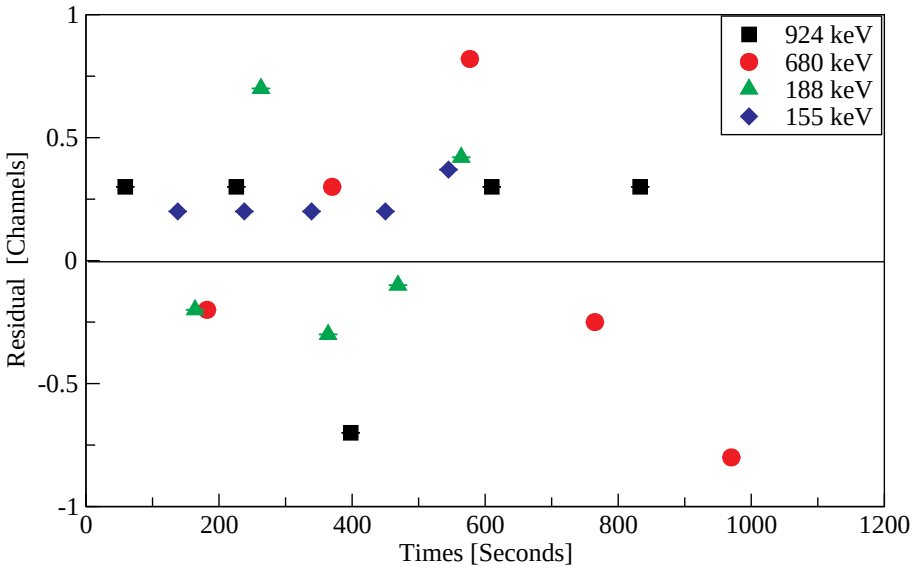

Figure 4.12: Plot of the difference in the centroid of the conversion electron peaks relative to the reference spectrum as a function of time.

any stray magnetic field will cause a loss of a fraction of these electrons and results in a smaller signal being output, proportional to the magnetic field [Sue11,Wan14]. It is important to note here that the maximum stray magnetic field at the target position is approximately 0.01 T (100 Gauss).

To investigate the effect of stray magnetic field on the photoelectrons, the magnetic flux density vs $LaBr_3$:Ce energy matrix from the in-beam data was used. The effect of this interference can be observed by the shift in the gain which increases linearly with magnetic field as shown in the top panel of Fig. 4.13. By projecting on the field, an energy spectrum was obtained and magnetic field were assigned to the most prominent peaks at lower and higher energies based on the $B\rho(E)$. A linear function was obtained from this relation for each detector and used to correct for the gain drift. As shown in the lower panel of Fig. 4.13, the peak positions and width have been reduced by the correction.

Fig. 4.14 shows the gain drifted total projection energy spectrum overlaid with

the gain corrected spectrum. There is an improvement in the shapes of the peaks by the gain correction as shown by the gain corrected spectrum.

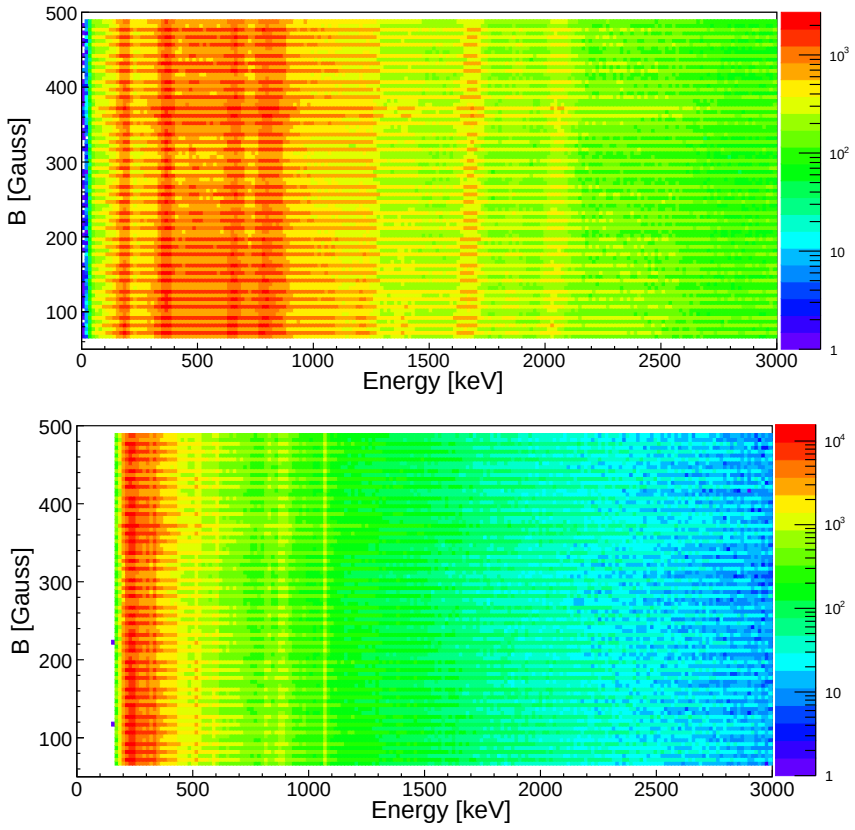

Figure 4.13: Magnetic flux density vs $LaBr_3$:Ce detector 1 energy matrix. Top without gain correction, bottom gain corrected.

4.3.3 K and L separation

Due to the limitation in the resolution of the Si(Li), it was not possible to separate between the K and L shell electrons which are ∼10 keV, ∼12 keV and ∼13 keV apart for ^{72}Ge, ^{72}As and ^{72}Se respectively. However, from knowledge of the theoretical conversion coefficients [Kib08], the intensity of the K conversion electrons are stronger than the L electrons at all energies.

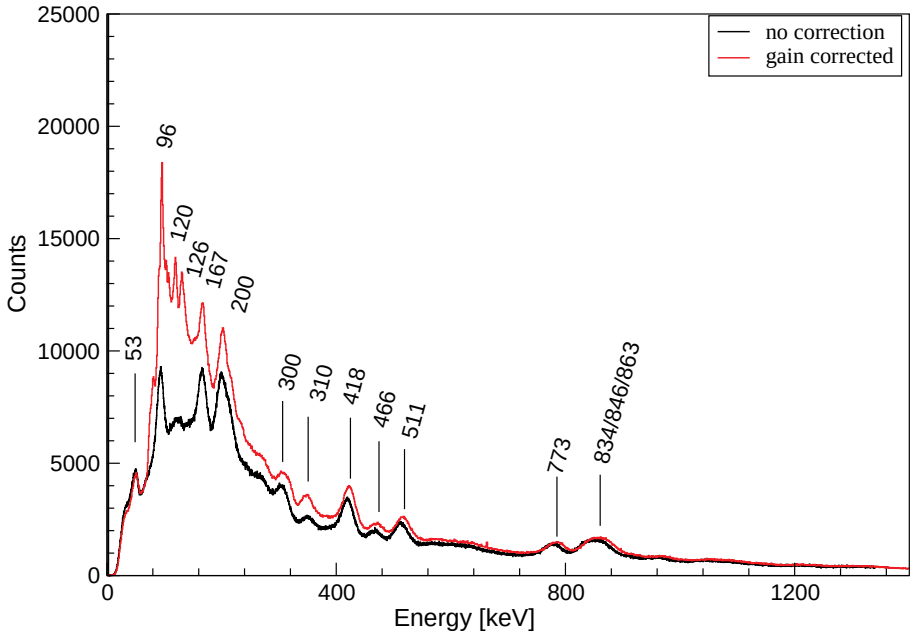

Figure 4.14: A plot showing the gain corrected spectrum from the $LaBr_3$:Ce detectors overlaid with a spectrum with gain drift.

Thus, the centroid was constrained through a χ^2 minimization to fit the overlapping peaks [Evi19]. Considering the peak width fixed with the source data, an additional peak was added in Radware, as shown in Fig. 4.15. The peaks were first fitted as a single peak with a χ^2 of 1.7 and when an additional peak was added, the χ^2 was reduced to 1.5 which support the method used to separate the K from the L electrons. The ratio of K to L from the singles spectrum is therefore determined and compared with previous measurement in Table 4.2.

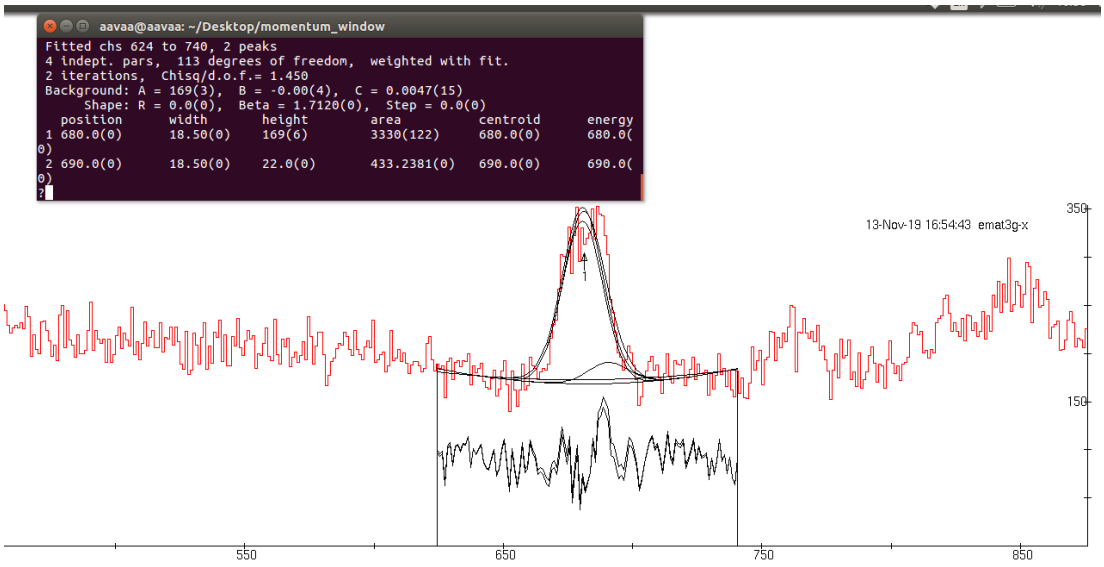

Figure 4.15: A sample spectra of CE showing a fit of the overlapping K and L shell electrons. The χ^2 is about 1.5 as shown in fit parameters.

Table 4.2: The ratio of K to L shell electrons from ^{72}As, ^{72}Ge and ^{72}Se compared with previous measurements from Ref. [Dra74]

Energy (keV)	Isotopes	Transition	This work: K/L	Ref: K/L
96	^{72}As	$4^-_1 \rightarrow 3^+_1$	3.50(40)	-
167	^{72}As	$3^+_1 \rightarrow 1^+_1$	5.00(8)	-
200	^{72}As	$7^-_1 \rightarrow 5^-_1$	3.50(8)	-
300	^{72}As	$6^-_1 \rightarrow 5^-_1$	3.40(21)	-
309	^{72}As	$4^-_1 \rightarrow 2^-_1$	4.60(30)	-
418	^{72}As	$8^+_1 \rightarrow 7^-_1$	5.7(50)	-
691	^{72}Ge	$0^+_2 \rightarrow 0^+_1$	7.6(4)	8.4(6)
773	^{72}Ge	$2^+_2 \rightarrow 0^+_2$	4.30(63)	-
937	^{72}Se	$0^+_2 \rightarrow 0^+_1$	8.1(2)	8.1(3)

4.4 ANU experimental setup

The setup used for the measurement of ^{54}Cr is located at the ANU Heavy Ion Accelerator Facility (HIAF), it consists of a 2.1 T superconducting solenoid which is cooled with liquid helium and an array of 9 mm thick Si(Li) detector called Miel. The Miel detector is segmented into 6 sections with a 3 mm thick non-magnetic shield in front of the detector to avoid crosstalk of electrons or positrons [Tho18]. The axis of the solenoid lies perpendicular to the beam. It is important to mention that the solenoid bore is divided into three sections, the first section is called the short end located 200 mm long from the target, the second section is the target chamber, and third section is the long end which is 400 mm from the target position. The exterior view of the setup and the schematics of the cross sectional view of the solenoid illustrating the short and long ends is shown in Fig. 4.16 and Fig. 4.17, respectively.

An axially symmetric baffle system designed to suppress the background caused by prompt gamma rays, scattered beam, X-rays and low energy electrons traveling along the solenoid axis is mounted inside the long end of the spectrometer. Therefore, the emitted electrons will make 2.5 orbits before landing on the Si(Li) detector placed 350 mm from the target. The spectrometer can be operated in lens mode by sweeping the field to cover a range of energies or at a fixed magnetic field to focus discrete lines. A image of the Super-e showing the baffle system, the Miel array and the particle trajectories is shown in Fig. 4.18. A Hall probe is inserted into the bore while operating the spectrometer in lens mode, about 30 mm from the target. It is mounted in a pipe placed 45 degrees from the bottom plate, where the target system is mounted to ensure that the time spent at each magnetic field setting is consistent.



Figure 4.16: Exterior view of the experimental setup used for the ANU measurements.

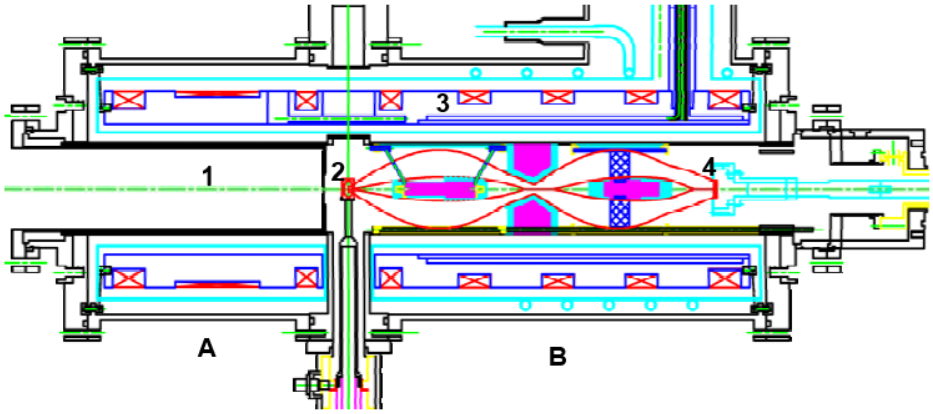

Figure 4.17: A cross sectional view of the solenoid showing the short and long end (A, B) of the coils, 1: beam line, 2: target, 3: coils, 4: detector.

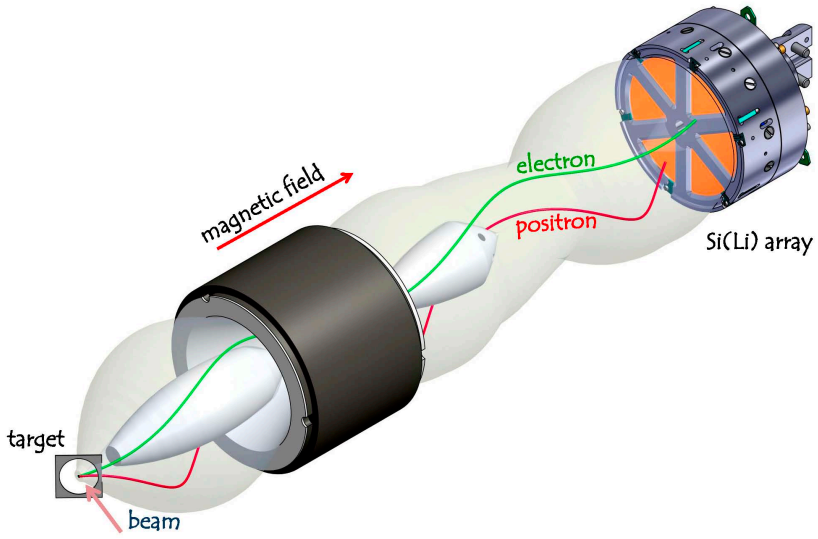

Figure 4.18: Image of the Super-e showing the target, baffles, Miel array, and envelope of trajectories [Kib12].

4.4.1 Experiment using ^{54}Cr target

A 99.2 % enriched ^{54}Cr foil was excited with a 5.4 MeV proton beam delivered by the 14UD tandem accelerator at the ANU. The choice of the beam energy was due to the goal of the experiment which is to populate states upto 3.5 MeV in ^{54}Cr (See Fig. 4.19). The (p, n) channel for ^{54}Mn opens at 2 MeV, therefore, a the beam energy was 3.4 MeV above the threshold, hence, the ^{54}Cr$(p, n)^{54}$Mn channel opens up. Conversion electrons and electron-positron pairs were measured with the Miel detector array. The Miel array along with accompanying electronics has a time resolution of 10 ns for electron-positron coincidence and an energy resolution of 2.5 keV at 1.1 MeV. Gamma rays emitted during the nuclear reaction were measured with two HPGe detectors named Odin and MUX2 placed at 25 cm and 150 cm away from the target, respectively. The HPGe detectors has full-width at half maximum (FWHM) of 2 keV at 1.3 MeV.

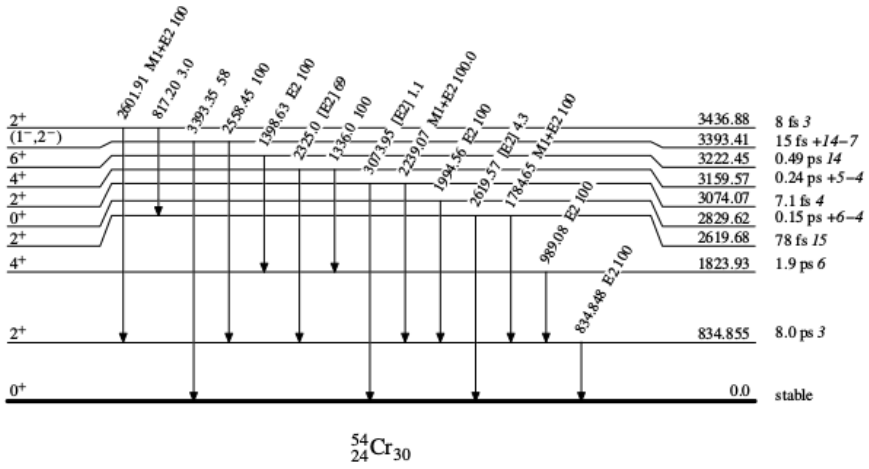

Figure 4.19: Level scheme showing adopted gamma rays for ^{54}Cr [Don14].

For the singles measurements, the field was sampled from a magnet current of 2.744 to 12.677 A for the first 2 runs followed by discrete field of 10.461 A to search for the $E0$ transition in ^{54}Cr. The field values were calculated according to Eq. (3.2) using the field-energy coefficients $C_{lower} = 0.0343$, $C_{lower} = 0.389$, and $C_{lower} = 0.045$ [Kib20]. The decay of excited states with energy above 2 MeV are dominated by IPF. Thus, the field was stepped to be optimum for the 2.443 MeV, 2.618 MeV and 2.848 MeV transitions. The energies of the pairs were measured by the segmented Miel detector and the coincidences were summed up offline using a *Tsort* script [Kib12] to project pair spectra for each field value and the three spectra were compressed and added together. The details of all the runs and experimental conditions are presented chronologically in Table 4.3.

Table 4.3: Summary of runs for ^{54}Cr measurement with Super-e spectrometer at $E_p = 5.4$ MeV.

Runs	Mode	Condition	Current [A]	Cycles
001	singles	beam diagnostics	2.744:12.677	-
002	singles	CE in 0.6:3.0 MeV	2.744:12.677	1.5
003	singles	fixed for 2.83 $E0$	10.416	100
004	pairs swept	for 1.6:5.0 MeV	2.034:7.057	
005	pairs stepped	very low statistics	3.502,3.802,4.21	6
006	pairs stepped	for 2.44, 2.62, 2.85 MeV	3.502,3.802,4.21	132
007	singles	for high statistics	4.83:8.59	13.3

4.4.2 Data acquisition system

The cables from the six segments of the Si(Li) and HPGe detectors carry signals from incident electrons and gamma rays into an Ortec Dual Spectroscopy Amplifiers (SA) and are readout via Analog to Digital Converters (ADCs). Similarly, the time signals from the Si(Li) detector, HPGe detectors and associated suppression shield is sent to a series of Timing Filter Amplifiers (TFA) to amplify and shape the signal, and then to Constant Fraction Discriminators (CFD) to generate the fast logic pulses. These logic signals are combined with the BGO shield to veto the HPGe signal. Information about the time difference between coincident detectors is received by the Multi-Function Display (MFD) and passed to a Time to Digital Converter (TDC) via the Level converter where it is sent into the data stream. The magnetic field for each electron detected is measured with a Hall probe and saved with the data. Also measured alongside with data is the magnetic field control voltage, which is read from the power supply programmer. A block diagram of the data acquisition system is shown in Fig. 4.20.

4.4.3 Detection efficiency of the ANU spectrometer array

In determining the efficiency of the HPGe detectors ^{152}Eu, ^{56}Co sources were used. To determine the Miel efficiency, a 2 mg/cm^2 ^{170}Yb foil was irradiated over a period of 24 hours with 18 MeV proton beam in the irradiation station. The intent was to produce ^{170}Lu with a half-life of 2 days in a (p, n) reaction which decays by emitting gamma rays and ICE up to 3.4 MeV.

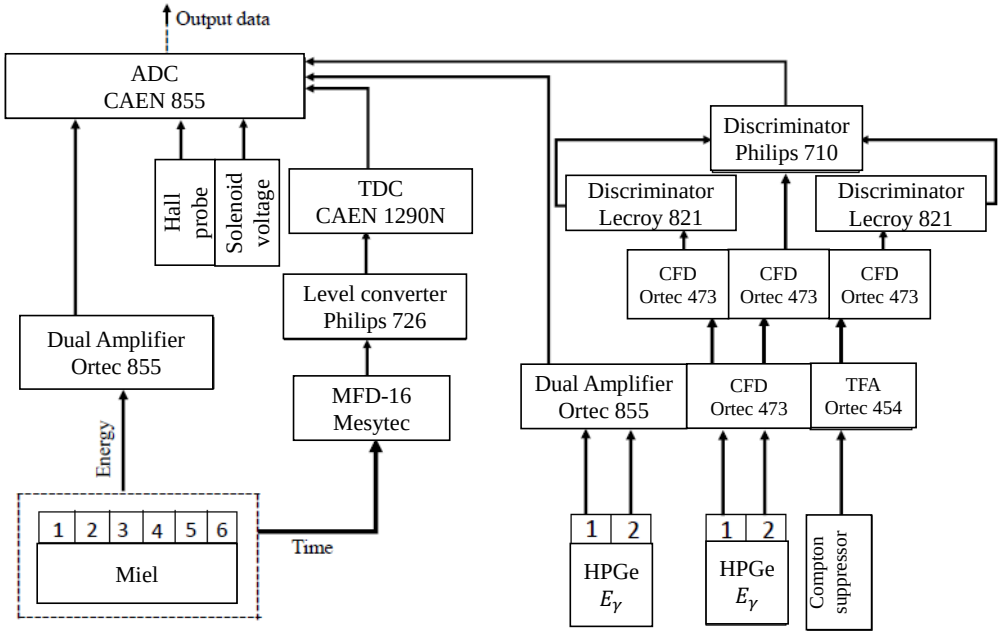

Figure 4.20: A block diagram of electronics used for data acquisition and processing.

4.4.4 HPGe detector efficiency

The activity of the sources were not known, therefore only the relative efficiency of the detector was determined. The relative efficiency for one of the HPGe detectors used in the measurements is shown in Fig. 4.21. There are two data points that were excluded from the fit as an outlier to get a good line of best fit. The gamma

efficiency functional form given in Ref. [Cre15] as

$$eff = EXP[(A + Bx + Cx^2)^{-G} + (D + Ey + Fy^2)^{-G}]^{-1/G}, \tag{4.7}$$

where x = ln(energy/100 keV) and y = ln(energy/1000 keV) while A, B, C, D, E, F, and G are fit parameters, were used to fit the data points.

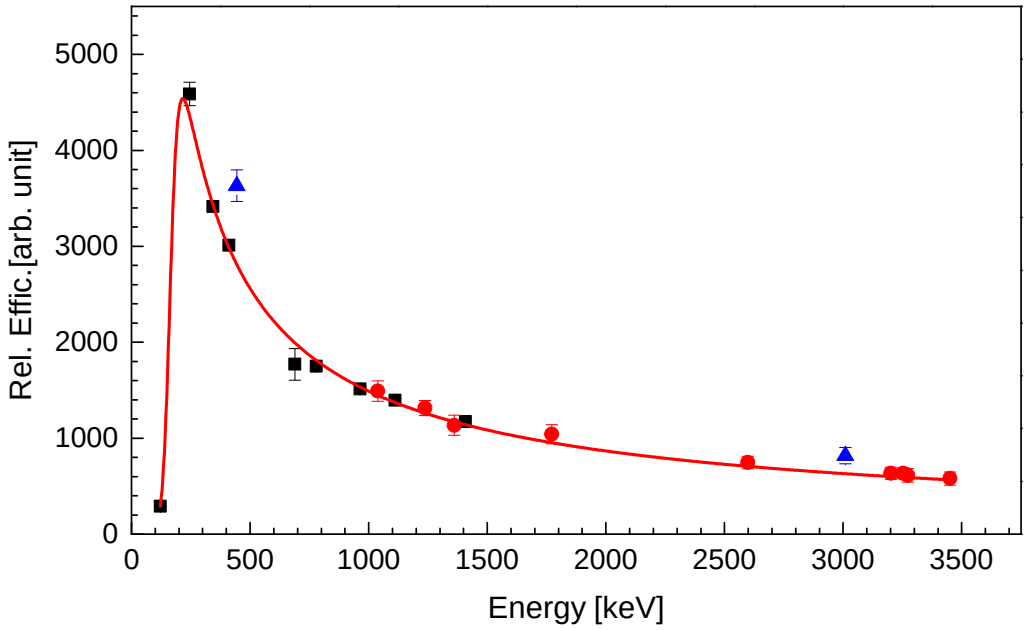

Figure 4.21: Relative efficiency of MUX2 detector, a normalization factor of 8.349 was used to combine the data from ^{152}Eu (black squares) and ^{56}Co (blue circles). The blue triangles are points excluded from the evaluation.

4.4.5 Super-e detection efficiency

The detection efficiency of the spectrometer was calibrated with ^{170}Lu source using relative intensities from Ref. [Bag02]. To normalize the relative efficiency of the lens, the Monte Carlo code [Kib20] was used to simulate the absolute detection efficiency of the Super-e plus Miel set up operated in lens mode using five

million electron trajectories. A magnetic current of range 4.830 A to 8.593 A were used in the calculations to sample electrons from 0.9 to 2.6 MeV energy range. The take-off emission angles of the electrons were constrained between 16° to 47°. The magnet current corresponds to the one used in the actual measurement. The result of the absolute efficiency is shown by the continuous line of Fig. 4.22.

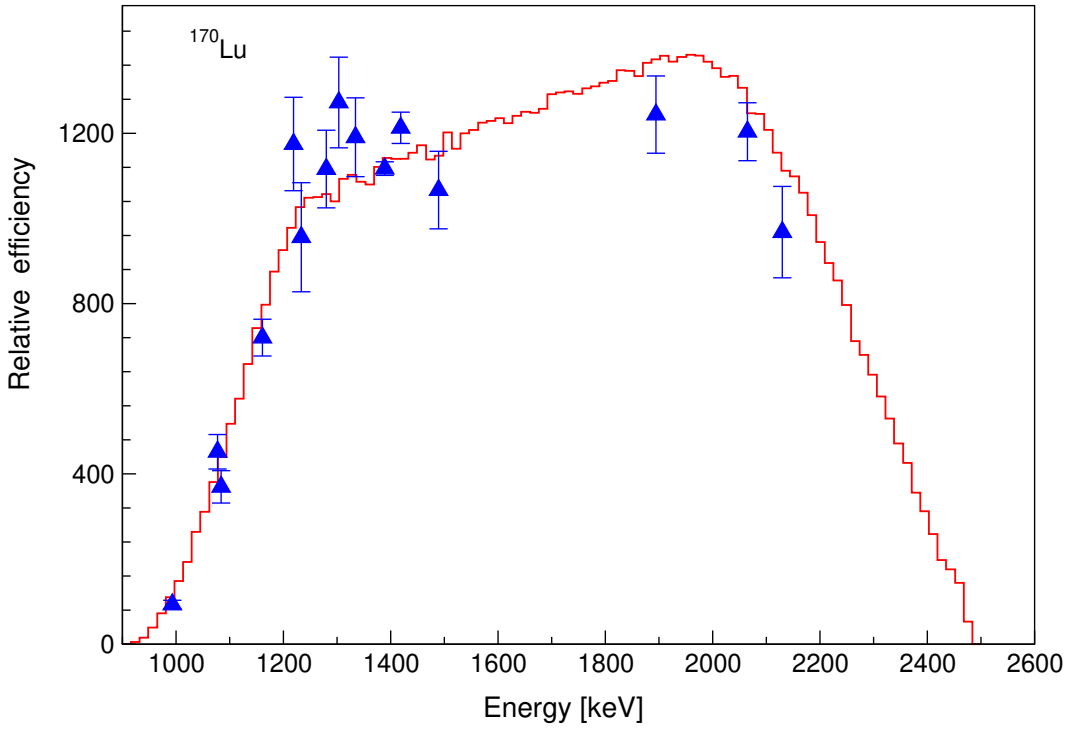

Figure 4.22: Relative efficiency of Super-e spectrometer calculated with Monte Carlo code compared with data point from the ^{170}Lu source.

4.4.6 Simulation of internal pair efficiency

Electron-positron pair energies (E_+, E_-) and individual emission angles (θ, ϕ) were randomly generated isotropically using a distribution described in Ref. [Tho18] in Monte Carlo simulations. The angle of separation (θs) between the electron and positron is obtained from the emission angle, it is used with the electron

energy E_+ to calculate the double differential probability $\mathrm{d}^2P_\pi(E_+,\theta_s)/E_+dE_+d\theta_s$, where P_π is the pair emission probability. To ensure that the emitted events are pairs, a random number is generated from $X \in [0, d^2P_\pi^{max}(E_+,\theta_s)/E_+dE_+d\theta_s]$ and compared with the double differential probability. If the random value exceeds the former value, the events is rejected because no pair is emitted. However, when the random number is less than the differential probability, the events are recorded as pairs. The double differential distributions for the 2.443 MeV ($M1$ and $E2$) transition in ^{54}Mn are presented in Figs. 4.23(a) and 4.23(b), respectively.

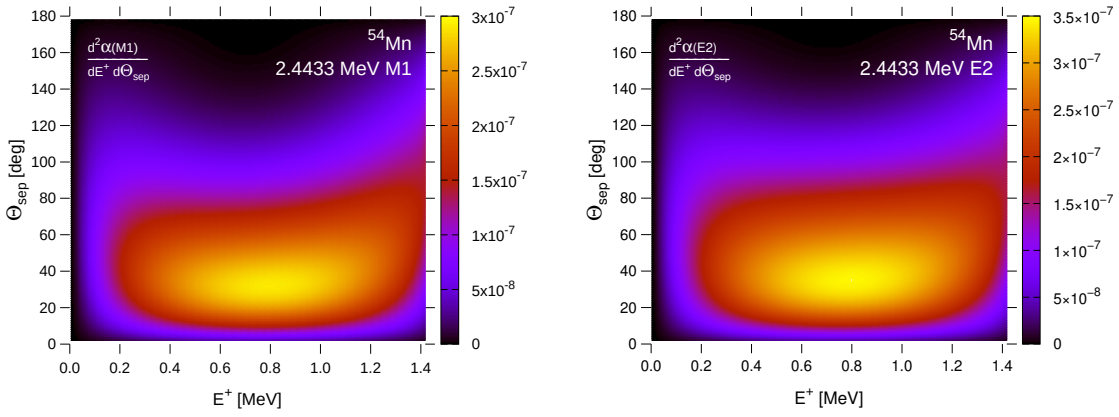

(a) **(b)**

Figure 4.23: The double differential pair emission rate for multipoles in the 2442 keV transition from Lens IPF [Kib20].

The distribution shows that the maximum emission probabilities occur at a separation angles, $\theta_s \sim 30^\circ$ and 40° for $M1$ and $E2$ respectively, when the electron-positron energies are approximately equal.

The internal pair efficiency required to extract the spectroscopic information for transitions of interest in this study is simulated using the Lens IPF Monte Carlo code [Kib20]. The pair efficiency depends on the transition energy and multipolarity, therefore, it was calculated individually for the observed tran-

sitions of interest. A total of one million events were sampled for each energy and a take-off angle range of $15° \leq \alpha \leq 48°$. The detection efficiency was evaluated for every pair, therefore, e^- and e^+ were accepted in the 588 - 833 keV energy range for 2443 keV ($M1 + E2$), 658 - 938 keV for 2618 keV ($M1 + E2$) and 762 - 1064 keV for the 2848 keV ($M1 + E2$) transitions. Table 4.4 shows the numerical values used to deduce the pair efficiencies. The resultant absolute pair efficiency is shown in Fig. 4.24. It should be noted that electrons and positrons share the energy and the results show that the efficiency is optimal, when the energy sharing is equal.

4.5 Data analysis for ^{54}Cr$(p, n)^{54}$Mn reaction

The ^{54}Cr data were sorted using a *Tsort* program. *Tsort* is a script driven program written to sort DCP run files and save the projections into DCP and Radware format 1D and 2D spectrum files. The DCP files are converted to ROOT histogram files for analysis. To correct for gain shift in aligning the six spectra from the Miel detector and the two crystals of HPGe detectors, a PSCALE (a linear scaling function) command is used between run files. This command will apply a linear transformation to the individual modules and ADCs and write the modified channel number out as

$$f(x) = ax + b + c(x)$$

where a and b is the gain and offset respectively, $c(x)$ is random number between -0.5 and +0.5. The addition of a random number to the output channel eliminate the possibility of two or more channels being mapped into the same channel.

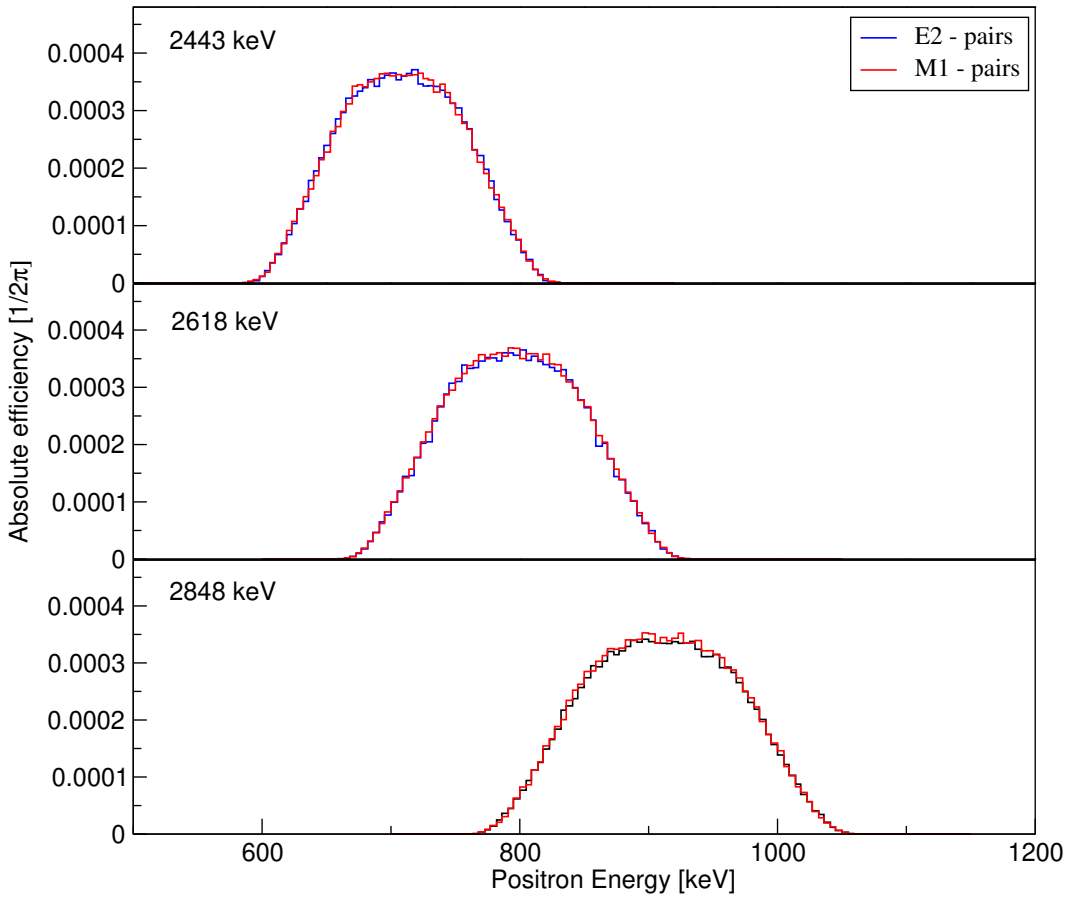

Figure 4.24: Simulated absolute pair efficiency for the individual multipolarities for each transitions of interest using three magnet current settings.

For pairs, three transitions were sampled i.e. 2443.3 keV, 2618.4 keV and 2848.2 keV. The Miel detector was operated in sum-coincidence mode, that is, whenever any two detector fired, the electron-positron energy, time differences and the magnetic field were recorded. To sum the 15 detector combinations (D1-D2, D1-D3 ...D1-D6, D2-D3.....D5-D6) and select true pair events, gates were placed on the Time to Digital Converter time difference coincident peak and the 15 pairs were subsequently added together.

Table 4.4: Numerical values for the simulated pair efficiencies. The uncertainty in the transmission is ∼1 % and ∼5 % for the detection efficiencies.

		e^-		e^+		pairs	
E (keV)	Quantity	$E2$	$M1$	$E2$	$M1$	$E2$	$M1$
2443.3	Trans. particles ($\times 10^4$)	17.12	17.00	17.17	17.14	50.56	50.72
	Transmission ($\times 10^{-3}$)	3.04	3.13	3.05	3.15	8.98	9.33
	Det. efficiency ($\times 10^{-3}$)	2.71	2.80	1.98	2.05	5.22	5.42
2618.4	Trans. particles ($\times 10^4$)	17.47	17.47	17.55	17.55	51.86	52.52
	Transmission ($\times 10^{-3}$)	2.71	2.78	2.72	2.80	8.03	8.35
	Det. efficienc ($\times 10^{-3}$)	2.38	2.45	1.73	1.78	4.53	4.71
2848.2	Trans. particles ($\times 10^4$)	19.59	19.57	19.64	19.70	56.45	57.39
	Transmission ($\times 10^{-3}$)	2.91	2.98	2.92	3.00	8.40	8.74
	Det. efficiency ($\times 10^{-3}$)	2.52	2.58	1.82	1.87	4.56	4.74

By gating on the random time difference region shown in Fig. 4.25, the summed energy spectrum was background subtracted. To adjust for sampling time, the random time difference regions were used to create a scaling factor using

$$Scaling factor = \frac{T_{Pr}}{T_{bgL} + T_{bgR}},$$

where, T_{Pr} is the time of the prompt events, T_{bgL} is the time of the left background and T_{bgL} is the time of the right background. The summed pair spectrum was sorted using momentum-selection and time-coincidence conditions. The strong gamma ray transitions in the three spectra were used to obtain their relative population. To normalize the gamma ray detection efficiency to the pair detection efficiency, the 2443.3 keV transition was used.

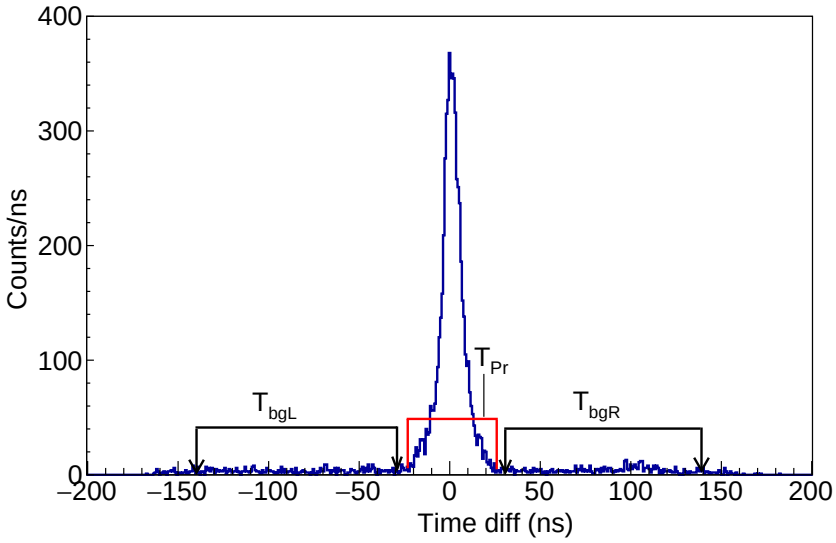

Figure 4.25: Time difference spectrum showing the three TDC regions. T_{bgL} is the background left, T_{bgL} is the background right and T_{Pr} is the prompt region. A factor of 0.1863 is obtained from these limits and used in scaling the pair spectrum according to sampling time.

It should be noted that in the super-e experiments, for every conversion electron or pair event, as well as every gamma ray detected, the corresponding magnetic field is also recorded. The projected magnetic field of the stepped field for pair conversion measurements are shown in Fig. 4.26. Gates were set on those fields to project the gamma rays and the pair spectra collected with the field setting.

4.5.1 Kinematics calculations of ^{54}Cr$(p,n)^{54}$Mn reaction

By using the approach described in Subsection 4.1.2.2, the dynamics of 5.4 MeV protons impinging on a 1.53 mg/cm^2 thick ^{54}Cr target were calculated. The summary of the results are presented in Table. 4.5 which suggest the recoil decays inside the target.

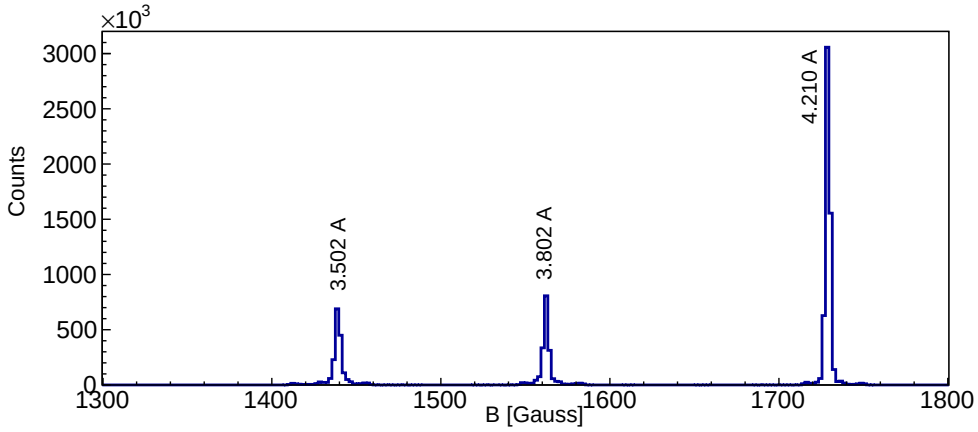

Figure 4.26: Projected magnetic field for pair conversion measurements. The three peaks correspond to the field settings.

Table 4.5: Reactions characteristics of the proton induced reaction on ^{54}Cr target.

Physical properties	**Quantity**
Beam energy [MeV]	5.4
Centre of mass energy [MeV]	
Recoil velocity β (v/c) [%]	1.95
Compound nucleus recoil energy [MeV]	0.98
Target thickness [mg/cm^2]	1.53
Effective target thickness [μm]	3.0
Maximum range of ^{54}Mn [μm]	0.4

Chapter 5

Results and Discussion

In this chapter, the results of experimental measurements at iThemba LABS and ANU are presented. The measured spectra and spectroscopic information such as gamma ray and ICE intensities, conversion coefficients, monopole strength, mean-square charge radius and quadrupole deformation deduced from the alpha-induced reaction measurement is presented and discussed in section 5.1. In section 5.2, the summary of iThemba LABS measurements are given. Similarly, spectroscopic information extracted from proton-induced measurements are discussed and summarized in sections 5.3 and 5.4, respectively. Also, theoretical calculations have been performed to interpret the experimental results and are discussed in section 5.4.

5.1 ^{70}Ge experiment results

The goal of the experiment was to measure conversion coefficients and electric monopole transition strengths $\rho^2(E0)$ in the low-lying transitions from the reaction products involving ^{70}Ge. To achieve this, ICE were measured in coincidence

with gamma rays. A level scheme showing adopted gamma rays for ^{72}Ge, ^{72}As and ^{72}Se taken from [Abr10] are shown in Figs. 5.23, 5.11, 5.24.

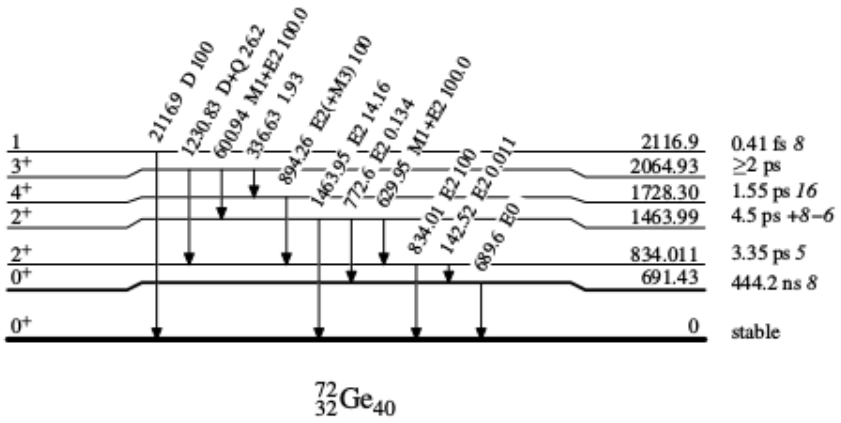

Figure 5.1: Level scheme showing adopted gamma rays for ^{70}Ge taken from [Abr10].

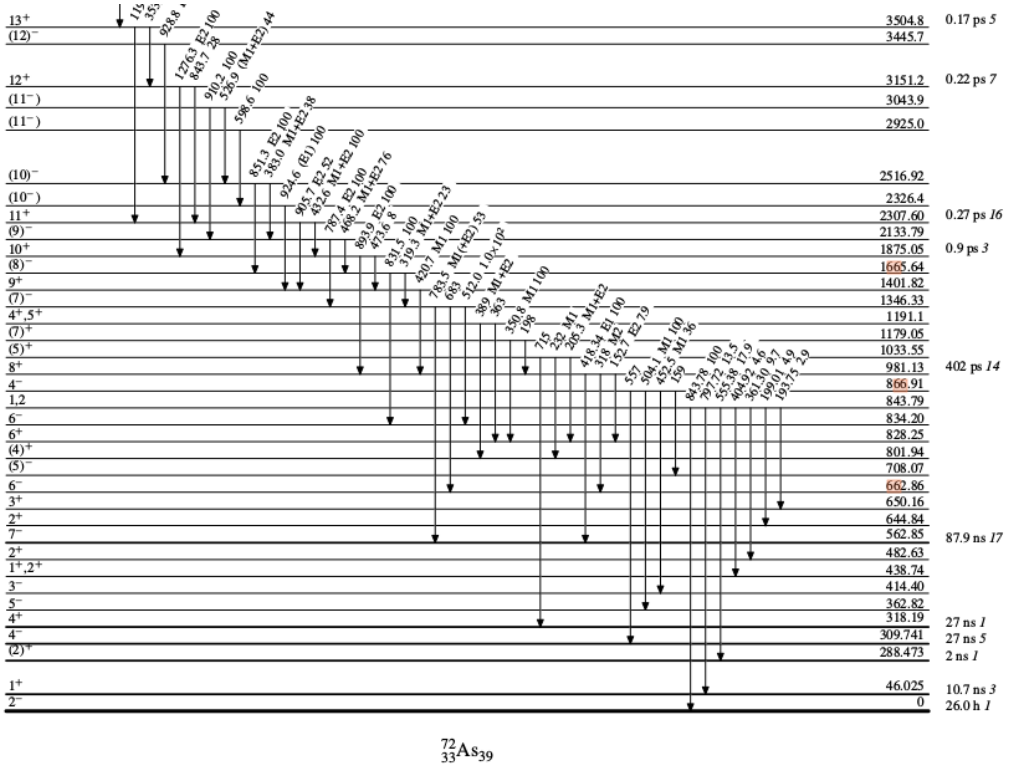

Figure 5.2: Level scheme showing adopted gamma rays for ^{72}As taken from [Abr10].

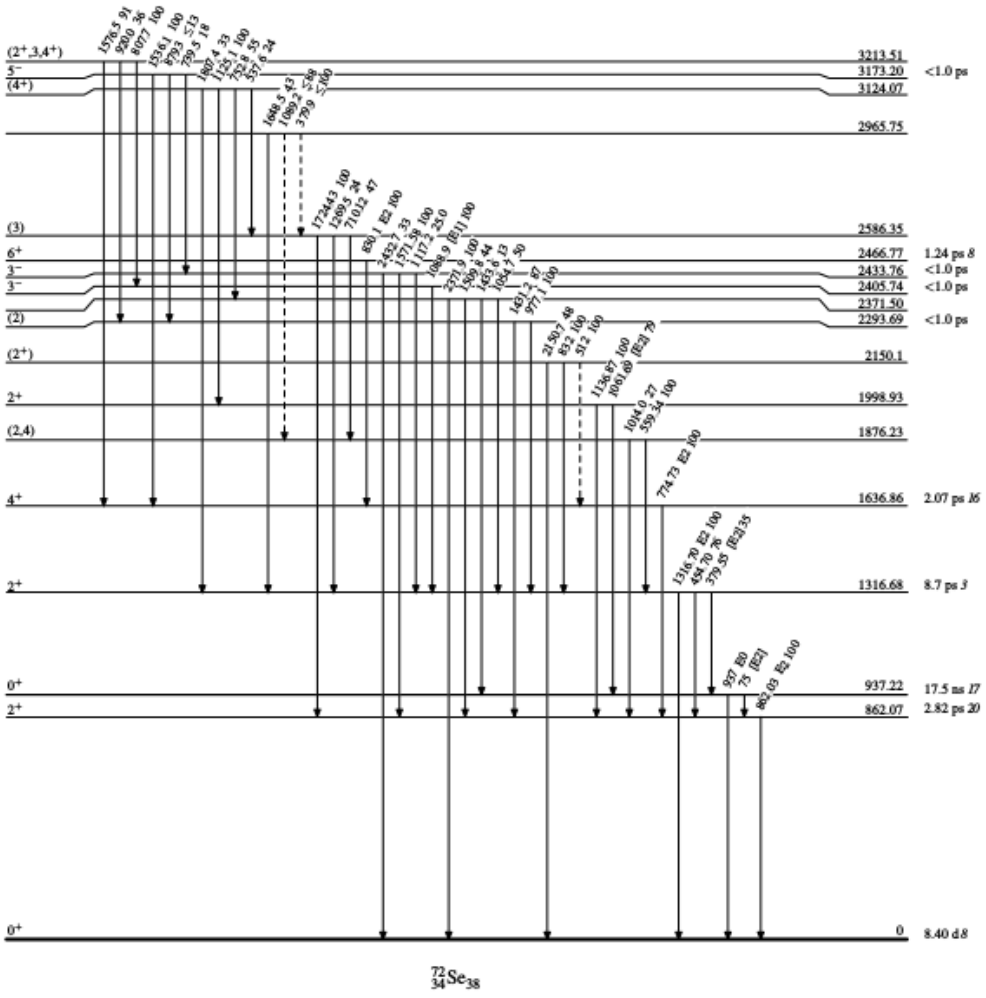

Figure 5.3: Level scheme showing adopted gamma rays for ^{72}Se taken from [Abr10].

The gamma ray singles and momentum window gated conversion electron spectra are shown in Fig. 5.4. A two-dimensional magnetic flux density versus electron energy matrix is displayed in Fig. 5.5 to show the relationship between the detected electrons and magnetic field.

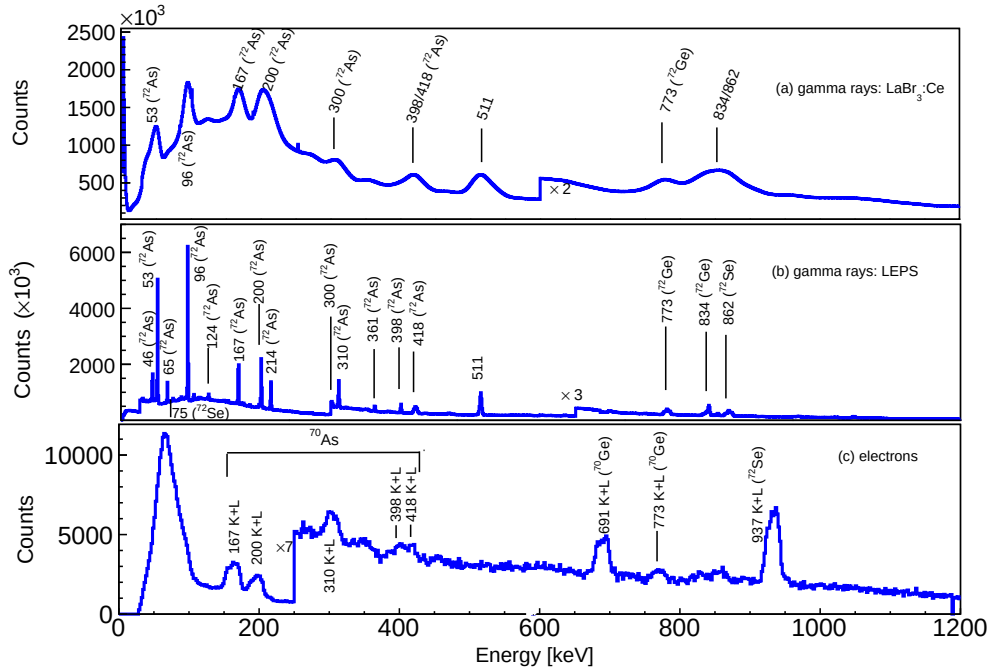

Figure 5.4: Singles spectra. (a) Gamma rays detected with $LaBr_3$:Ce detectors, (b) Gamma rays measured with LEPS detectors, (c) Conversion electrons from the Si(Li) detector gated on the momentum window. The conversion electron peaks are shifted up by the K shell binding energy of ^{72}Ge to align with the transition energy.

The gamma-electron coincident matrix was created using time difference and $B(\rho)$ gating conditions to minimize random coincidences and to accept only conversion electrons emitted within the characteristic limits of the acceptance window. Therefore, the unwanted background is greatly minimized. The matrix showing detected conversion electrons from the Si(Li) detector in coincidence with the measured gamma rays from the six $LaBr_3$:Ce detectors is shown in Fig. 5.6. By placing single gates on the observed transitions in the electron-gamma matrix, the background subtracted spectra shown in Fig. 5.7 and Fig. 5.8 were obtained and used to deduce the experimental ICCs which shall be discussed in the next subsection.

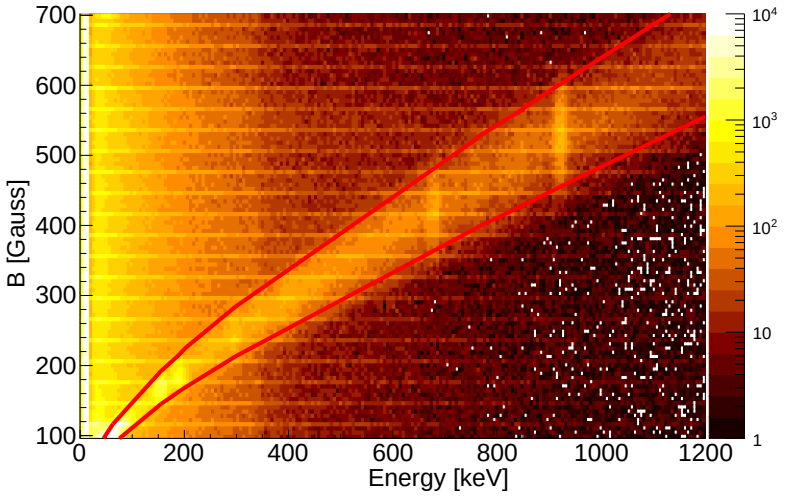

Figure 5.5: Magnetic flux density versus energy matrix from the α-induced reaction. The red lines represent the momentum window calculated using Eqn. (3.2).

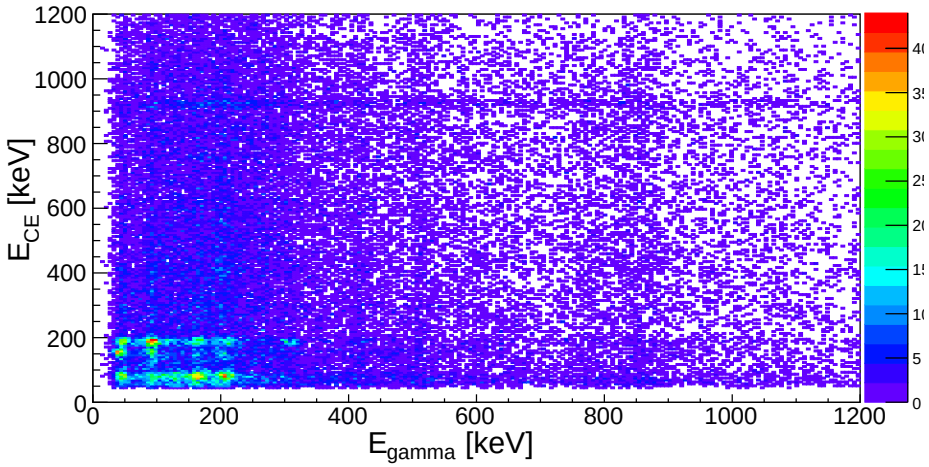

Figure 5.6: A coincident matrix for the $LaBr_3$:Ce versus Si(Li) energies from the ^{70}Ge experiment.

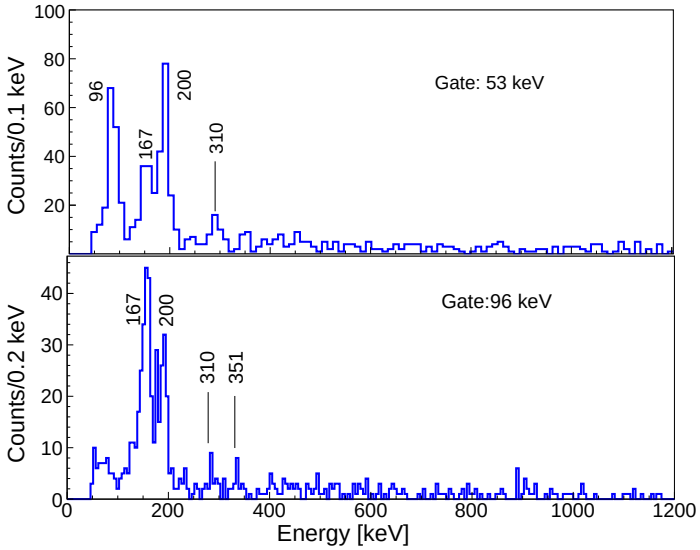

Figure 5.7: Sample of gated background subtracted ICE spectra projected from the e-γ matrix. Upper: gated on 53 keV gamma rays, Lower gated on 96 keV gamma rays.

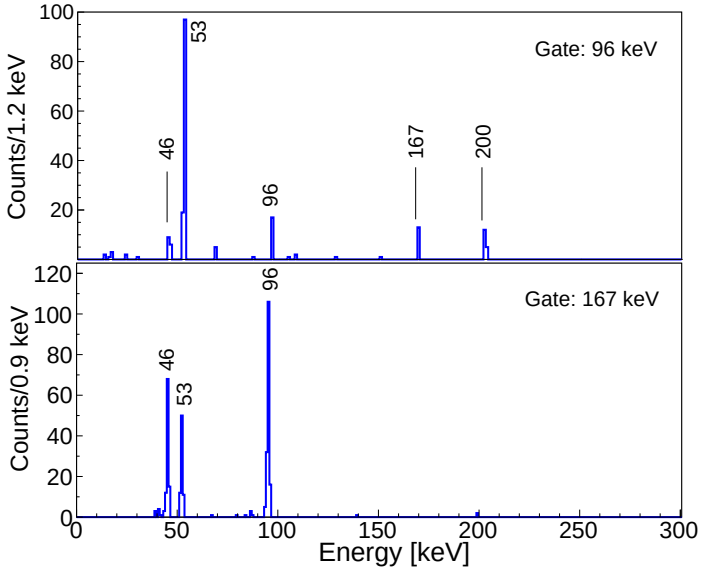

Figure 5.8: Background subtracted γ-ray spectra projected from the e-γ matrix. Gates are placed on $(4_1^- \rightarrow 3_1^+)$ and $(3_1^+ \rightarrow 1_1^+)$ transitions. Upper: gated on 96 keV conversion electron transition, Lower gated on 167 keV conversion electron transition.

5.1.1 Extraction of internal conversion coefficients

The calibration of the spectrometer was performed using ^{133}Ba and ^{207}Bi radiation sources with known activities. Therefore, the experimental conversion coefficient α_K is determined from the measured coincidences using

$$\alpha_{exp} = \frac{N_e \times \epsilon_\gamma}{N_\gamma \times \epsilon_e}, \tag{5.1}$$

where N_e is the number of coincident electrons, N_γ is the number of coincident gamma rays detected and (ϵ_e, ϵ_γ) are the corresponding absolute efficiencies. The peak areas and deduced intensities from the observed transitions are given in Table 5.1.

Table 5.1: Gamma ray and K conversion electron coincident peak areas and intensities.

E_γ (keV)	Transition	N_γ	N_e	I_γ	I_e
^{72}As					
96	$4_1^- \rightarrow 3_1^+$	599(66)	299(22)	12.2(13)	404(30)
167	$3_2^+ \rightarrow 1_1^+$	616(68)	177(19)	18.7(21)	200(22)
200	$7_1^- \rightarrow 5_1^-$	1332(147)	1074(118)	47(5)	1063(117)
300	$6_1^- \rightarrow 5_1^-$	514(57)	62(7)	25(3)	51(6)
310	$4_1^- \rightarrow 2_1^-$	300(34)	113(11)	16.1(10)	93(9)
418	$8_1^+ \rightarrow 7_1^-$	557(61)	28(5)	38(4)	20(4)
^{72}Ge					
691	$0_1^+ \rightarrow 0_1^+$	95(7)	18(6)	1583(126)	1125(90)
773	$2_2^+ \rightarrow 0_1^+$	332(75)	39(20)	41(9)	23(12)
^{72}Se					
937	$0_2^+ \rightarrow 0_1^+$	125(9)	38(4)	2083(177)	57.6(11)

The deduced experimental α_K values are compared with theoretical conversion coefficient from BrIcc [Kib08] in Fig. 5.9. The measured ICC values from this work for 96 keV, 200 keV, 310 keV and 418 keV transitions decaying via pairs of $E1$ and $E2$ are in fair agreement with theoretical values, thus, providing evidence

to strengthen the previously assigned multipolarities and spin-parity values from Ref. [Mar76, Soh99, Abr10]. On the contrary, experimental value of the 167 keV $3_2^+ \rightarrow 1_1^+$ transition is not consistent with theoretical value, thus, suggesting a mixed $M1 + E2$ multipolarity. Further comments will be given in the discussion of the α_L results. The deduced conversion coefficient of the 773 K transition from ^{72}Ge is lagre with respect to the theoretical BrIcc value. However, it is consistent within experimental uncertainties with $E2$ multipolarity. Another enhancement was also observed for 300 K ($6_1^- \rightarrow 5_1^-$) transition in ^{72}As which was assigned a mixed multipolarity ($M1 + E2$) by Ref. [Soh99, Soh97].

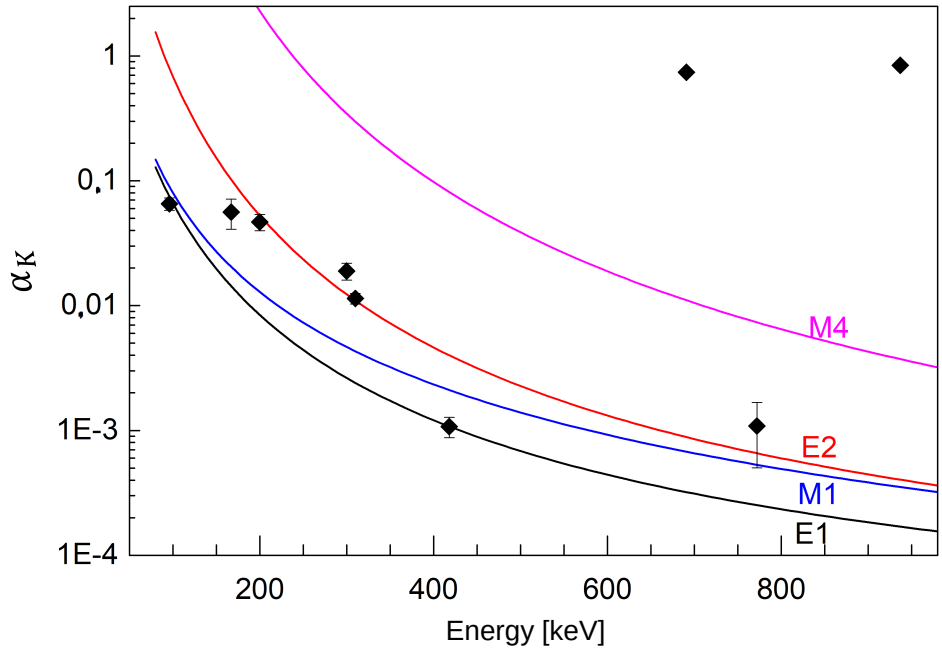

Figure 5.9: Experimental K conversion coefficients (diamond) compared with theoretical values from BrIcc [Kib08] values (smooth lines).

However, this is a $J_i^\pi \neq J_f^\pi$ transition, it is therefore, highly unlikely that the enhancement is due to the presence of an $E0$. Based on the uncertainty limit of 15 % in this measurement, it is sensible to say the transition is more likely to be

an $E2$ transition contrary to the $M1 + E2$ assignment by Ref. [Soh99].

There is no clear evidence of corresponding gamma ray peaks for the 691 keV and 937 keV transitions from the decay of ^{72}Ge and ^{72}Se. Therefore, to extract the ICCs of these transitions, a lower limit of counts was assumed based on the absolute detection efficiency of the detectors. The high ICC values obtained as shown in Fig. 5.9 are significantly higher than $M4$ transitions which shows that such transitions are not possible by gamma decay, therefore, they can be assigned as $E0$ transitions. The adopted multipolarities are summarized in Table. 5.2.

Table 5.2: Adopted multipolarities from [Abr10] and experimental K conversion coefficients, α_K compared with theoretical values from BrIcc for the observed transition in ^{72}As, ^{72}Ge and ^{72}Se.

E (keV)	Transition	Mult.	$\alpha_K \times 10^{-3}$			
			Exp.	$M1$	$E2$	$E1$
^{72}As						
96	$4_1^- \rightarrow 3_1^+$	$E1$	65.4(8)	89.3(13)	794(12)	74.6(11)
167	$3_2^+ \rightarrow 1_1^+$	$E2$	98.8(15)	20.4(3)	102.2(15)	14.39(20)
200	$7_1^- \rightarrow 5_1^-$	$E2$	46.7(7)	12.81(18)	52.6(8)	8.40(12)
300	$6_1^- \rightarrow 5_1^-$	$M1 + E2$	19.0(3)	4.7(7)	12.28(18)	2.6(4)
310	$4_1^- \rightarrow 2_1^-$	$E2$	11.4(1)	4.3(6)	10.95(16)	2.4(4)
418	$8_1^+ \rightarrow 7_1^-$	$E1$	1.08(2)	2.1(3)	4.0(6)	1.10(15)
^{72}Ge						
691	$0_2^+ \rightarrow 0_1^+$	$E0$	740(20)	0.61(9)	0.81(12)	0.29(5)
773	$2_2^+ \rightarrow 0_1^+$	$E2$	1.10(58)	0.48(7)	0.60(9)	0.23(4)
^{72}Se						
937	$0_2^+ \rightarrow 0_1^+$	$E0$	843.3(26)	0.39(6)	0.44(7)	0.18(3)

Similarly, the α_L conversion coefficients were also deduced using L intensities deduced from the assumption of two peaks with fixed width, the results are compared with theoretical values from BrIcc in Fig. 5.10 and Table 5.3. The experimental α_L values of 96 keV, 418 keV and 773 keV transitions differ from the theoretical values. For the 96 keV and 418 keV transitions, the results are contrary to

the $E1$ interpretation previously made in Fig. 5.9. Since parity is not conserved in both transitions, the 96 keV cannot be an $E2$ transition, also, the 418 keV cannot have a $M1$ multipolarity. The difference could be due to over-estimation in the deduced K/L intensities from the fits. Therefore, the assignment of $E1$ multipolarity to these transitions is based on the α_K values. In the case of the 773 keV transition, the difference is ascribed to a systematic error which could be from the efficiency calibration at higher energies. However, the α_L values of the 167 keV and 200 keV transitions are in perfect agreement with the theoretical values, while 300 keV and 310 keV values agree within experimental uncertainties. This further complements the previously assigned multipolarities which are also consistent with the α_K results.

Table 5.3: Experimental L conversion coefficients, α_L compared with theoretical values for the observed transitions in ^{72}As and ^{72}Ge.

E (keV)	Transition	Mult.	$\alpha_L \times 10^{-3}$			
			Exp.	$M1$	$E2$	$E1$
^{72}As						
96	$4_1^- \rightarrow 3_1^+$	$E1$	56(3)	9.70(1)	7.81(1)	107.6(15)
167	$3_2^+ \rightarrow 1_1^+$	$E2$	12(3)	2.18(3)	12.02(17)	1.48(2)
200	$7_1^- \rightarrow 5_1^-$	$E2$	6(2)	1.36(2)	6.0(1)	0.87(1)
300	$6_1^- \rightarrow 5_1^-$	$M1+E2$	3.60(8)	0.49(7)	1.35(2)	0.270(4)
310	$4_1^- \rightarrow 2_1^-$	$E2$	2.6(11)	0.45(1)	1.20(2)	0.250(4)
418	$8_1^+ \rightarrow 7_1^-$	$E1$	0.19(3)	0.20(3)	0.430(6)	0.111(2)
^{72}Ge						
773	$2_2^+ \rightarrow 0_1^+$	$E2$	0.24(1)	0.049(7)	0.062(9)	0.023(4)

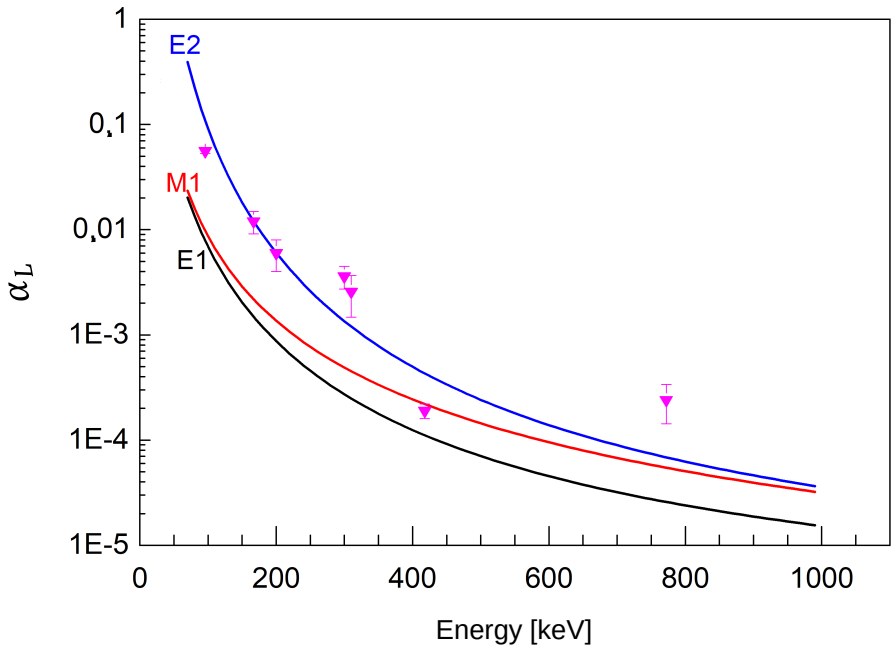

Figure 5.10: Experimental L conversion coefficients, α_L (triangles) compared with theoretical values from BrIcc [Kib08] (smooth lines).

The partial level schemes for the observed transitions in ^{72}As, ^{72}Ge and ^{72}Se nuclei are shown in Figs. 5.11 and 5.12. These were built based on adopted spin-parity and energy levels from [Abr10].

5.1.2 Extraction of $q_K^2(E0/E2)$ and $\rho^2(E0)$ values

The intensity ratio of the electric monopole transitions $E0$ to the electric quadrupole transitions $E2$, $q_K^2(E0/E2)$ introduced by [Chu56] was for $E0$ transitions between 2^+ states, however, it was later observed that the quantity can be extended to cover $E0$ transitions between 0^+ states as well [Ham74, Kib94] and $E2$ transitions from $0_i^+ \rightarrow 2_f^+$. In ^{72}Se, the 937 keV 0^+ state decays to the ground state via an $E0$ transition and to the first excited state through an $E2$ (75 keV) transition.

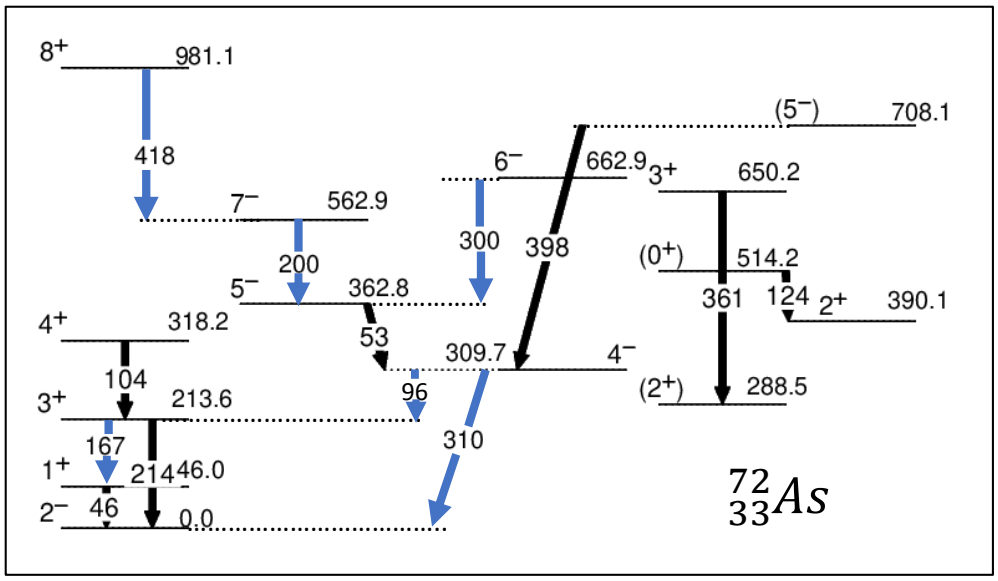

Figure 5.11: Partial level scheme for ^{72}As deduced from e-γ coincidence. Spin-parity assignment and energy levels were adopted from [Abr10]. Blue denotes transitions whose ICC has been measured in this study.

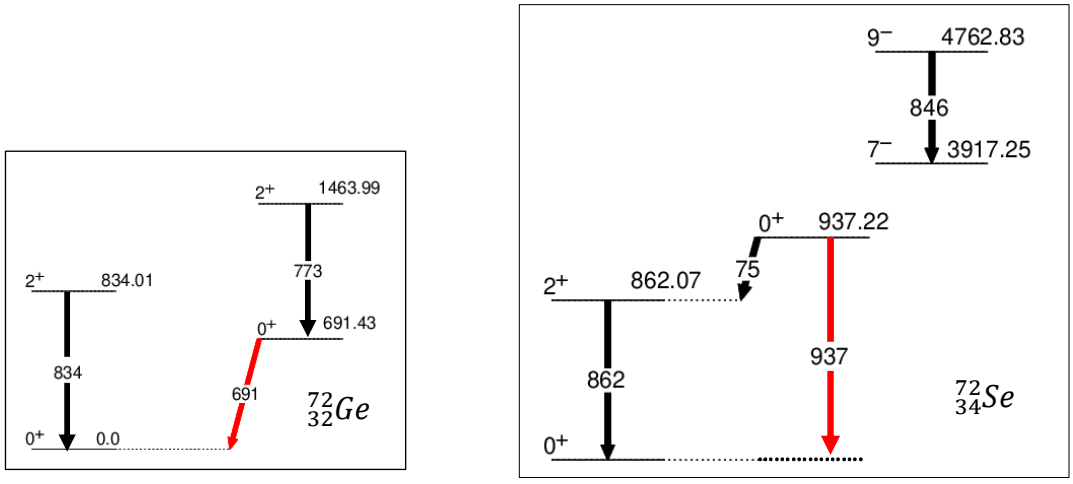

Figure 5.12: Partial level schemes of populated states in ^{72}Ge (left) and ^{72}Se (right). The red denotes $E0$ transitions. Spin-parity assignment and energy levels were adopted from [Abr10].

To deduce the q_K^2 value according to Eq. (2.55), the K conversion electron intensities of the depopulating transitions were determined using the assumption of two peaks with fixed width from the total projection conversion electron spectrum shown in Fig. 5.13.

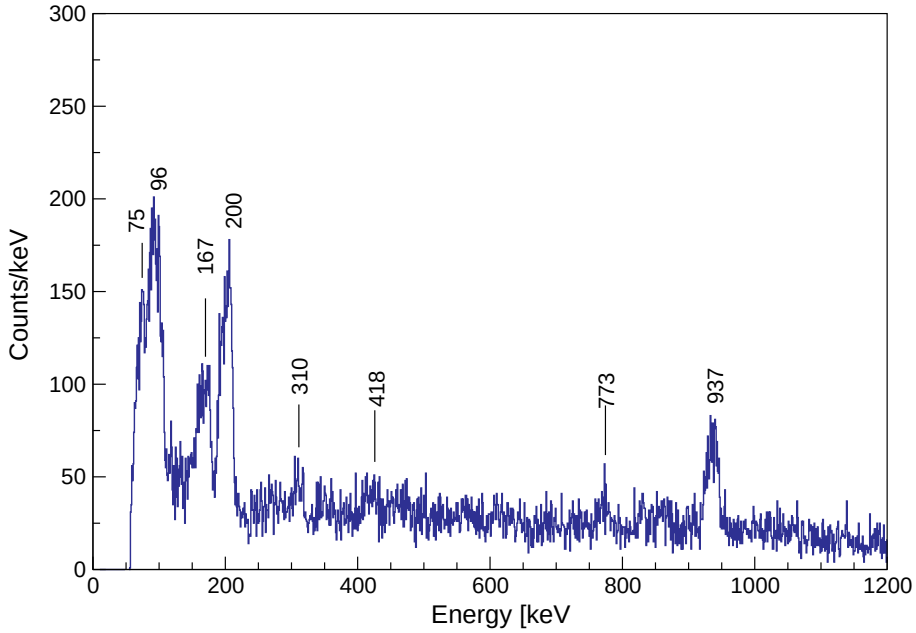

Figure 5.13: Total projection conversion electron coincidences form the ^{70}Ge experiment.

The measured q_K^2 value of 0.47(5) agrees with the previous measurement of [McC11, Cho94, Ram75, Ham74] within the uncertainties. However, it was not possible to determine the q_K^2 value in ^{72}Ge because the $E0$ transition is from the first excited 0^+ state which happens to be the first excited state in the decay scheme as such does not have an $E2$ branch (see Fig. 5.12).

By applying Eq. (5.2), the monopole strength $\rho^2(E0)$ parameter for the pure $E0$ transition observed in ^{72}Se was deduced using the adopted half-life

of 17.5(17) ns [Abr10].

$$\rho^2(E0) = \frac{ln(2)}{\Omega_{tot}(E0) \times (1 + \frac{I_{tot}(E2)}{I_{tot}(E0)}) \times T_{1/2}}, \tag{5.2}$$

where $I_{tot}(E2)$ and $I_{tot}(E0)$ are the total intensities of the $E2$ transition depopulating the 0_2^+ state and monopole transition, respectively. The $\Omega_{tot}(E0)$ is the total electronic factor ($3.78 \times 10^8\ s^{-1}$) taken from Ref. [Kib08]. The results of the measured $\rho^2(E0)$ and q_K^2 together with measured gamma ray and conversion electron intensities are shown in Table 5.4. The obtained $\rho^2(E0)$ is large, although it agrees with previous values of Ref. [Cho94] within uncertainty limits. The magnitude of the $\rho^2(E0)$ suggests there is either a significant deformation/ large charge radius difference or mixing between two states, thus, exhibitive of shape coexistence [Woo99].

5.1.2.1 Extraction of half-life for 691 keV transition

As stated in Section 5.1.2, the 0^+ state in ^{72}Ge cannot decay to the 2^+ state, hence its q_K^2 value could not be measured. However, the $\rho^2(E0)$ value can be calculated if a new half-life of the $E0$ transition is measured. The half-life of the 691 keV transition this has been evaluated to be 444.2(8) ns from ENDSF [Bra84]. The $E0$ is directly populated by the 142 keV transition from the 834 keV 2^+ state with a half-life of 3.35 ps and 773 keV from 1464 keV 2^+ state whose half-life has been evaluated to be 4.5 ps from ENDSF. A time difference spectrum between the $LaBr_3$:Ce detector and the Si(Li) detector is shown in Fig. 5.14. The time difference is asymmetric with a tail on the right, indicative of slower electrons.

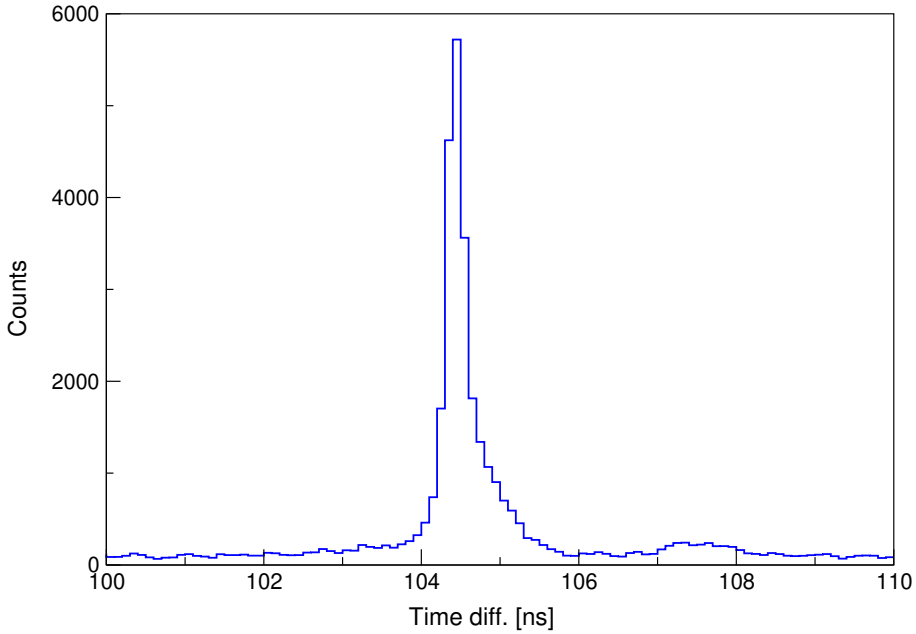

Figure 5.14: The time difference spectrum between a $LaBr_3$:Ce and the Si(Li) detector corresponding to all the events.

By setting a gate on the 773 keV transition which is in coincidence with the 691 K conversion electrons, it is expected that the 691 K should be seen. However, there was no observable peak as seen from the gated spectrum in Fig. 5.15. This could be explained partly from the kinematic calculations. The recoil is formed in the target, then moves away 50 mm from the target position where the electrons enter the spectrometer. With a recoil velocity of ∼0.7 % c which is equivalent to 0.2 cm/ns, most electrons will be emitted outside the acceptance of the spectrometer. Lack of statistics is another reason why the transition was not observed. Therefore, to measure these transitions, one needs a thick target (e.g., 1 mg/cm^2) to stop the recoils and data should be collected for a longer period to acquire more statistics.

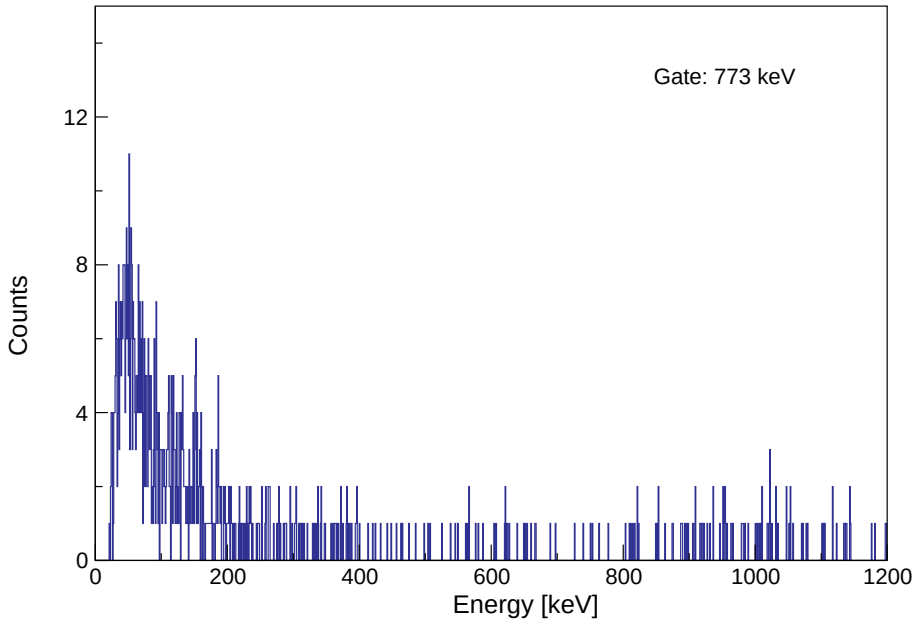

Figure 5.15: ICE spectra projected from the e-γ matrix. Gate is on the 773 keV gamma ray.

The $\rho^2(E0)$ of ^{72}Ge was however calculated according to Eq. (2.53) using the adopted half-life from ENDSF. The theoretical value is compared with literature value in

5.1.3 Extraction of the difference in $\langle r^2 \rangle$ and $\langle \beta_2 \rangle$ in ^{72}Se

The monopole strength $\rho^2(E0)$ can be utilized to determine the change in the mean-square charge radius $\langle r^2 \rangle$ and the difference in the quadrupole deformation parameter $\langle \beta_2 \rangle$ due to its connection with the charge radii and quadrupole deformation as shown in Subsection 2.4.1.

Thus, the experimental value of $\rho^2(E0)$ is used in the following relation

$$\rho^2\left(E0\right) = \frac{Z^2}{R^4} \times a^2(1-a^2) \times (\langle r_1 \rangle^2 - \langle r_2 \rangle^2)^2, \tag{5.3}$$

to obtain the $\Delta \langle r^2 \rangle$ value, where a is the mixing amplitude which is given a

Table 5.4: Measured intensities, the ratio $q_K^2(E0/E2)$ and the $E0$ strength for ^{72}Ge and ^{72}Se compared with literature values.

Isotopes	Quantity	Value	Reference
^{72}Ge (690 E0)	I_{CE}	3400(67)	Exp.
	$\rho^2(E0)$	9.2(2)	Evaluated
		9.18(2)	[McC11]
^{72}Se (75 E2)	I_γ	122.5(14)	Exp.
^{72}Se (937 E0)	I_{CE}	57.6(11)	Exp.
	$q_K^2\ (E0/E2)$	0.47(5)	Exp.
		0.41(8)	[McC11]
		0.6(4)	[Cho94]
		0.37(23)	[Ham74, Ram75]
	$\rho^2(E0)$	33.3(85)	Exp.
		29(18)	[McC11]

.

maximum value of $\frac{1}{\sqrt{2}}$ in this study. The other parameters have been defined in subsection 2.4.1. The change in the deformation parameter $\Delta\langle\beta_2\rangle$ is determined according to Eq. (2.69). The change in the mean-square charge radius for the 937 keV state from ^{72}Se is 2.22(57) fm^2, while the deformation parameter obtained from the $\rho^2(E0{:}\ 4_1^- \rightarrow 3_1^+)$ value is 0.212(54) assuming a spherical ground state (0_1^+). The $\Delta\langle\beta_2\rangle$ value in this measurement agrees with the previous result of 0.207(12) [Ram87], though the uncertainties in this measurement is five times larger, which is due to low statistics. The enhanced $\Delta\langle r^2\rangle$ and the $\Delta\langle\beta_2\rangle$ values calculated using maximum mixing amplitudes suggests a strong mixing and a slight deformation between the 0_1^+ state and the excited 0_2^+ state.

5.1.4 Extraction of $B(E0)$ in ^{72}Se

The reduced monopole $E0$ transition probability calculated from the monopole strength $\rho^2(E0)$ according to Eq. (2.48) yield a $B(E0)$ value of 116(30) W.u. There is no previous information on the $B(E0)$ value of ^{72}Se to compare the

result in this study with. However, the interpretation of the large $B(E0)$ value is that the ground state and the first excited 0^+ state are strong mixtures of components with different $\langle r^2 \rangle$.

5.2 Summary of ^{70}Ge(α,X)Y results

The first in-beam experiment proved successful. The initial intent was to measure the $E0$ transitions in ^{70}Ge through a scattering reaction. However, other reaction channels opened during the experiment hindered the observation of the states of interest. Nevertheless, the results from the experiment proved that coincident measurement with the spectrometer is possible with reasonably high efficiency in the higher energy regime, which is comparable to other spectrometers like the Super-e at ANU [Kib90]. ICCs from the observed transitions in ^{72}As and ^{72}Ge were deduced. The results were consistent with theoretical values, except in the case of a few transitions. The adopted low-lying multipolarities based on the measured ICC values were also largely in agreement with previous assignment. Other spectroscopic information such as, the $E0/E2$ branching ratio, monopole strength, $\rho^2(E0)$ of the electromagnetic transitions, $\langle r^2 \rangle$, $\langle \beta_2 \rangle$ were consistent with previous measurements. Consequently, it is observed from the measured properties of the $E0$ transition in ^{72}Se, calculated in the maximal mixing limit that there is a strong mixing and slight shape changes between the ground state and the first excited 0^+. It is worth mentioning that a paper for the results presented in this thesis has been published in Nuclear Instrument and Methods A [Ava20].

5.3 ^{54}Cr experiments results

The singles gamma ray, ICE and the IPF spectra of the observed transitions from the ^{54}Cr$(p,n)^{54}$Mn reaction are presented in Fig. 5.16. The magnetic flux density versus ICE energy matrix showing the relationship between the magnetic field and the energy of the detected electrons for ^{54}Mn are shown in Fig. 5.18. For clarity, only the transitions with corresponding conversion electrons or pair are labelled, the rest of the observed transitions are listed in Table 5.5. However, since there are no observable conversion or pair electrons corresponding to these gamma ray transitions, they could not be investigated further.

Table 5.5: List of gamma rays observed but not labelled in Fig. 5.16

Energy (keV)	Energy (keV)
1697.3(3)	2198.9(2)
1705.4(1)	2213.1(3)
1932.7(1)	2236.7(3)
2047.2(2)	2267.4(2)
2054.9(2)	2291.3 (5)
2106.9(1)	2354.2(1)
2148.6(1)	2673.7 (2)

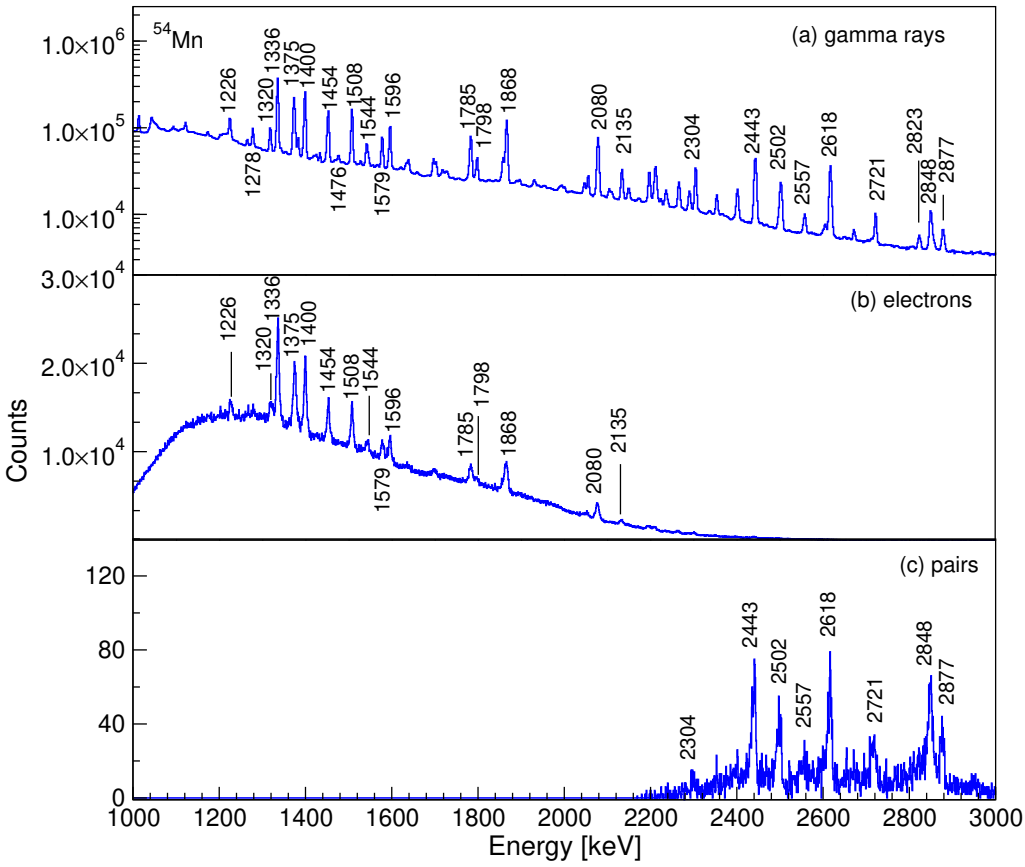

Figure 5.16: (a) Singles γ-ray and (b) conversion-electron spectra measured simultaneously with swept magnetic field. The peaks are shifted by the binding energy of the K conversion electrons to align with (a). (c) Pair sum spectrum measured with stepped field and is shifted up in energy by $2m_0c^2$ to reflect the transition energy. The data are presented from 1000 keV to 3000 keV since no transitions with corresponding conversion electrons or pairs were detected outside of this range, and for clarity, some gamma ray transitions were not labelled.

5.3.1 Extraction of spectroscopic information in ^{54}Mn

To deduce spectroscopic information from the experiment, the first step was to establish firmly which nucleus the observed transitions are from because there transitions with similar energies in ^{54}Mn and ^{54}Cr, this can be observed in Figs. 4.19, 5.17. The ratios of all the strong depopulating transition intensities were evaluated using the deduced peak areas and efficiency. There are transitions with

$\sim$ 1785 keV in both nuclei, however, the intensity ratio of the 1784.6 keV to 2619.7 keV in ENDSF [Don14] for ^{54}Cr is 20:1, which did not agree with the intensity ratio of 1.4:1 measured in this experiment which shows that the 2619.7 keV 2^+ state in ^{54}Cr was not observed.

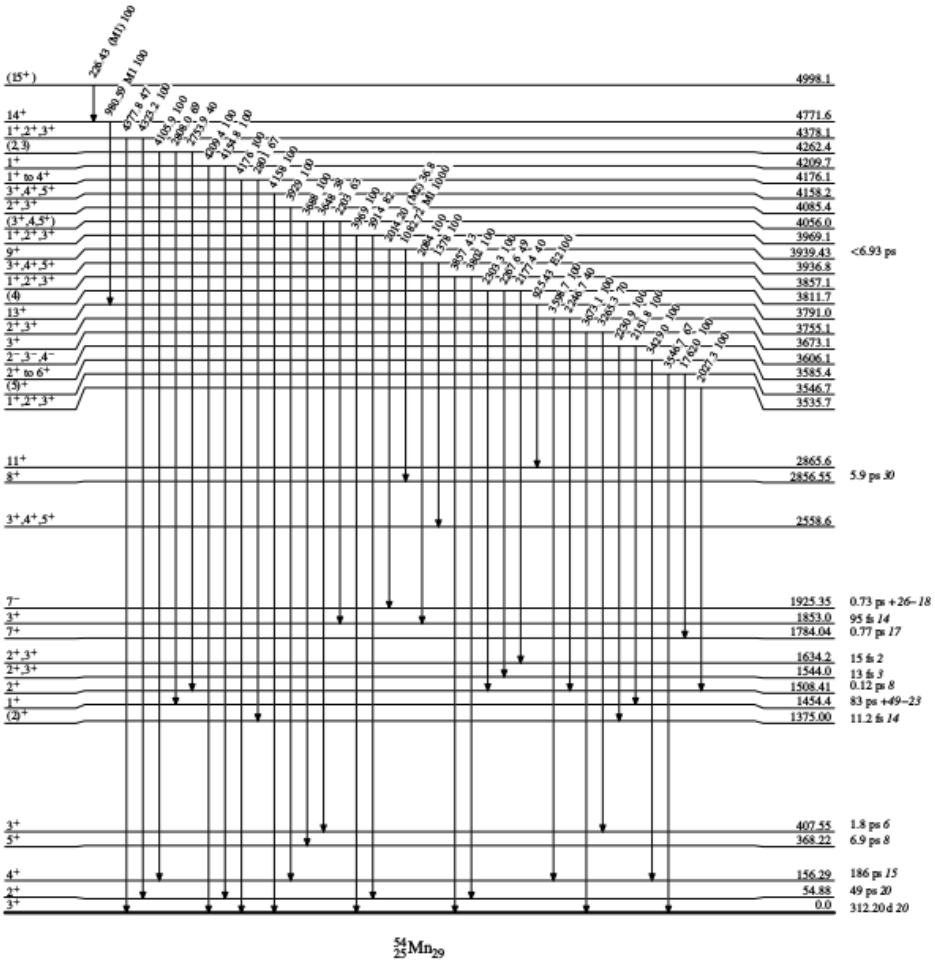

Figure 5.17: Level scheme showing adopted gamma rays for ^{54}Mn [Don14].

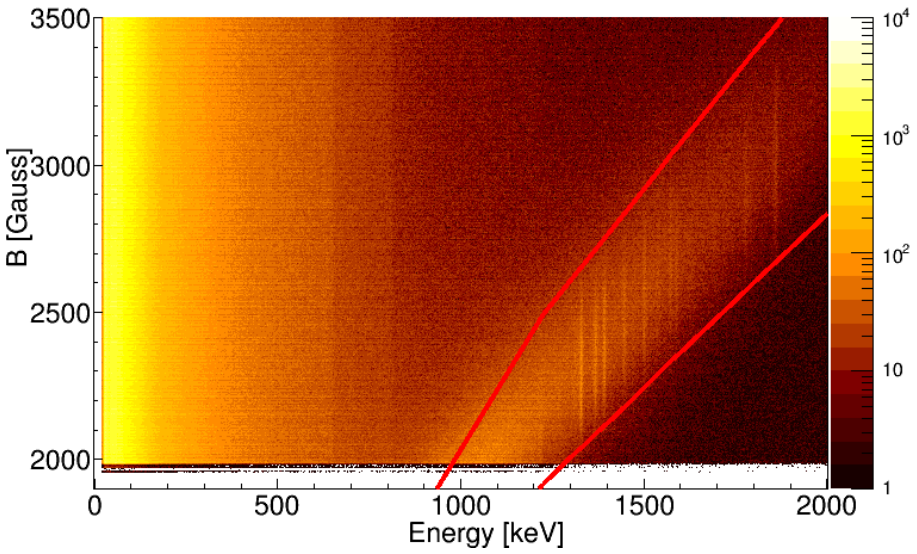

Figure 5.18: The magnetic flux density vs energy matrix. The solid lines represent the momentum window calculated according to Eq. (3.2) using the energy-field relationship coefficiencts for Super-e [Kib20].

Moreover, by comparing the measured intensity ratio of 1784.8 keV and 1730.0 keV transitions from the 1784.5 keV (1^+) state in ^{54}Mn, there was a good agreement, indicating that the 1784.8 keV transition observed is from ^{54}Mn. The possibility of this state overlapping with the 1783.4 keV transition state from 2856.6 keV (8^+) state is ruled out as the beam energy is not enough to excite high spin states. Therefore, with the above evidence, it is sufficient to say that the observed 1784.5 keV is a pure $E2$ ($1^+_4 \rightarrow 3^+_1$) transition from 1784.5 keV (1^+) state. Consequently, the 1784.8 keV was used to normalize the ICE and gamma-ray intensities. Another transition with the same energy in both nuclei is the 1336.0 keV. In ^{54}Mn it is a single transition from the 1391.0 keV (1^+) state while in ^{54}Cr, the 1336 keV and 2325 keV transitions are depopulating the 3159.6 keV (4^+) state with an intensity ratio of 1.4:1 [Don14]. Since, there is no observable peak at 2335 keV, it was concluded that the observed 1336 keV transition is from ^{54}Mn.

There are other depopulating transitions in ^{54}Mn with energies less than 1 keV

apart as observed in 5.17, which may overlap with transitions of interest. For example, there is a 1454 keV transition depopulating the 1454.4 keV (1^+) state and 1453.7 keV from the 1508.4 keV (2^+) state. To resolve this, the ratio of measured intensities of the depopulating transitions were compared with ENDSF values. For instance, the branching ratio of the 1375.1 keV transition from the 1375.0 keV (2^+) state is not consistent with the measured intensity when compared with 1320.2 keV transition from the same state. This could be due to overlap with the 1376.9 keV transition from 1784.5 keV (1^+) state. Also, the ratio of measured intensities of the 1454.0 keV and 1399.9 keV from the 1454.4 keV (1^+) state was not in agreement with the branching ratios from [Don14]. This could be due to contamination with the 1453.7 keV from the 1508.4 keV (2^+) state. Similarly, the intensity ratio of the transitions depopulating the 2136.1 keV (1^+) state i.e. 2080.4 keV and 2136.9 keV was not consistent with deduced intensities, it is likely that the 2080.4 keV is overlapping with the 2079.1 keV transition from the 2133.9 keV (1^+) state. Therefore, these transitions were not considered in the ICC analysis despite being excited.

5.3.2 Internal conversion coefficients (α_K)

The ICC values for ^{54}Mn were determined through the so-called Normalized to Peak Gamma (NPG) method [Sai98] because only singles gamma ray and ICE were detected. The method involves the use of relative efficiencies (ϵ_γ, ϵ_{CE}) for detected gamma rays and conversion electrons respectively and a normalization factor, which is determined using theoretical conversion coefficient of a reference transition. It is customary to use the strongest pure $E2$ transitions as a reference transition where the intensity of other gamma rays can be determined relative

to it. When precision measurements are required, especially in a case where the multipolarity is well established [Sai98], the NPG method is preferred to the method used in Section 5.1.1. Another reason why the method is attractive is that it requires only singles measurement [Ham65]. The method is parameterized as

$$\alpha_K = N \times (\frac{A_{CE}}{\epsilon_{CE}} \times \frac{\epsilon_\gamma}{A_\gamma}), \tag{5.4}$$

where N is the normalization factor determined using theoretical known conversion coefficient of a pure $E2$ transition, A_{CE} and A_γ are the peak areas of ICE and gamma ray, respectively. Therefore, the 1784.8 keV ($1_4^+ \rightarrow 3_1^+$) transition was used to obtain the normalization factor. The measured intensities for the observed transitions in ^{54}Mn, adopted multipolarities and the deduced experimental ICC with theoretical values are presented in Table 5.6. The measured values are compared with theoretical values from BrIcc in Fig. 5.19.

It can be observed from the results that the experimental ICC for 1266 keV transition is between $M1$ and $E2$ which suggest a mixed $M1 + E2$ multipolarity. It is worth mentioning here that the multipolarity of this transition has not been measured before. The 1320 keV $(2)_2^+ \rightarrow 2_1^+$ transitions depopulating the 1375.0 keV (2^+) state indicate enhanced ICC value. An enhancement in the ICC value suggests the presence of an $E0$ component, therefore, this transition will be examined for $E0$ strength. The ICC values for the 1336.0 keV and 1544 keV transitions are located slightly above the theoretical $E2$ value with their uncertainties extending over the $E2$ line. Therefore, these transitions were assigned as $E2(+M1)$ multipolarity taking the uncertainties into consideration. In previous measurements the 1366 keV transitions was assigned as mixed $M1 + E2$ multipolarity [Don14] but the 1544 keV has not been assigned before.

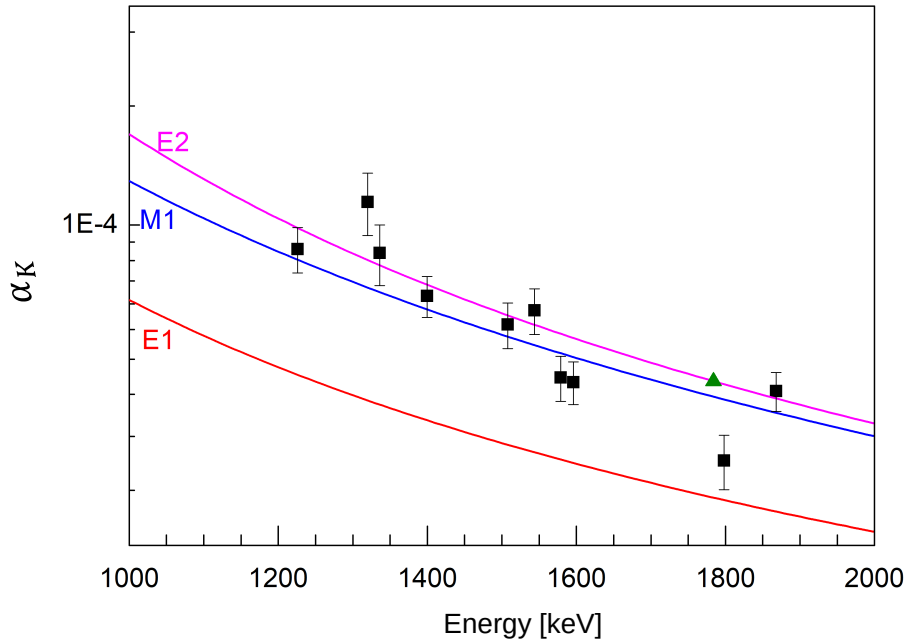

Figure 5.19: Experimental K conversion coeffcients compared with BrIcc values. The green triangle denotes the normalization transition.

Furthermore, the measured ICCs of 1399.6 keV from the 1454.4 keV (1^+) state and 1508.3 keV transitions from the 1508.4 keV excited state supports the assignment of $M1+E2$ on this transition as reported in Ref. [Don14]. Thus, the multipolarity can be unambiguously assigned. Other transitions whose multipolarities until now were unknown are 1579.4 keV, 1596.2 keV, 1798.4 keV, and 1867.8 keV. The experimental ICC provides evidence to assign $M1$ multipolarity to the 1579.4 keV, 1596.2 keV and 1798.4 keV transitions. It could be argued that the 1798.4 keV from the 1853.0 keV (3_5^+) state is more like an $E1$ transition due to its location, but the parity is well known, therefore, based on parity change restrictions this argument is rejected. On the other hand, the 1867.8 keV was assigned a mixed $E2(+M1)$ multipolarity within the uncertainty limit.

Table 5.6: Adopted multipolarities, measured intensities and conversion coefficients compared with theoretical coefficients for ^{54}Mn nucleus.

					$\alpha_K \times 10^{-5}$		
E (keV)	Transition	Mult.	I_γ	I_{ce}	This work	$M1^c$	$E2^c$
1226.4	$2_4^+ \rightarrow 3_2^+$	$M1+E2$ [a]	73(4)	33.3(24)	8.9(10)	8.39(12)	9.85(13)
1320.3	$(2)_2^+ \rightarrow 2_1^+$	$E0+M1+E2$	70(4)	40(5)	11.2(17)	7.30(11)	8.38(12)
1336.0	$1_1^+ \rightarrow 2_1^+$	$M1+E2$	425(39)	189(10)	8.7(13)	7.14(10)	8.17(12)
1399.9	$1_2^+ \rightarrow 2_1^+$	$M1+E2$ [b]	338(17)	122(6)	7.0(7)	6.54(10)	7.40(11)
1508.3	$2_2^+ \rightarrow 3_1^+$	$M1+E2$ [b]	205(14)	63.7(33)	6.1(7)	5.70(8)	6.35(9)
1544.0	$2,3^+ \rightarrow 3_1^+$	$E2(+M1)$ [a]	52(3)	17.4(12)	6.5(7)	5.47(8)	6.05(9)
1579.4	$2,3^+ \rightarrow 2_1^+$	$M1$ [a]	77(4)	18.3(12)	4.6(5)	5.25(8)	5.78(8)
1596.2	$1_3^+ \rightarrow 2_1^+$	$M1$ [a]	123(6)	28.6(17)	4.5(5)	5.15(8)	5.67(8)
1784.8	$1_4^+ \rightarrow 3_1^+$	$E2$ *	134.5(67)	31.5(17)	=4.56	4.22(6)	4.56(7)
1798.4	$3_5^+ \rightarrow 2_1^+$	$M1$ [a]	81(7)	13(1)	3.1(4)	4.16(6)	4.49(7)
1868.8	$1_5^+ \rightarrow 2_1^+$	$E2(+M1)$ [a]	215(11)	47.9(27)	4.3(4)	3.89(6)	4.18(6)

(a) newly assigned, (b) tentatively assigned in Ref. ([Don14]), (*) normalization transition, (c) theoretical ICC [Kib08].

In order to evaluate the component of the $E0$'s in the mixed transitions, the ratio of the experimental ICC for the K shell electrons to the theoretical values from BrIcc [Kib08] were used. For mixed transitions, the K mixed ICCs were used and the excess above unity as shown in Fig. 5.20 was taken to be the enhancement factor. The $E2$ transition in good agreement with theoretical value lies directly on the line of unity.

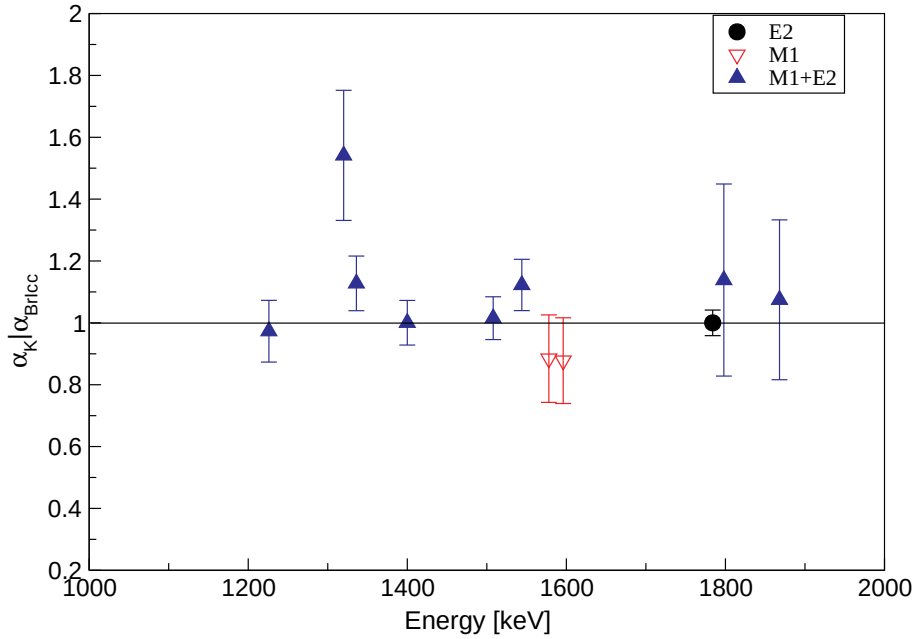

Figure 5.20: The ratio of experimental K conversion and pair coefficients to theoretical values for the transitions of interest in ^{54}Mn. The $E2$ shown here is the normalization transition

5.3.3 Internal pair coefficient (α_π)

The pair conversion coefficients were determined according to Eq. (5.5) with a different normalization factor obtained using the 2443.3 keV transition. It is important to note that the multipolarity of the transition is not known but the spin and parity has been established by previous studies [Don14]. Therefore, an $M1$

multipolarity was assumed since it is a $1^+ \rightarrow 2^+$ transition and from the selection rules, it is obvious that the lowest multipolarity dominate the decays [Reg03]. For the 2672.9 keV state that feeds the 2_1^+ level by emitting a single photon of 2618 keV, the spin is unknown, but a positive parity was assigned previously [Don14]. From the measured pair coeffcients which suggest an $M1$ multipolarity, it is probable that the state may have a spin of unity. The spin and parity of the 2903.1 keV (1^+) state is well established, however, the multipolarity of the 2848.4 keV transitions have not been reported before. The result from the the measured pair coefficient suggests it is a magnetic dipole transition, therefore the multipolarity of $M1$ was unambiguously assigned in this study.

Table 5.7: Adopted multipolarities, intensities and internal pair coefficients (α_π) compared with theoretical coefficients from BrIcc.

E (keV)	Transition	Mult.	I_γ	$I_\pi \times 10^5$	$\alpha_\pi \times 10^{-4}$		
					Exp.	$M1^b$	$E2^b$
2443.3	$1_9^+ \rightarrow 2_1^+$	$M1$ [a]	4.1(2)	5.6(7)	=4.43	4.43(7)	5.29(8)
2618.4	$?^+ \rightarrow 3_2^+$	$M1$ [a]	3.39(15)	5.1(8)	5.08(8)	5.19(8)	6.11(9)
2848.4	$1_{10}^+ \rightarrow 2_1^+$	$M1$ [a]	3.0(2)	5.2(8)	5.86(6)	6.16(9)	7.15(10)

(a) new assigned multipolarity, (b) theoretical values from BrIcc [Kib08]

5.3.4 Partial decay scheme for ^{54}Mn

The experimental ICCs were used as a tool to unambiguously assign multipolarities to the observed transitions. Based on the measured ICC, spin of states that were tentatively assigned previously, were confirmed. Where uncertainties still exist, the assignment was based on the enhanced factor of the multipolarity relative to unity. The partial decay scheme for adopted multipolarities is presented in Fig.

5.21. The decay scheme is built based on the observed gamma ray transitions and the adopted multipolarities.

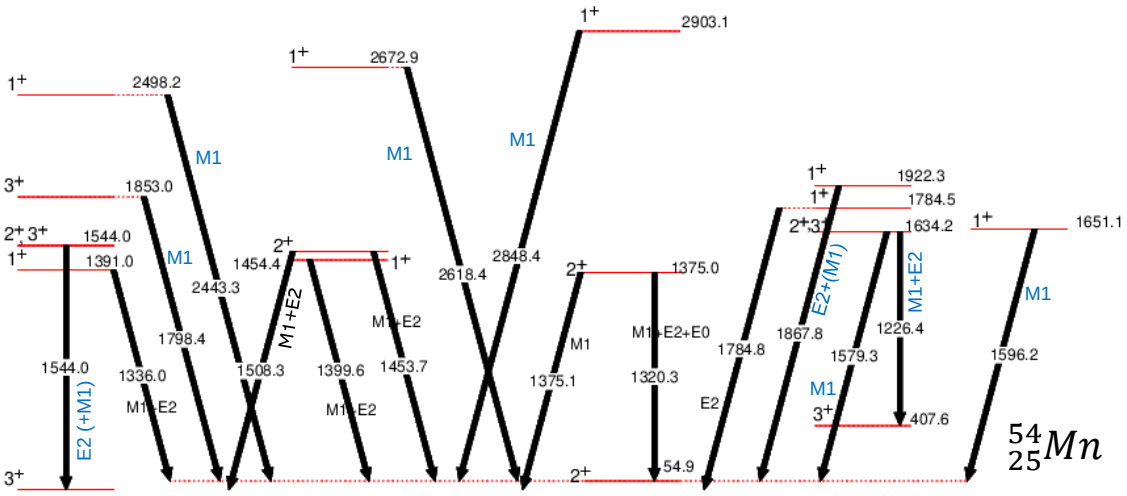

Figure 5.21: Partial decay scheme of ^{54}Mn from the (p,n) reaction showing excitation energies up to 2.9 MeV. In addition, the γ-ray energies and multipolarities are given. Blue denotes the new assigned multipolarities.

5.3.5 Mixing ratio $\delta(E2/M1)$

The BrIccMixing v.2.3 [Kib11] program, developed to calculate multipole mixing ratios and normalization factors for conversion electrons based on a Chi-square Fitting (CFIT) program [Rys80], was used to calculate the multipole mixing ratios using the experimental ICC. The results of the mixing ratios for the newly assigned multipolarities in this measurement are shown in Table 5.8. It should be noted that only the absolute values of the mixing ratios are quoted as the mixing ratio deduced through ICC, is not sensitive to the sign of δ^2 [Rez17]. The large mixing ratio reported for some transitions means, the negative uncertainties overlaps with zero [Kib08]. A plot of the χ^2 fitting for 1226 keV, is shown in Fig. 5.22.

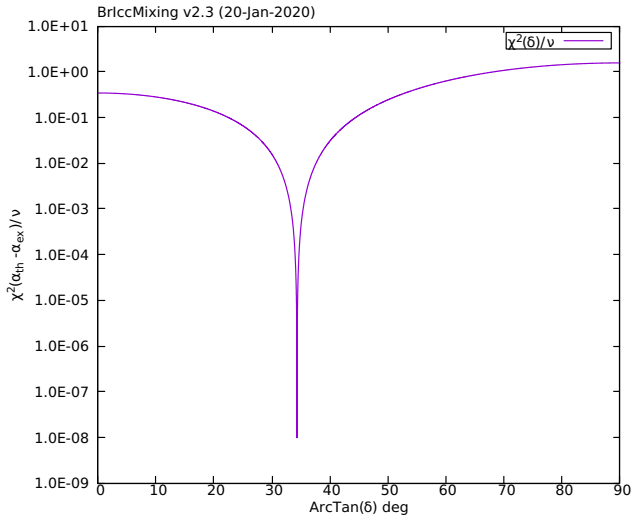

Figure 5.22: A plot of χ^2 for the 1226 keV transition as a function of arctan(δ).

5.3.6 The $q_K^2(E0/E2)$ and $\rho^2(E0)$ values for ^{54}Mn

The 1320.3 keV transition is suggested to display an $E0$ component due to its large ICC value. Therefore, the intensity ratio between $E0$ and $E2$ was deduced by substituting for both, the experimental and theoretical conversion coefficient into

$$q_K^2(E0/E2) = \frac{\alpha_K^{exp}(1+\delta^2(E2/M1)-\alpha_K(M1))}{\delta^2(E2/M1)\alpha_K(E2)} - 1 \qquad (5.5)$$

where $\delta^2(E2/M1)$ is the mixing ratio taken from ENDSF [Don14]. Following the deduction of the $q_K^2(E0/E2)$ value, the strength of the $E0$ transition $\rho^2(E0)$ for the $J^\pi \rightarrow J^\pi$ transition, where $J \neq 0$ was evaluated according Eq. (2.56) using the transition rate deduced from the level half-life of 11.2(14) fs. It is important to note that Ω_K values in BrIcc are given for only even Z nuclei [Kib08], therefore, the values for odd Z nuclei are usually interpolated from the neighbouring even Z nuclei. In the case of ^{54}Mn, with 25 protons, the $\Omega_K(Z,k)$ values of ^{54}Cr and

^{54}Fe were calculated, and the mean value of 8.13(41) s^{-1}, was used. A q_K^2 value of $3.3^{+2.5}_{-1.7}$ and a $\rho^2(E0) \times 10^3$ value of 626^{+142}_{-115} were obtained for the $2_2^+ \rightarrow 2_1^+$ transition depopulating the 1375. keV 2^+ state. The $\rho^2(E0)$ value in this study is large and comparable with the 860(76) and 470(190) value obtained for ^{54}Fe [Tho18] and ^{54}Cr [Dow20] from a similar $2_2^+ \rightarrow 2_1^+$ transitions. The large $E0$ strength is a fingerprint for shape coexistence and strong mixing between two states, therefore, it can be inferred that shape coexistence exist in the odd-odd ^{54}Mn. Although more precise measurements are required to conclude.

Table 5.8: Summary of adopted multipolarities, deduced mixing ratios for the observed transitions, the, intensity ratio and monopole strength $\rho^2(E0)$. Uncertainty within 1 σ were not quoted.

E (keV)	multipolarity	$\delta(E2/M1)$	q_K^2	$\rho^2(E0) \times 10^3$
1226.4	$M1+E2$	$0.68^{+37(a)}_{-32}$	-	-
1320.3	$E0+M1+E2$	$0.4^{+3(b)}_{-2}$	$3.3^{+2.5}_{-1.7}$	643^{+142}_{-115}
1336.0	$E2(+M1)$	-0.85(45)$^{(b)}$	-	-
1544.0	$E2(+M1)$	<1.7E+3$^{(a)}$	-	-
1798.4	$M1$	<1.7E+3$^{(a)}$	-	-
1867.8	$E2(+M1)$	<1.3E+3$^{(a)}$	-	-

(a) reported for the first time, (b) taken from Ref. [Don14]

5.3.7 Summary of ^{54}Mn data

The low-lying states in ^{54}Mn were populated through a (p,n) reaction using the Super-e setup at the ANU. The ICC (α_K) of the $J^\pi \rightarrow J^\pi$ transitions were extracted for the first time in 10 transitions. With the experimental ICC values, it was possible to unambiguously assign multipolarities to nine transitions that were

not assigned before. An $E0$ component was observed in a $2_2^+ \rightarrow 2_1^+$ transition for the first time in this nucleus.

5.4 Theoretical calculations

The nuclear properties of the low-lying excited states in ^{72}Ge and ^{54}Mn are studied within the Five-dimensional collective Hamiltonian based on the covariant density functional theory (5DCH-CDFT) and the Shell model approach, respectively. The results for the calculations are presented in Subsections 5.4.1 and 5.4.2 respectively.

5.4.1 Collective Hamiltonian calculations

The structure of the lowest excited states in ^{72}Ge and ^{72}Se were investigated by diagonalizing the five-dimensional collective Bohr Hamiltonian (5DCH) [Nik08] described in Section 2.2.5. The mass parameter B_0 have been fitted to reproduce the energy of the lowest 2^+ state. Potential energies $V(\beta, \gamma)$, were calculated in the frame of covariant energy density functional theory based on the relativistic mean field with the $NL3$ parameter set. The calculated excitation energies of the low-lying states are compared with experimental results presented in Fig. 5.23 and Fig. 5.24. There is a 2σ agreement between the calculations and experimental results in ^{72}Ge apart from the first excited 0_2^+ state. For ^{72}Se, the calculations and experimental energies agree within $\sim 1\sigma$.

As observed in [Aya16], the lowest excited 0^+ state in ^{72}Ge can be described by assuming the coexistence of two triaxially-deformed configurations. In other words, the potential energy V(β, γ) should have two coexisting minima.

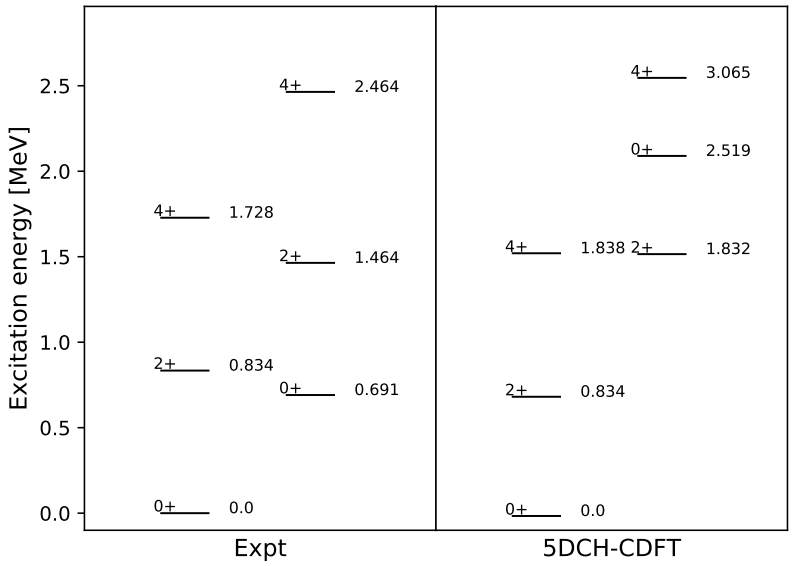

Figure 5.23: Calculated energies from the 5DCH-CDFT of the 0^+, 2^+, 4^+ states in ^{72}Ge compared with experimental results [Abr10].

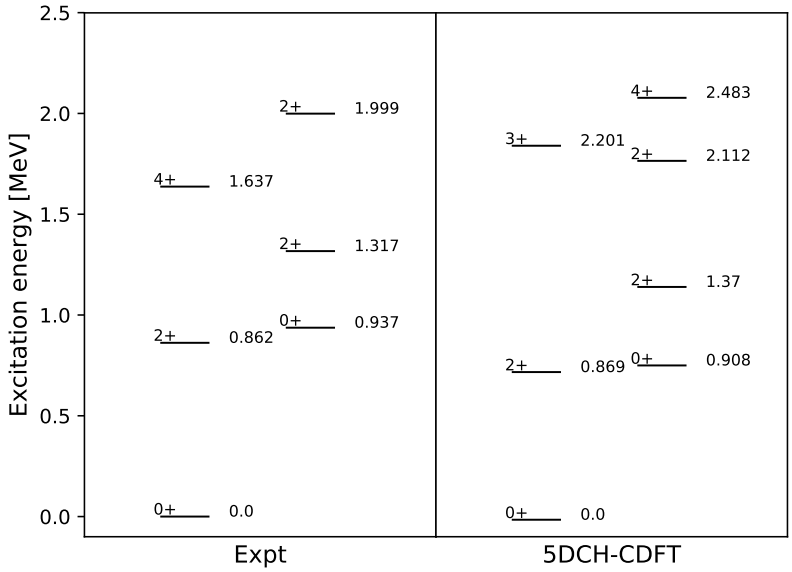

Figure 5.24: Calculated energies from the 5DCH-CDFT of the 0^+, 2^+, 4^+ states in ^{72}Se compared with experimental results [Abr10].

However, this calculation shows only one, albeit wide minimum. As a result, the model fails to describe the low-lying excited 0^+ state as evident in the large excitation energy. The calculated transition probabilities for ^{72}Ge are compared with experimental values in Table. 5.9. There is a standard deviation of an order of magnitude between the theoretical $B(E2)$ values and experimental values. A theoretical $\rho^2 \times 10^3$ value of 73.0 was obtained from the calculations using Eq. (2.25). The value is eight times larger than the experimental value from [McC11]. The discrepancy is due to the failure of the model to describe the low-lying excited 0^+ state. Furthermore, the results of the electromagnetic transition probabilities calculations for ^{72}Se are given in Table. 5.10. As evident from the table, the $B(E2)$ of the first excited 0_2^+ states obtained in the calculations is six times smaller than the experimental value. For other transitions, there is a maximum standard deviation of six between theory and experiment. Similarly, the obtained $\rho^2 \times 10^3$ value of 96.5 from the calculations is three times larger than the experimental value from [McC11]. This result can be improved by modifying the potential energy with the addition of a second triaxially-deformed minimum.

Table 5.9: Electromagnetic transition probabilities from 5DCH-CDFT calculations for ^{72}Ge compared with experimental values taken from [Abr10]. The standard deviation (SD) of the theoretical $B(E2)$ with calculated values are presented.

.

Energy (keV)	Transition Exp.	$B(M1)$ Cal.	$B(M1)$ (W.u) Exp.	$B(E2)$(W.u) Cal.	$B(E2)$(W.u) Exp.	SD
143	$2_1^+ \rightarrow 0_2^+$	-	-	5.94	17.8(3)	6
834	$2_1^+ \rightarrow 0_1^+$	-	-	31.34	23.5(4)	4
630	$2_2^+ \rightarrow 2_1^+$	$\sim$0	1.4E-4(5)	53.05	62^{+9}_{-11}	5
773	$2_2^+ \rightarrow 0_2^+$	-	-	$\sim$0	0.03^{+5}_{-6}	0.02
1464	$2_2^+ \rightarrow 0_1^+$	-	-	$\sim$0	0.13^{+18}_{-24}	0.07
894	$4_1^+ \rightarrow 2_1^+$	-	-	53.10	35(5)	9
1000	$4_2^+ \rightarrow 2_2^+$	-	-	34.12	15^{+8}_{-15}	10
1630	$4_2^+ \rightarrow 2_1^+$	-	-	$\sim$0	0.05^{+3}_{-5}	0.3

Table 5.10: Electromagnetic transition probabilities from 5DCH-CDFT calculations for ^{72}Se compared with experimental values taken from [Abr10]. The standard deviation (SD) of the theoretical $B(E2)$ with calculated values are presented.

Energy (keV)	Transition Exp.	$B(M1)$ Cal.	$B(M1)$ (W.u) Exp.	$B(E2)$(W.u) Cal.	$B(E2)$(W.u) Exp.	SD
75	$0_2^+ \rightarrow 2_1^+$	-	-	26.65	162(28)	68
862	$2_1^+ \rightarrow 0_1^+$	-	-	39.13	23.7(17)	8
455	$2_2^+ \rightarrow 2_1^+$	0.001	-	41.73	75(5)	16
380	$2_2^+ \rightarrow 0_2^+$	-	-	66.83	77(6)	9
1317	$2_2^+ \rightarrow 0_1^+$	-	-	0.27	0.44	0.02
1270	$3_1^+ \rightarrow 2_2^+$	-	-	11.85	-	-
1724	$3_1^+ \rightarrow 2_1^+$	-	-	0.02	-	
775	$4_1^+ \rightarrow 2_1^+$	-	-	55.71	55(5)	0.4
559	$4_2^+ \rightarrow 2_2^+$	-	-	46.39	-	-
1014	$4_2^+ \rightarrow 2_1^+$	-	-	67.97	-	-

5.4.2 NuShellX calculations for ^{54}Mn

Shell model (SM) calculations were performed for ^{54}Mn using the NushellX code [Bro14]. A doubly magic ^{40}Ca core was used in the fp-model space ($0f_{7/2}$, $0f_{5/2}$, $1p_{3/2}$ and $1p_{1/2}$ orbits) with effective Hamiltonian GXF1A [Hon04, Hon05]. The single-particle energies were fitted using data from the pf-shell nuclei to obtain the level excitation energies. The calculations were restricted to only the 1^+, 2^+ and 3^+ states which are the states that were excited in the experiment. This was also, helpful to save time and computing power.

The assignments of energies to excited states was based on the shell model assumption that each state has a well-defined spin and parity. However,

there are few states for which the spins are not experimentally established e.g., the state at 1544.0 keV is given 2^+, 3^+ in ENDSF. Thus, the assignments were done starting from the ground state to all states with possible spins and parities 1^+, 2^+ and 3^+ in order of ascending energy. For example, the state at 1544 keV was given spin-parity 3^+, since the first three 2^+ and 3^+ states were assigned for lower energy states and the fourth 3^+ state is lower in energy than the fourth 2^+ state, therefore, it was thought of it as being the next in line. The calculated excitation energies agree within 2σ with the experimental energies as shown in Fig. 5.25.

By combining the shell model calculations with experimental results, spin and parities were assigned to the excited states. The 1544 keV state which decays by the emission of 1544 keV gamma ray was assigned to be a $2,3^+$ state in previous experiments [Don14], however, the SM calculations suggest it is a 3^+ state. From the experimental results in this study, the 1544 keV transition was assigned a mixed $E2(+M1)$ multipolarity. This is consistent with the SM predictions; therefore, it makes sense to say the J^π of 1544 keV state is likely 3^+. Similarly, the 1634 keV and 2673 keV states have both been predicted to have J^π of 2^+.

Electromagnetic transition probabilities for the observed transitions in ^{54}Mn were calculated using the one-body transition densities. As explained by Suhonen [Suh07], effective charges are needed in the evaluation of the $B(E2)$s in order to correct the effects related to the limited model space. In this calculation, the effective charges used for protons and neutrons are $e_P = 1.5e$ and $e_n = 0.5e$. The results of the $B(E2)$ and $B(M1)$ are presented in Table. 5.11. The SM results differ from the experimental results with a maximum standard deviation of 42,

except for the 1400 keV and 1508 keV transitions. This deviation might be that there are contributions from outside the shell model space. Further investigation is needed to to reach a conclusion.

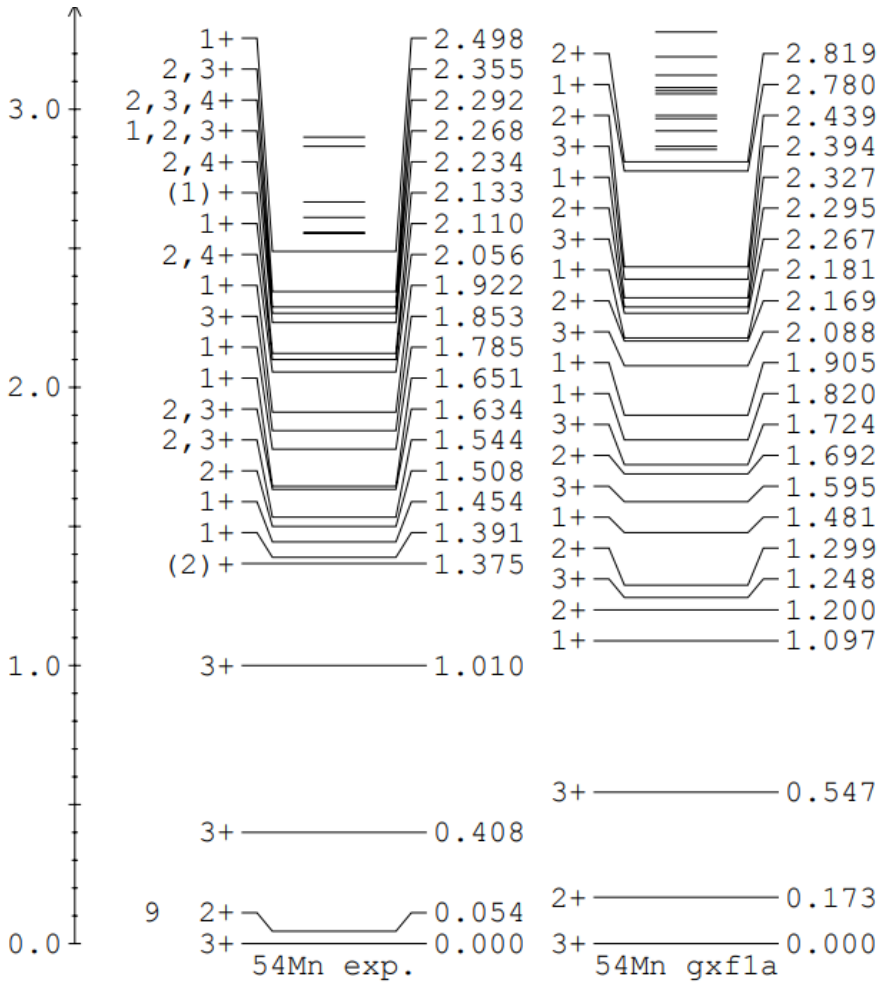

Figure 5.25: Excitation energies from Shell model calculations compared with experimental results [Don14] for the 1^+, 2^+ and 3^+ from ^{54}Mn. The energies are given in MeV.

Table 5.11: Transition probabilities from SM calculations for ^{54}Mn compared with experimental values taken from [Don14]. The standard deviation (SD) between the experimental values and theoretical values are also shown

E_γ (keV)	Transition Exp.	Transition SM+exp	$B(M1)$ (W.u) SM	$B(M1)$ (W.u) exp.	$B(E2)$(W.u) SM	$B(E2)$(W.u) Exp.	SD
1226	$2_4^+ \rightarrow 3_2^+$	$2_4^+ \rightarrow 3_2^+$	0.16	-	2.1	-	-
1320	$(2)_2^+ \rightarrow 2_1^+$	$2_2^+ \rightarrow 2_1^+$	3E-3	0.16(6)	0.3	30^{+5}_{-3}	15
1336	$1_1^+ \rightarrow 2_1^+$	$1_1^+ \rightarrow 2_1^+$	8E-4	1.4E-2(8)	0.2	12(8)	6
1400	$1_2^+ \rightarrow 2_1^+$	$1_2^+ \rightarrow 2_1^+$	4E-2	$(9E-5)^{+3}_{-6}$	1.4E-2	$(2E-4)^{+7}_{-2}$	0.007
1508	$2_2^+ \rightarrow 3_1^+$	$2_2^+ \rightarrow 3_1^+$	4E-2	3.6E-2(25)	0.19	$(2.1E-3)^{+162}_{-21}$	0.09
1544	$2,3^+ \rightarrow 3_1^+$	$3_4^+ \rightarrow 3_1^+$	1.4E-3	-	1E-3	-	-
1579	$2,3^+ \rightarrow 2_1^+$	$2_4^+ \rightarrow 3_1^+$	2.6E-2	-	1.19	-	-
1596	$1_3^+ \rightarrow 2_1^+$	$1_3^+ \rightarrow 2_1^+$	5.2E-2	-	3.4	-	-
1784	$1_4^+ \rightarrow 3_1^+$	$1_4^+ \rightarrow 3_1^+$	-	-	8.4E-2	84(21)	42
1798	$3_5^+ \rightarrow 2_1^+$	$3_5^+ \rightarrow 2_1^+$	2.7E-2	-	3.3E-3	-	-
1868	$1_5^+ \rightarrow 2_1^+$	$1_5^+ \rightarrow 2_1^+$	4.5E-2	-	0.41	-	-
2443	$1_9^+ \rightarrow 2_1^+$	$1_9^+ \rightarrow 2_1^+$	1E-3	-	0.33	-	-
2618	$?^+ \rightarrow 3_2^+$	$2_8^+ \rightarrow 2_1^+$	1E-3	-	2.5E-3	-	-
2848	$1_{10}^+ \rightarrow 2_1^+$	$1_{10}^+ \rightarrow 2_1^+$	2E-4	-	6.6E-2	-	-

Chapter 6

Conclusions and Recommendations

An electron spectrometer that uses a magnetic lens plus a Si(Li) detector with an array of gamma ray detectors was refurbished and characterized using standard electron sources. An in-beam experiment using a ^{70}Ge target was performed using an α-induced reaction. The experiment was performed for characterization purposes and for extraction of physics information on nuclei in the mass 70 region that has been under intense scrutiny for shape coexistence. The in-beam experiment yielded data from various reaction channels into ^{72}As, ^{72}Se and ^{72}Ge recoil nuclei, respectively. The deduced properties of the $E0$ transition in ^{72}Se support the interpretation of shape coexistence in this isotope. In the present work, the observed spectroscopic quantities in ^{72}As and ^{72}Ge were in good agreement with the values available in the literature as presented in Section 5.1.1.

In addition, properties of the lowest excited 1^+, 2^+ and 3^+ states of ^{54}Mn were investigated through ICE and IPF measurements. The extracted results produced a great deal of physics information, namely conversion coefficients, inten-

sity ratios between $E0$ and $E2$ transitions, mixing ratios and monopole strength $\rho^2(E0)$ parameter. It is worthy to note that the measurements provide the first experimental information on the mixing ratios of some transitions with mixed multipolarities as shown in Table. 5.8. The measured $\rho^2(E0)$ is comparable to similar measurements in neighbouring nuclei where shape coexistence has been reported. However, due to the large uncertainties in the $\rho^2(E0)$ value, it will be a good exercise to remeasure the spectroscopic information of the $2_2^+ \rightarrow 2_1^+$ transition required to obtain a precise $E0$ in order reach a definite conclusion.

As part of the long-term research plan of the iThemba LABS facilities, more developments on the electron spectrometer for internal pair formation measurements have been considered. This will involve segmented LEPS detectors at more advanced stage. In a related development, a proposal to couple the K600 magnetic spectrometer, for measuring the outgoing alpha particles, and thus isolating particles at zero-degree to pin-down these elusive 0^+ states have been approved by iThemba LABS Program Advisory Committee.

Bibliography

[Abr10] D. Abriola and A. A. Sonzogni. Nuclear Data Sheet (NDS), 111:1, 2010. of Health, Front Onclo, 5:270, 2015.

[Ago03] S. Agostinelli, J. Allison, K. Amako, J. Apostolakis, *et al.*, Nuclear Instrument and Methods in Physics Research A 506:250-303, 2003.

[Ald56] K. Alder, A. Bohr, T. Huus, B. Mottelson, *et al.*, *Study of Nuclear structure by Electromagnetic Excitation with Accelerated Ions.* Reviews of Modern Physics, 28:43, 1956.

[And07] J. Andrzejewski, A. Król, J. Perkowski, K. Sobczak, *et al.*, *Electron spectrometer for in-beam spectroscopy.* Nuclear Instruments and Methods A, 585:155-164, 2008.

[Ava20] A. A. Avaa, P. Jones, I. T. Usman, M. V. Chisapi, *et al.*, *Electron Spectrometer for Electric Monopole (E0) Transition Studies in Nuclei.* Nuclear Instrument and Method A 964, 2020 https://doi.org/10.1016/j.nima.2020.163809

[Aya16] A. D. Ayangeakaa, R. V. F. Janssens, C.Y. Wu. J. M. Allmond, *et al.*, *Shape coexistence and the role of axial asymmetry in* ^{72}Ge. Physics Letters B, 754:254-259, 2016.

[Bag02] C. M. Baglin. Nuclear Data Sheets, 96:611, 2002.

[Ban14] S. R. Banerjee. *Study of extreme nuclear shapes in extreme conditions.* AIP

Conference Proceedings, 1609:34-38, 2014.

[Bas15] M. R. Basu, S. Ray, A. Bison, and M. S. Sarkar. *et al.*, Journal of Instrumentation (JINST) preprint, 2015.

[Ber07] C. Bertulani. *Nuclear Physics in a Nutshell.* Princeton University Press, 248, 2007.

[Bla52] J. M. Blatt and V. F. Weisskopf. *Theoretical nuclear physics.* New York, Wiley 1952.

[Bob07] I. Boboshin, B. Ishkhanov, S. Komarov, V. Orlin, *et al.*, *Investigation of quadrupole deformation of nucleus and its surface dynamic vibrations* International Conference on Nuclear Data for Science and Technology, 65-68, 2007.

[Boh69] A. Bohr and B. R. Mottelson. *Single-Particle Motion. Vol. 1.* W. A. Benjamin, Inc., 189, 1969.

[Boh75] A. Bohr and B. R. Mottelson. *Nuclear deformations. Vol. II.* W. A. Benjamin, Inc., 681-683, 1975.

[Bra84] G. Braun, A. Bockisch and W.Neuwirthh. *Lifetime of the 0_2^+ state of ^{72}Ge determined by delayed Auto-coincidence of a Ge(Li) detector.* Nuclear Instruments and Methods in Physics Research, 224:112-116, 1984.

[Bro14] B. A. Brown and W. D. M. Rae. *The Shell-Model Code NuShellX@MSU.* Nuclear Data sheets, 120:115-118, 2014.

[Bro85] B. A. Brown, A. Etchegoyen, W. D. M. Rae, N. S. Godwin *et al.*, MSU-NSCL Report, 524, 1985.

[But96] P. A. Butler, P. M. Jones, K. J. Cann, J. F. C. Cocks, *et al.*, *Electron Spectroscopy using a Multi-detector Array.* Nuclear Instrument and Methods A, 381:433-442, 1996.

[Cap09] M. A. Caprio, D. J. Rowe, and T. A. Welsh. *Construction of SO (5) ⊃ SO (3) spherical harmonics and Clebsch-Gordan coefficients*. Computer Physics Communications, 180:1150-1163, 2009.

[Chi19] M. V. Chisapi. Private communication, 2019.

[Cho15] Q. Chong. *Theoretical Nuclear Physics*. https://https://www.kth.se/social/files/58d26e56f27654419542e9c8/Lecture2014, 2015.

[Cho94] W. T Chou and M. M King. Nuclear data sheets, 73:215, 1994.

[Chu56] E. L. Church and J. Weneser, *Electric monopole transitions in atomic nuclei*. Physics Review, 103:1035, 1956.

[Chu58] E. I. Church, M. E. Rose, and J. Weneser. *Electric-Monopole Directional-Correlation Experiments*. Physical Review, 109:1299-1306, 1958.

[Cre15] J. Cresswell and J. Sampson. *MTsort Language-ED0C033*. University of Liverpool, 2015.

[Dav10] D. J. Rowe and J. L. Wood. *Fundamentals of Nuclear Models*. World Scientific Publishing, first edition, 2010.

[Dio99] J. S. Dionisio, Ch. Vieu, E. Gueorguieva, K, Mohammed, *et al.*, *Accelerators, Spectrometers, Detectors and Associated Equipment*. Nuclear Instruments and Methods A, 437:282-334, 1999.

[Don14] Y. Dong and H. Junde. *Adopted Levels, Gammas*. NDS 121:1, 2014.

[Dra74] J. E. Draper, N. S. P. King, and W. G. Wyckoff. *In-beam Measurement of E0 Matrix Element in ^{72}Se and ^{72}Ge*. Physical Review C, 9:948-952, 1974.

[Dow20] J. T. H. Dowie, T. Kibédi, A. E. Stuchbery, A. Akber, *et al Evidence for Shape Coexistence in ^{52}Cr Through Conversion-electron and Pair-conversion Spectroscopy*. EPJ Web of Conferences, 232:04004, 2020.

[Epi18] Experimental Physics and Industrial Control System, (2018). http://

epics.anl.gov/base/R3-16/1-docs

[Eji89] H. Ejiri and M. J. A. de Voigt. *Gamma-ray and Electron spectroscopy in Nuclear Physics*, 38-41, 1989.

[Evi19] L. J. Evitts. A. B. Garnsworthy, T. Kibédi, J. Smallcombe *et al. Electric monopole transition strengths in the stable nickel isotopes*. Physical Review C, 99:024306, 2019.

[Fod17] A. Fodor. *Design and Simulation of Beam-Background Monitors in the Vicinity of the Electromagnetic Calorimeter for the Belle II Experiment*. PhD thesis, Department of Physics, McGill University, 25-26, 2017.

[Fra74] H. Frauenfelder and E. M. Henley. *Subatomic Physics*. Prentice-Hall, Inc., Englewood Cliffs, N.J, 1974.

[Gam90] Y. K. Gambhir, P. Ring, and A. Thimet. *Relativistic mean field theory for finite nuclei*. Annals Physics, 198:132, 1990.

[Gar97] G. Garcia Bermúdez, J. Döring, G. D. Johns, R. A. Kaye, *et al.*, *Collective structure in* ^{70}As. Physical Review C, 56:2869-2872, 1997.

[Gar16] P. E. Garrett, B. Jigmeddorj, A. J. Radich, A. J. Andreoiu *et al.*, *Conversion electrons from high-statistics β-decay measurements with the 8π spectrometer at TRIUMF-ISAC*. EPJ Web of Conferences, 123:02005, 2016.

[Gil08] G. R. Gilmore. *Practical Gamma-ray spectroscopy*. Second Edition. John Wiley and Sons, Ltd. 27-29, 2008.

[Gol55] M. Goldhaber and J. Weneser. *Electromagnetic transitions in nuclei*. Annual Review of Nuclear Sciences, 5:1-24, 1955.

[Ham65] J. H. Hamilton. *Internal Conversion Processes*. Academic press New York and London, 48, 1965.

[Ham74] J. H. Hamilton, A. V. Ramayya, W. T. Pinkston, R. M. Ronningen, *et al.*,

Evidence of Coexistence of spherical and deformed shapes in ^{72}Se. Physical Review Letters, 32:239-243, 1974.

[Ham74] J. H. Hamilton, K. Kumar, L. Varnell, A. V. Ramayya, *et al.*, *$E0/E2$ transition strengths and interpretations of 0^+, 2^+ states in Hf 178*. Physical Review C, 10:2540, 1974.

[Hax49] O. Haxel, J. H. D. Jensen, and H. E. Suess. *On the "Magic Numbers" in Nuclear Structure*. Physical Review, 75:1766, 1949.

[Hey90] K. Heyde and R. A. Meyer. *Comments on "Monopole strength and shape coexistence in the $A \approx 100$ mass region"*. Physical Review C, 42:790-792, 1990.

[Hey83] K. Heyde, P. Van Isacker, M. Waroquier, J. L. Wood, and R. A. Meyer *et al.*, *Coexistence in Odd-mass Nuclei*. Physics Report, 102:291-393, 1983.

[Hjo95] M. Hjorth-Jensen, T. T. S. Kuo and E. Osnes. *Realistic effective interactions for nuclear systems*. Physics Reports, 261:125, 1995.

[Hon04] M. Honma, T. Otsuka, B. A. Brown, and T. Mizusaki. *New effective interaction for pf-shell nuclei and its implications for the stability of the $N = Z = 28$ closed core*. Physical Review C, 69, 034335:1-29, 2004.

[Hon05] M. Honma, T. Otsuka, B. A. Brown, and T. Mizusaki. *Shell-model description of neutron-rich pf-shell nuclei with new effective interaction GXPF1*. Physical Review C, 69:499-502, 2005.

[Ide01] E. Ideguchi, D. G. Sarantites, W. Reviol, A. V Afanasjev, *et al.*, *Superdeformation in the Doubly Magic Nucleus* ^{40}Ca. Physical Review Letters, 87:22, 2001.

[Jon12] P. Jones, R. Bark, S. P. Bvumbi, T. D. Buche, *et al.*, Scientific and Technical reports, section 2.1.12, iThemba LABS An-

nual report. https://tlabs.ac.za/wp-content/uploads/pdf/annaul_reports/Annual_Report_2013_small.pdf. 79-81, 2012.

[Jon96] P. Jones. Ph.D. Thesis, University of Liverpool, 1996.

[Kan95] J. Kantele *Handbook of Nuclear Spectrometry*. Academic Press Limited, 1995.

[Kan04] H. Kankaanpää, P. A. Butler, P.T. Greenlees, J. E. Bastin, *et al. In-beam electron spectrometer used in conjunction with a gas-filled recoil separator*. Nuclear Instruments and Methods in Physics Research A, 534:503510, 2004.

[Kib90] T. Kibédi, G. D. Dracoulis and A. P . Byrne. *Lens-mode operation of a Superconducting Electron Spectrometer in (HI, xn) reactions*. Nuclear Instruments and Methods in Physics Research A, 294:523-533, 1990.

[Kib94] T. Kibédi, G. D. Dracoulis, A. P Byrne, P. M. Davidson, *et al.*, *Low-spin non-yrast states and collective excitations in* ^{174}Os, ^{176}Os, ^{178}Os, ^{180}Os, ^{182}Os *and* ^{184}Os. Nuclear Physics A, 567:183-236, 1994.

[Kib05] T. Kibédi and R. H. Spear. *Electric monopole transitions between* 0^+ *states for nuclei throughout the Periodic table*. AIP Conference Proceedings, 769:1, 2005.

[Kib12] T. Kibédi, A. E. Stuchbery, N. M. Krings, T and Protic, *et al.*, *Development of a new Si(Li)-detector array for the pair spectroscopy of the Hoyle-state*. Nuclear Science Symposium and Medical Imaging Conference (NSS/MIC),273-276, 2012.

[Kib11] T. Kibedi. *BrIccMIxing v2.3 manual*. BrIccMixing - ENSDF evaluation tool to determine Mixing Ratio(MR) and Normalization Factor from conversion electrons data, 1-5, 2011.

[Kib08] T. Kibédi, T. W. Burrows, M. B. Trzhaskovskaya, P. M. Davidson, *et al.*,

Evaluation of theoretical conversion coefficients using BrIcc. Nuclear Instrument and Methods A, 589:202-229, 2008.

[Kib20] T. Kibédi, T. K. Eriksen, J. T. H. Dowie, T. Tunningley, *et al.*, Nuclear Instrument and Method Physics Research A, Manuscript in preparation, 2020.

[Kid97] M. Kidera, M. Oshima, M. Katagiri, Y. Hatsukawa, and T. Morikawa. *Development of a Compact Multi-electron Detector for in-beam Spectroscopy.* Nuclear Instruments and Methods in Phys. Research A, 397:304-309, 1977.

[Kle64] P. Kleinheinz, I. Samuelsson, R. Vukanovic and K. Siegbahn. *A four-detector Electron directional correlation Spectrometer.* Nuclear Instruments and Methods, 32:1-27, 1964.

[Kno00] G. F. Knoll. *Radiation detection and measurement.* Third Edition. John Wiley and Sons, Inc. 309-312, 2000.

[Kon17] A. Koning, S. Hilaire and S. Goriely *TALYS-1.9*, 1.9, 2017.

[Kra88] K. Krane. *Introductory Nuclear Physics.* John Wiley and Sons, second edition, 1988.

[Lal09] G. A. Lalazissis, S. Karatzikos, R. Fossion, D. Pena Arteaga *et al.*, *The effective force NL3 revisited.* Physics Letters B, 671:3641, 2009.

[Lal97] G. A. Lalazissis, J. Konig, and P. Ring. *New parameterization for the Lagrangian density of relativistic mean field theory.* Physical Review C, 55:540-543, 1997.

[Lea15] K. G. Leach. *PHGN 422: Nuclear Physics Shell Model Supplement.* Department of Physics, Colorado School of Mines, 2015.

[Lei98] U. Leinberger, E. Berdermann, F. Heine, S. Heinz, *et al.*, *First energy and angle differential measurements of e^+e^--pairs emitted by internal pair con-*

version of excited heavy nuclei. European Physical Journal A, 1:249-256, 1998.

[Luo79] M. Luontama, J. Kantele, R. Julin, and A. Passoja. *A combination Intermediate-Image Magnetic Plus Si(Li) Electron Spectrometer for In-beam Experiments*. Nuclear Instruments and Methods, 159:339-345, 1979.

[Mar20] E. V. Mardyban, E. A. Kolganova, T. M. Shneidman, R. V. Jolos, *et al.*, *Description of the low-lying collective states of* ^{96}Zr *based on the quadrupole-collective Bohr Hamiltonian*. arXiv preprint arXiv:2004-13790, 2020.

[Mar76] M. A. J Mariscotti, M. Behar, A. Filevich, G. G. Bermudez, *et al.*, *Level structure of* ^{72}As *studied with the* (α, xnp) *reaction*. Nuclear Physics A, 260:109-123, 1976.

[Mar93] M. J. Martin. Nuclear Data Sheet (NDS), 70:315, 1993.

[Mat10] D. H. Mattox. *Handbook of Physical Vapour Deposition (PVD) Processing*. Second edition. Elsevier Inc. 1-24, 2010.

[May49] M. G. Mayer. *On closed shells in nuclei. II*. Physical Review, 75:1969-1970, 1949.

[McC11] E. A. McCutchen, C. J. Lister, T. Ahn, R. J. Casperson, *et al.*, *Shape coexistence in* ^{72}Se *investigated following the* β *decay of* ^{72}Br. Physical Review C, 83:024310, 2011.

[McG70] J. B. McGrory, B. H. Wildenthal and E. C. Halbert. *Shell-Model structure of* $^{42-50}Ca$. Physical Review C, 2:186, 1970.

[MID19] Multi Instance Data Acquisition System. 2019 http://npg.dl.ac.uk/MIDAS/

[Mon14] J. A. B. Monago. *Shape study of the* $N = Z$ *waiting-point nucleus* ^{72}Kr *via beta decay*. PhD thesis, Universidad Complutense de Madrid, 2014.

[Mou18] M. Moukaddam, J. Smallcombe, L. J. Evitts, A. B. Garnsworthy, *et al. In-beam internal conversion electron spectroscopy with the SPICE detector.* Nuclear Instruments and Methods in Physics Research A, 905:180-187, 2018.

[Mse19] L. Msebi , V. W. Ingeberg, P. Jones, J. F. Sharpey-Schafer, M. Wiedeking, *et al. A fast timing array 2″ × 2″ $LaBr_3$:Ce for lifetime measurements of excited nuclear states.* Nuclear Instruments and Methods in Physics Research A. Manuscript in preparation.

[Nev11] R. Neveling, H. Fujita, F. D. Smit, D. Adachi, *et al.*, Nuclear Instrument and Methods in Physics Research A, 654:29-39, 2011.

[New98] R. T. Newman, J. J. Lawrie, B. R. S. Babu, M. S. Fetea, *et al.*, Balkan Physics Letters, Special Issue. 182-190, 1998.

[Nik08] T. Niksic, D. Vretenar, and P. Ring. *Relativistic nuclear energy density functionals: Adjusting parameters to binding energies.* Physical Review C, 78:034318, 2008.

[OCo94] D. O'Connor, G. Knoll, and R. Ziff. *Evaluation and measurement of the experimental gamma-ray peaks broadenings and recovery times in a gain stabilized system.* Nuclear Instruments and Methods A, 353:291-295, 1994.

[OPE19] Opera FEA simulating software, 2019. operafea.com/opera-3d-static-electromagnetics-module

[Pak15] J. Pakarinen, P. Papadakis, J. Sorri, R. D. Herzberg, *et al. The SAGE Spectrometer.* European Physics Journal A, 50:53, 2014.

[Pap15] P. Papadakis, J. Pakarinen, P. A. Butler, D. Cox, *et al. The SPEDE spectrometer: combined in-beam γ-ray and conversion electron spectroscopy with radioactive ion beams.* Proceedings of the Conference on Advances in Radioactive Isotope Science (ARIS2014):030023, 2015.

[Pat15] S. Pattnayak, C. Padhan, C. R. Praharaj and Z. Niak. *Role of Intruder Orbits in the structure of doubly shall closed* ^{56}Ni Proceedings of the DAE-BRNS Symposium on Nuclear Physsics, 60:216-217, 2015.

[Pas85] A. Passoja, R. Julin, J. Kantele and M. Luontama. *E0 Transitions in* ^{70}Ge *and shape coexistence Interpretation of Even-Mass Ge Isotopes*. Nuclear Physics A, 441:261-270, 1985.

[Pov11] A. Poves. *The Nuclear Shell Model:Past, Present and Future*. https://ejc2011.sciencesconf.org/conference/ejc2011/EJC2011version_finale_poves. Accessed: 2019-05-17, 2011.

[Pro09] L. Próchniak and S. G. Rohoziński *Quadrupole collective states within the Bohr collective Hamiltonian*. Journal of Physics G, 36:1-53, 2009.

[Rad95] D. C Radford. Background subtraction from in-beam HPGe coincidence data sets. Nuclear Instruments and Methods A, 361:297-306, 1995.

[Rab95] S. Rab. Nuclear Data Sheet (NDS), 75:491, 1995.

[Ram87] S. Raman, C. H. Malarkey, W. T. Milner, C. W. Nestor, P. H. Stelson. *Transition probability,* $B(E2)\uparrow$*, from the ground to the first-excited* 2^+ *state of even-even nuclides*. Atomic Data and Nuclear Data Tables, 20, 1987.

[Ram75] A. V. Rammayya, R. M. Ronningen, J. H. Hamilton, W. T. Pinkston, *et al.*, *Mean life and collective effects of the 937 keV,* 0^+ *Se: Evidence for nuclear coexistence*. Physical Review C, 12:1360-1363, 1975.

[Ras60] J. O. Rasmussen. *Theory of E0 transitions of Spheroidal Nuclei*. Nuclear Physics, 19:85, 1960.

[Reg03] P. Regan. *Post Graduate Nuclear Experimental Techniques (4NET) Course Notes*. Department of Physics, University of Surrey, October, 49-50, 2003.

[Rez17] K. Rezynkina, A. Lopez-Martens, and K Hauschild. *On the graphical extrac-*

tion of multipole mixing ratios of nuclear transitions. Nuclear Instruments and Methods A, 844:96-98, 2017.

[ROO16] ROOT Data Analysis Framework https://root.cern.ch/content/release-53436. 3234, 2016.

[Ros49] M. E. Rose. *Internal pair formation*. Physical Review 76, 5:679-681, 1949.

[Row10] D. J. Rowe, and J. L. Wood. *Fundamentals of nuclear models: foundational models*. World Scientific, 2010.

[Rys80] M. Rysavi and O. Dragoun. *A Computer Program for the Determination of Nuclear Parameters from Initial Conversion Experiments*. Comput.Phys.Commun. 19:93, 1980.

[Sai14] Saint-Gobain. *Measuring Radiation Brochure*. 5, 2014. http://www.crystals.saint-gobain.com/

[Sai98] M. Sainath and K. Venkataramaniah. *Measurement of internal conversion coefficients of the 109 keV M4 transition in* ^{125}*Te*. IL NUOVO CIMENTO 111 A, 223 - 226, 1998.

[Sar09] M. S. Sarkar, S. Ray, P. Bhattacharya, R. M. Basu and A. Bisoi. *et al.*, Proceedings of the International Symposium on Nuclear Physics. 456-457, 2009.

[Sch87] B. Schüurmann, D. Rychel, B. Van Krüuchten, J. Speer, *et al.*, *Inelastic alpha scattering from the stable even germenium Iosotopes*, 1987.

[Shi18] Z. Shi, Q. B. Chen, and S. Q. Zhang. *Low-lying states in even Gd isotopes studied with five-dimensional collective Hamiltonian based on covariant density functional theory*. European Physical Journal [arXiv:1803.09471], 1-12, 2018.

[Shi13] N. Shimuzu. *Nuclear shell-model code for massive parallel computation,*

KSHELL. arXiv:1310.5431 [nucl-th], 1-2, 2013.

[Soh97] D. Sohler. *Nuclear Structure Studies in Ge-As region*. PhD thesis, MTA Atomki, 17-18, 1997.

[Soh99] D. Sohler, Zs. Podolyák, Zs. Dombrádi, J. Gulyás, and A. Algora, *Further evidence on shape coexistence in* ^{72}As Physical Review C, 59:1328-1333, 1999.

[Som18] V. Somá. *From the liquid drop model to lattice QCD: A brief history of nuclear interactions*. European Physical Journal Plus 133, (434):1-22, 2018.

[Sor16] J. Sorri. *Electron Spectroscopy with the SAGE Spectrometer*. PhD thesis, University of Jyväskylä, Finland, Department of Physics, March 2016.

[Sue11] Y. Suetsugu, Y. Tanimoto, Y. Hori, K. Kanazawa *et al.*, *Effects of external magnetic fields on the photoelectrons emission from a copper beam chamber*. Proceedings of the 2001 Particle Accelerator Conference, Chicago. 2180-2182, 2011.

[Suh07] J. Suhonen. *From nucleons to nucleus: concepts of microscopic nuclear theory*. Springer Science & Business Media, 2007.

[Sul03] A. Sulaksono, T. Bürvenich, J. A. Maruhn, P. G. Reinhard *et al.*, *Mapping exchange in relativistic Hartree-Fock*. Annals of Physics, 306:36-57, 2003.

[Szu11] T. Szucs, D. Bemmerer, T. Cowan, D. Degering, *et al.*, *Shallow-underground accelerator sites for nuclear astrophysics: Is the background low enough?*,The European Physical Journal A, 48:8, 2011.

[Tar02] O. Tarasov, B, Dominique, M. Lewitowicz, and O. Sorlin *The code LISE: a new version for "Windows"*. Nuclear Physics A, 701:661-665, 2002.

[TDK] TDK-Lambda EMEA available at https://emea.tdk-lambda.com/public/index.asp www.emea.tdk-lambda.com

[Tho18] T. K. Eriksen, PhD thesis, Australian National University, 75, 2018.

[Tho08] R. W. Thomae, P. J. Celliers, J. L. Conradie, J. L. G. Delsink, *et al.*, *Status of new electron cyclorton resonance sources at iThemba LABS*. Proceedings of ECRIS08, IL USA, 68 - 71, 2008.

[Tol57] S. Tolansky. *Introduction to Atomic Physics*. Longmans, Green and Co. 157, 1957.

[Trz90] W. H. Trzaska. *Recommended data on selected gamma-ray and conversion-electron calibartion sources* Nuclear Instrument and Methods A, 297:223-229, 1990.

[Var88] D. A. Varshalovich, A. N. Moskalev and V. K. Khersonskii. *Quantum theory of angular momentum*. World Scientific, 1988.

[Ver80] M. Vergnes. *Proceeding of the Intl. Conf. on the Structure of Medium-Heavy Nuclei, Rhodes, 1979*. The Institute of Physics, Bristol, 25, 1980.

[War72] E. K. Warburton and D. E. Alburger. *E*0 *Decay of the 2561 keV* 0^+ *Level of* ^{54}*Fe*. Physical Review C, 6:1224, 1972.

[Wal74] J. D. Walecka. *A theory of highly condensed matter*. Annals of Physics, 83:491, 1974.

[Wan14] X. Wang, D. M. Malaspina, H. W. Hsu, R. E. Ergun *et al.*, *The effects of magnetic fields on photoelectron-mediated spacecraft potential fluctuations*. Journal of Geophysical Research: Space Physics. 10.1002:7219-7326, 2014.

[War03] T. A. War, A. Chandan, R. Devi, S. K. Khosa and A. Bharti. *Importance of hexadecapole interactions in even-even Ge and Se Isotopes*. Indian Journal of Pure and Applied Pyhsics, 14:914-921, 2003.

[Wol25] P. Wolfgang. *On the connexion between the completion of electron groups in an atom with the complex structure of spectra*. Zeitschrift für Physik, 31:765,

1925.

[Woo99] J. L. Wood, E. F. Zganjar, C.De Coster, and K. Heyde. *Electric monopole transitions from low energy excitations in nuclei*. Nuclear Physics A, 651:323-368, 1999.

[Woo92] J. L. Wood, K. Heyde, W. Nazarewics, M. Huyse, *et al.*, *Coexistence in even-mass nuclei*. Physics Reports, 215:101-201, 1992.

[Won04] S. M. Wong. *Introductory nuclear physics*. Wiley-VCH, second edition, 189, 2004.

[Yar58] J. Yarwood. *Electricity, Magnetism and M Atomic Physics*. University Tutorial Press Ltd., 99, 1958.

[Yan96] F. Yang. and J. H. Hamilton. *Modern Atomic and Nuclear Physics*. The McGraw-Hill Companies, Inc., 82-503 1996.

[Zie13] J. F. Ziegler, M. D. Ziegler, and J. P. Biersack. *The Stopping and Range of Ions in Matter software*, 8, 2013.

Appendix A

Pumping and venting procedure

The outlined procedure is recommended for operating the iThemba LABS magnetic lens spectrometer vacuum.

Ensure that following valves are closed; V-1, V-2 by the sides of turbomolecular pump 1 (T1), V-6 by the side of turbo 2 (T2) and V-7 located close to the target control system on top of the spectrometer. When connected to a beam line, the valve V-9 located between the spectrometer and the beam line should always be closed when beam is not on target. Also, ensure that V-3 on the target ladder control system and V-4 connected by the side of turbomolecular pump 2 (T2) are open. Switch on the oil free backup pumps F1 and F2 then open V-2 gradually, wait until the Pirani gauge reads 10^{-1} mbar on meter 1 (M1) and meter 2 (M2), then switch on T1 and T2, gradually open valve V-6. Then press the start button on the second pump controller, check the status light which must turn orange to see if its running.

Venting to atmosphere: To vent the whole spectrometer to atmosphere, first switch off turbo T1 and T2 wait for a minute then switch off the

backup pumps F1 and F2. Use argon gas to vent the system by connecting to V-1, gradually open the vent valve monitoring meter 1 (M1) and 2 until the pressure rises to atmosphere.

Changing of target: Extract out the target ladder fully while V-3 is still open. Close V-3 using pneumatic control. Close V-5, then pump down slowly with pump 3 connected to V-8 by slowly opening V-8. Open and change the target but ensure V-7 is still closed. Connect the target ladder back then pump the target volume with pump 3 again by slowly opening V-8 meanwhile, V-5 should remain closed. Close V-8 and slowly open V-7 wait until the power supply light turns orange, then close V-7 and open V-5 and V-3 last to drive down the target to its position.

Appendix B

Remote control system

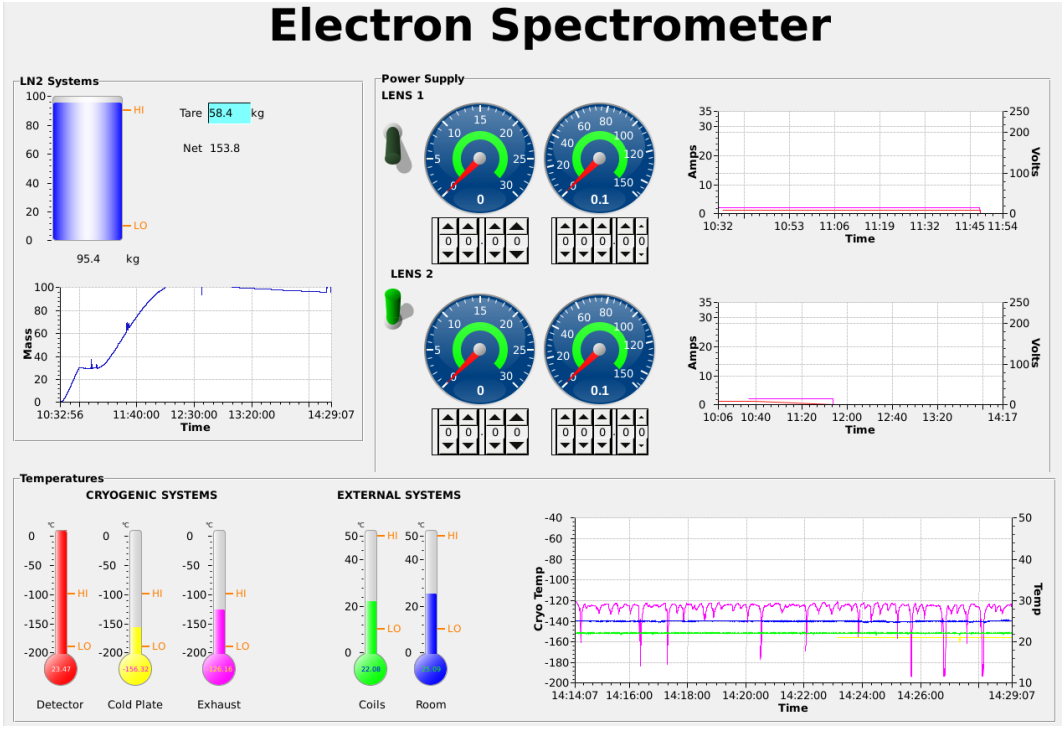

Figure B.1: The Experimental Physics and Industrial Control System (EPICS) showing the liquid nitrogen, power supply and cryogenics systems

Appendix C

Spectrometer earthing

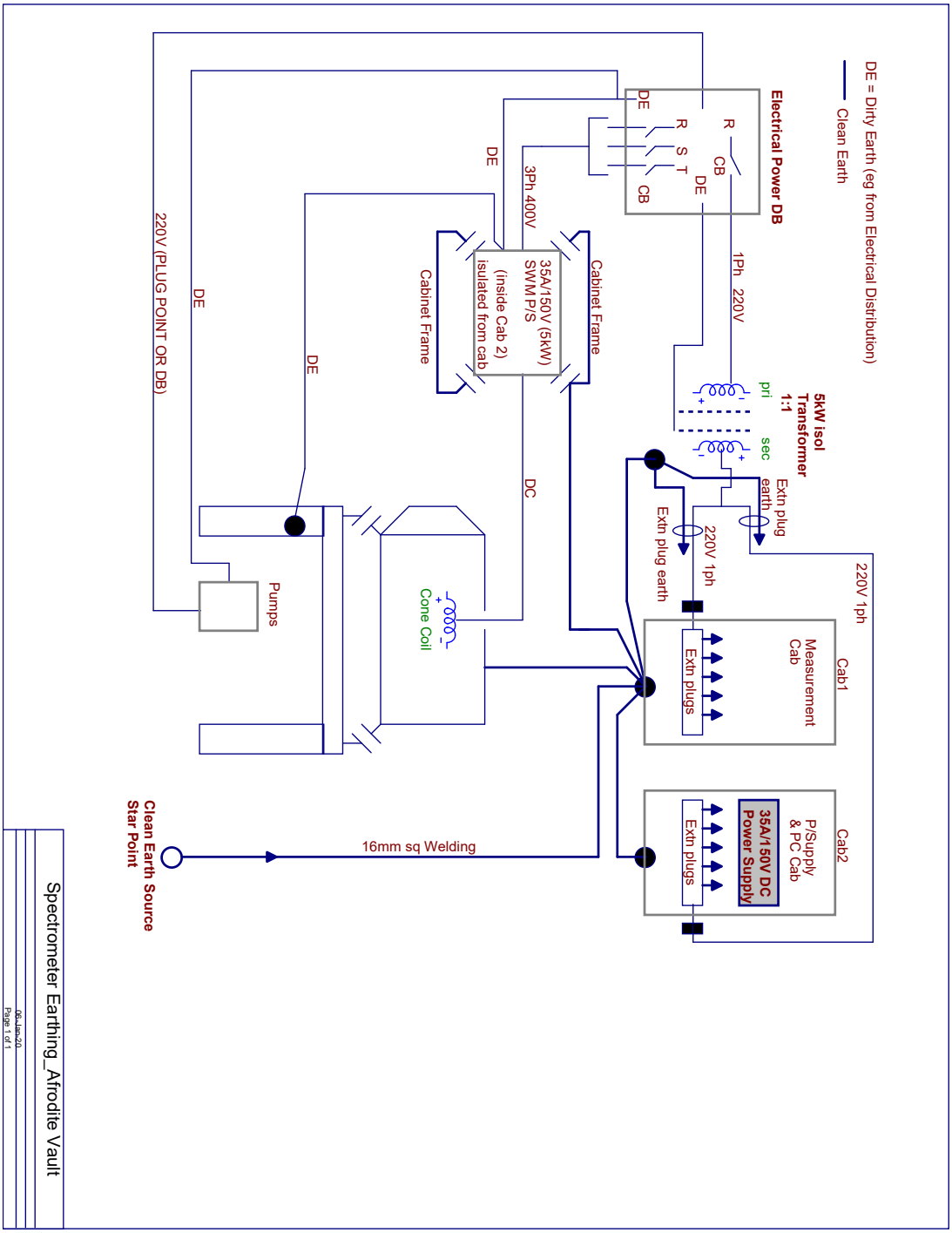

Figure C.1: Earthing of various components of the spectrometer to minimize noise.